Dynamic wave-modes in solar chromospheric structures

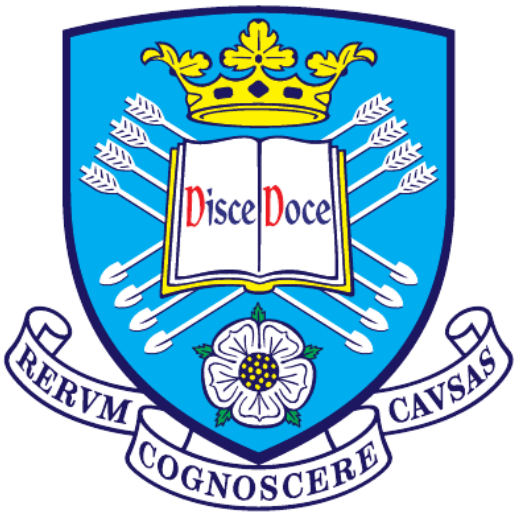

Rahul Sharma

Supervisor: Prof. Robertus Erdélyi

Co-supervisor: Dr. Gary Verth

School of Mathematics and Statistics (SoMaS)

The University of Sheffield

This dissertation is submitted for the degree of

Doctor of Philosophy

December 2017

सूर्य आत्मा जगतस्तस्थुषश्च

sūrya ātmā jagatas tasthuṣaš ca

The Sun, [is] the soul of whatever moves and stands

Rig Veda [I.115.1], 1700 BC

Declaration

The work in this thesis is based on the research carried out at the Solar Physics and Space Plasma Research Center (SP^2RC), within the School of Mathematics and Statistics, Department of Applied Mathematics, at the University of Sheffield, England. No part of this thesis has been submitted elsewhere for any other degree or qualification and it is all my own work, unless referenced to the contrary in the text.

Rahul Sharma
December 2017

Acknowledgements

It is a great pleasure and honor, to express my gratitude to many people, who directly or indirectly, helped me through my PhD years. First and foremost, I would like to thank my supervisors Prof. Robertus Erdélyi and Dr. Gary Verth for mentoring me in my academic pursuits in past 4 years. They are truly gifted scientists and it was my privilege to work with them. Robertus, thank you for believing in me, and giving me an opportunity to pursue my PhD at Sheffield. I have learnt a lot from you, and almost everyday of my PhD, acknowledged your patience in dealing with my rather slow and sometimes *not-so-mathematical* approach to the problems. Gary, you are amazing, and am really grateful to you for introducing me to the subject, being available to me and listening to my ideas, and encouraging me in the times, when I was lost and confused. I am truly grateful to the School of Mathematics and Statistics for funding my education and travels to many conferences, that I attended in course of my PhD.

At Sheffield, I met some of the most wonderful people in my life, my friends in erstwhile H23c and now H23. Stuart, Sam, Nabil and Drew for teaching me Python and dealing with my rather stupid queries on coding. Chris, you are simply awesome. A discussion with you always provided me a "sanity-check" to my research. Freddie, you are the best TeaMate one could ever ask for.. and also, other members of H23 (Mihai, Fin, Matt, Ellie, Rachael) for being unfortunate enough to share the same office with me. Alex and Stevie for reminding me of my incapabilties of dealing with dense Mathematics. My Hungarian friends (Tom, Norby, Mariana, Noemi) for teaching me some of the most useful words in the language. Thanks are due to Aditi and Rekha ji, for providing me the much needed 'Indian' environment, here in Sheffield. Thank you for the food, samosas, chai and all the flavors that kept my taste-buds alive in here.

I am heartily grateful to Prof. P. Venkatakrishnan for introducing me to astronomy, being my mentor and believing in my abilities to do science. Thank you for writing all those recommendations for my "summer-science-ventures", and to direct me on the path to become a scientist. It's my privilege to thank the staff and members of Udaipur Solar Observatory, for allowing me to visit at their place and use their facilities, for all those years. They exposed me to the wonders of science and especially, the solar

physics. Further, my family at Mumbai, Jodhpur and Udaipur, deserve a special thank for tolerating my adventures, which first appeared nothing like a proper career. To both my sisters (Manju and Karuna) jiji .. thank you for everything !!

And last, but not the least, this thesis is ***dedicated to the loving memory of my parents.*** After the death of my father, my mother which despite of all sorts of hardships and difficulties, brought me up, educated and made me who I am today. I have no words to express my gratitude for the love and affection, and the sacrifices she made, all those years. This thesis is devoted to her.

Abstract

Sun's outer atmosphere is a million degree hotter than it's visible surface, which is not understood with any of the known laws of thermodynamics and remains an intriguing problem for the astrophysics in general. It is now believed that most of the energy dissipation phenomenon occurs at the interface-region, which is a highly dynamic, gravitationally stratified, nonlinear, inhomogeneous environment, where the plasma-β varies from large, across unity, to very small. Previous studies, suggests that energy from lower solar atmosphere is transported up higher in corona by waves and oscillations through small-scale thin magnetic flux-tube structures, that populate the interface-region. This thesis primarily focuses on the identification and the understanding of the coupled linear/nonlinear wave-modes that are confined in the observed flux-tube structures. High-resolution imaging-spectroscopy data from the ground-based telescope is used to get an unprecedented view of the spicule structures within the complex chromospheric environment. Innovative analysis techniques were developed, for the first time, to investigate the three-dimensional (3D) ensemble of the observed kinematic components. The subsequent analysis at both, pixel- and the tube-scale, provided important insight into the nonlinear evolution of the coherent wave-modes, along with their consequent affects on the ambient solar atmosphere. Key findings include, the accurate interpretation of the observed spectroscopic (Doppler) velocity profiles, which were akin for both torsional Alfvén and kink wave modes. It was shown that the kinematic behavior of the kink wave-mode is not entirely transverse, but also has associated rotational component, due to displaced surrounding plasma. Also, the various observed kinematic components (transverse, cross-sectional width, azimuthal torsion) which, till-date, were observed *independent* to each other were found strongly coupled, with definitive phase-relationships. Furthermore, the non-helical evolution of the coupled dynamical components across the interface region, was found, due to the presence of a plethora of nonlinear wave phenomenon. The analysis, presented in this thesis, on the dynamics in the solar chromosphere, can provide the vital clues and insight into the mechanisms responsible for the transfer and dissipation of energy.

Table of contents

[1]This chapter is based on **Sharma, R.**, Verth, G and Erdélyi, R., 2017, "Dynamic Behavior of Spicules Inferred from Perpendicular Velocity Components", *The Astrophysical Journal*, **840**, 2.

[2]This chapter is based on **Sharma, R.**, Verth, G and Erdélyi, R., 2018, "Evolution of complex 3D - motions in spicules", *The Astrophysical Journal*, **853**, 1.

List of figures

List of tables

Chapter 1

Background

1.1 Introduction

One of the key unanswered questions remained in solar/steller astrophysics today is related to the million degree hot Sun's outer atmosphere, which is not yet understood with any of the known laws of thermodynamics. The origins of this problem dates back over 70 years, with the identification of the Fe IX and Ca XIV spectral lines (Edlén, 1943; Grotrian, 1939) in the outer solar atmosphere, indicating the presence of fully ionized plasma at million degrees. It is argued (Erdélyi, 2004, and references therein), that the actual interpretation of these spectroscopy results, in terms of the *solar coronal heating problem* was done in seminal work by Alfvén (1941). Since then, several physical mechanisms, that include, magnetic reconnection, current-cascades, turbulence, magnetic field braiding, magnetodydrodynamic (MHD) waves, etc., were proposed (see reviews and references within; Arregui, 2015; Erdélyi, 2004; Golub and Pasachoff, 1997; Kuperus, 1969; Kuperus et al., 1981) to answer this question, from both theoretical and observational perspectives, that involve energy dissipation through waves and/or magnetic reconnection.

One of the prime ingredients of all the energy transfer mechanisms is the magnetic field. On Sun, the magnetic field is not found to be homogeneous, but in discrete concentrations emerging out from the photosphere. Very large concentrations are observed as sunspots, which remained the focus of solar magnetism as well as dynamo theories. These form, what is known as, active regions and are the source of violent explosive events, like solar flares. Despite of much interest dedicated towards quantifying the role of these regions in the heating of the entire solar atmosphere, it was not, yet, fully understood whether these localized regions of intense solar activity can answer the long standing problem of the coronal heating. High-resolution ground- and

space-based observations of the quiet-Sun's photosphere also showed surface covered with weak concentrations of magnetic fields. These magnetic fields emanating from the intergranular lanes get concentrated by continuous buffeting of the photosphere and forms the foot-points of individual flux tubes. These thin magnetic flux tubes (MFTs) respond to the dynamical nature of solar surface and constantly emerge, move, interact and dissipate at a very short period of time. Previous studies suggested that mechanical energy/momentum (and mass) from the lower solar atmosphere is transported up higher in the corona by the MHD waves and oscillations through these thin MFT structures that populate the interface region (upper photosphere - chromosphere - transition region - lower corona) between the lower and higher solar atmosphere.

Recently, Aschwanden et al. (2007) advocated that the coronal heating problem is a paradoxical *misnomer* for the actual heating mechanisms that take place in the solar interface-region. This region bridge the cold solar photosphere (and kinetic pressure dominated) to the hot corona (and magnetic pressure dominated) and is home to many complex (plasma and magnetic) physical processes. As this layer is effectively bordered with the cold interplanetary environment, and subject to the radiative losses, it is imperative that a significant amount of energy is required ($\sim$15 times higher) to maintain its temperature at the order of 10^4 K (Fig. 1.1). Though, quest to answer the heating problem attracted attention of the solar physics community to the physics of corona itself, and had led serious efforts, both theoretical and observational, the solar interface-region remained poorly understood, partly due to the observational challenges and complex physical environment.

Recent, high-resolution ground- and space-based observations have revised the interest of the solar community to the physical mechanisms in the interface-region, through collective analytical, numerical and observational approaches. The underlying mechanisms of the energy transfer and dissipation processes in this layer are duly reflected in the dynamics of the fine-scale structures that are observed in multi-wavelength observations. This thesis deals with the observations and accurate identification of the associated MHD wave modes (linear/nonlinear), through innovative methods to gain insight into the full three-dimensional processes of the dynamics, and its possible role in *chromospheric* heating[1]. The interface-region, observed thin magnetic flux tube structures and historic dynamical records (non-MHD and MHD) are briefly reviewed in the following sections:

[1] *Here, this term is used only to imply the physical mechanisms required to maintain the equilibrium temperature at the chromospheric layer.*

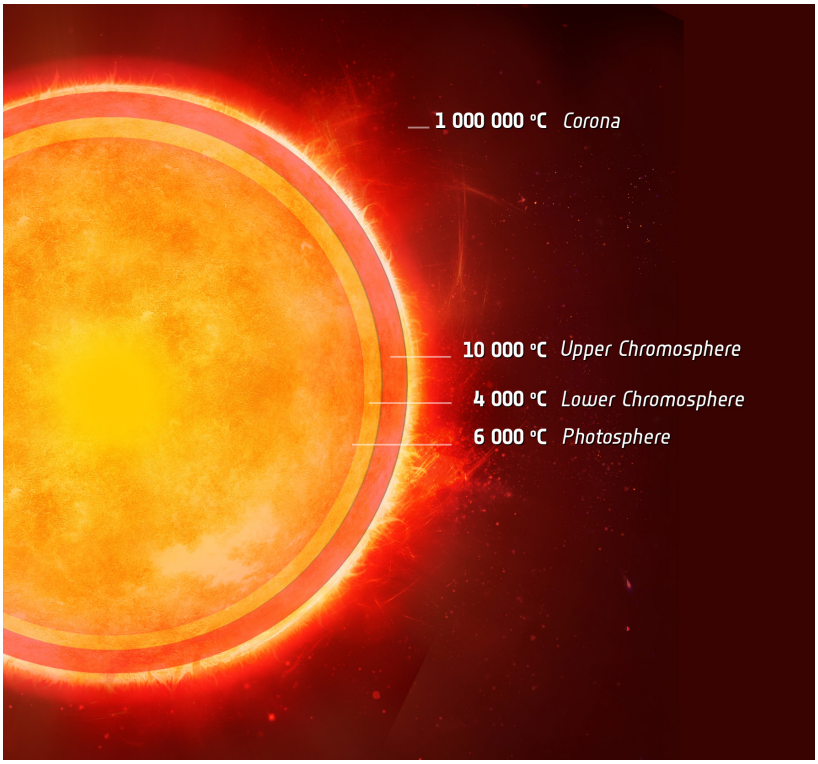

Fig. 1.1 Different consituent layers of the solar interface-region are shown. The temperature from the kinetic pressure dominated lower solar atmosphere (photosphere), of the order of a few thousand ($\times 10^4$) Kelvin, rises to several million ($\times 10^6$) Kelvin, in the magnetic-pressure dominated corona. This steep-rise in the temperature profile at the interface-region is termed as the *coronal heating problem*, and is at the focus of the research, to decipher the underlying physical mechanisms. Image credit: ESA (http://www.esa.int/spaceinimages/Images/2013/02/Cool_layer_in_a_Sun-like_star)

1.2 The heating at the Interface-Region

This region was first observed in the eclipse observations as a red/pink 'arc' around the Sun, and was named as '*chromosphere*' or the 'colored-sphere' by two Englishmen, Sir J. N. Lockyer (1836-1920) and E. Frankland (1825-1899). While, the earlier observations were only possible at the times of the solar eclipse, by the mid-1800s, astronomers were keen to explore this solar region by using spectroscopic techniques. French astronomer, Pierre Jules Janssen (1824-1907) was credited as the first to use a spectrograph, for solar chromospheric studies. At the same time, Sir Norman Lockyer made similar attempt to observe the chromosphere in bright Hα and H$_\beta$ spectral lines, for 20 October, 1868 eclipse in India, where, he made the discovery of Helium in the solar atmosphere. However, the lack of the understanding of the atomic spectra and the laws that govern the excitation of the atoms, earlier observations did not make much progress, in regard to the accurate interpretation of observed flash spectrum.

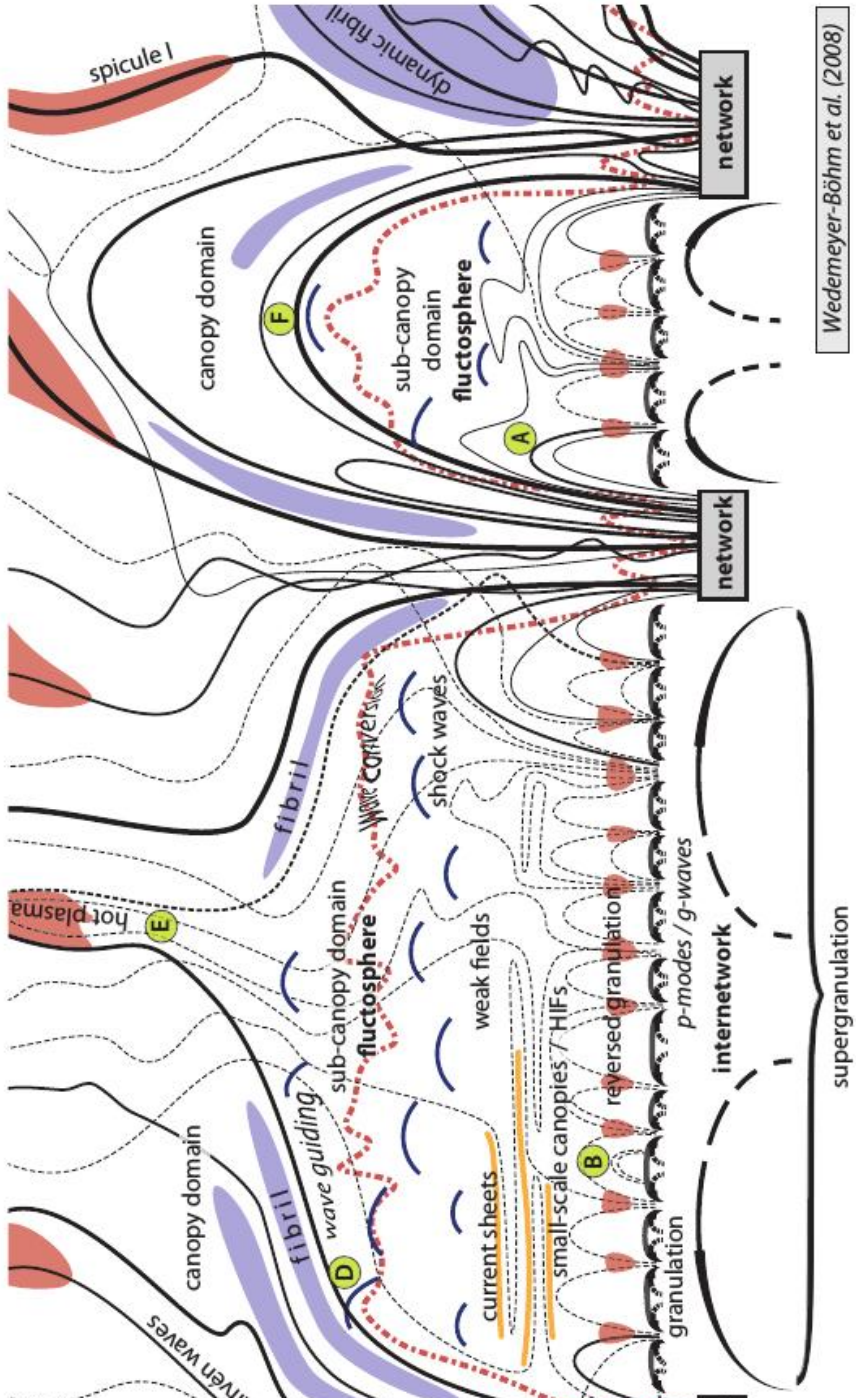

Fig. 1.2 A schematic picture of the solar interface-region. Solid lines mark the magnetic fields emerging out from the network region while dashed lines represent those emanating from the intergranular lanes. **A** an **B** show the small-scale loop features, while labels **D-F** show the conditions for wave and magnetic canopy interaction. However, it must be noted that actual 3D magnetic environment of the interface-region would be more complicated than shown here. Image credit: Wedemeyer-Böhm et al. (2009).

A major shift in the understanding of chromospheric observations came in 1920, when an Indian physicist, M. N. Saha (1893-1956) published, what later came to known as the Saha ionization equation (Saha, 1920). He proposed that, apart from the temperature, gas-pressure also plays an important role in the degree of ionization of a gas. Although, it did help to understand some of the observed features of the flash spectra (emission from ionized metals), however still, the presence of other emission lines, such as, hydrogen-Balmer, Ca II-H/K, He I-II, at the heights over 10 Mm, remained unanswered. In simple terms, the temperature at these heights was high enough for the electrons of hydrogen atoms to be excited from one energy level to the other. While, the theoretical models predicted a fall in the temperature to around 4000 K, at the height of 0.5 Mm above the photosphere, they failed to explain the rise in the temperature to around 8000 K at 2 Mm, and further, a steep rise to a million degree corona. This meant, that for the variations in the plasma parameters (temperature, pressure and density), for an extended inhomogeneous environment, there required other physical mechanisms to balance the thermal energy losses.

In principle, in the solar chromosphere, the energy losses take place largely due to radiation, thermal conduction and/or mass flows. However, the main cause of energy loss is the radiative losses (Withbroe and Noyes, 1977). Any energy loss from the other two factors (thermal conduction and flows) is restricted by the magnetic fields in the complex chromospheric environment (Fig. 1.2). Magnetic fields bind the plasma (mass and temperature) to only move along the magnetic fields, and not across them (assuming, e.g., resistivity is negligible). Also, presence of any closed magnetic configurations can further confine the chromospheric material to escape to much greater heights. Though, the lower solar atmosphere (photosphere, lower chromosphere) is kinetic pressure dominated, but it drops exponentially across the interface-region and thereafter dominated by the magnetic pressure. The ratio of the two (kinetic to magnetic) pressures is expressed as plasma-β and its variation across the interface-region is shown in Figure 1.3b. For these given physical conditions, various theoretical models for the solar chromosphere were developed, with both, homogeneous and inhomogeneous considerations, (Avrett and Loeser, 2008; Shklovskii and Kononovich, 1958; Vernazza et al., 1973, 1976, 1981). These models were built with many assumptions, about hydrostatic equilibrium, abundances, etc., to fairly match with the observations. Recent review on these models is given by Carlsson (e.g., 2007). Figure 1.3, shows the magnetic and the plasma environment of the solar interface-region, based on these given theoretical models and the associated observational constraints.

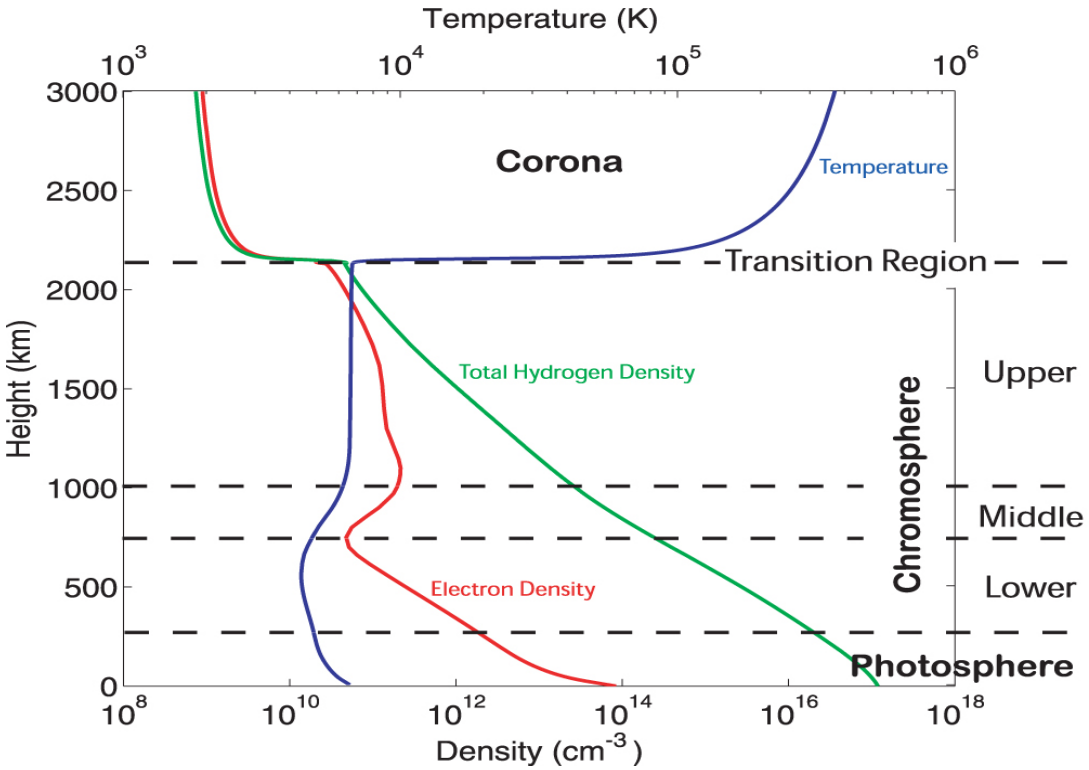

(a) Distribution of the temperature (blue) and the plasma density (hydrogen and electron) across different layers of the solar interface-region. The parameters used for the plot were adapted from the model chromospheric atmosphere given by Avrett and Loeser (2008). Image credit: Song (2017).

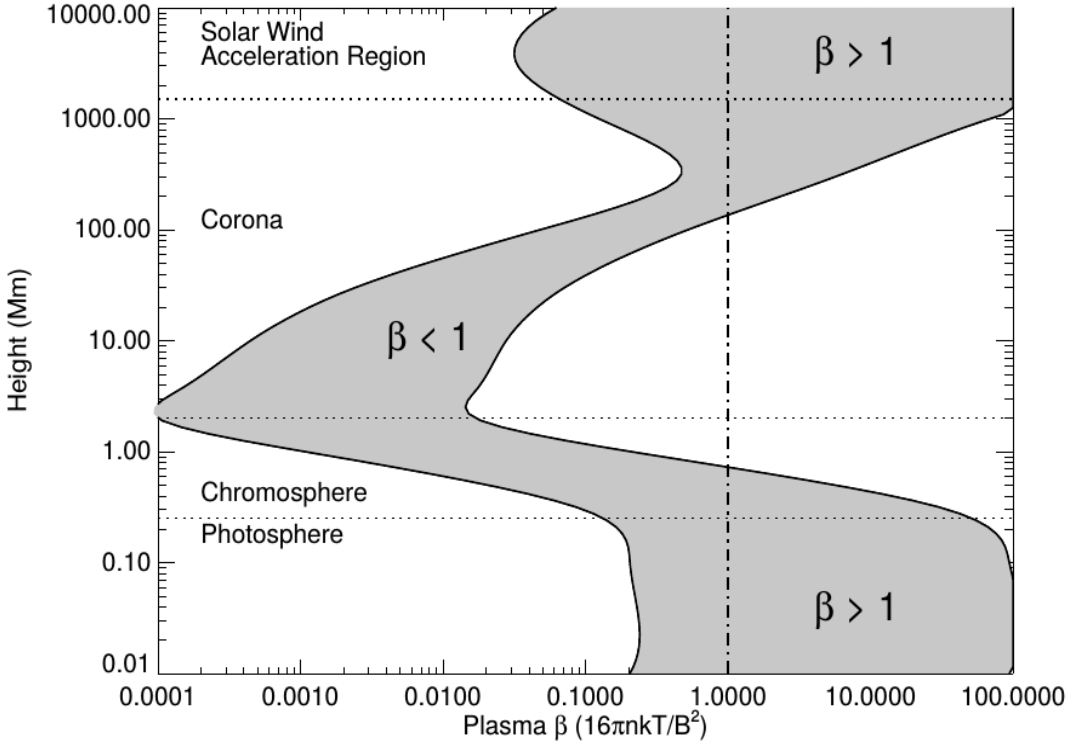

(b) Evolution of the plasma-β in the solar atmosphere. In the solar interface-region, the β parameter gradually varies from the plasma-pressure dominated photosphere to the magnetic-pressure dominated corona. Vertical dash-dot line marks the region where both the pressures (magnetic and plasma) are equal ($\beta = 1$). Image credit: Gary (2001).

Fig. 1.3 Plasma and magnetic environment in the solar interface-region

Till date, the theoretical, numerical and the observational studies identified, five major categories of physical mechanisms that could compensate the energy losses, and are given below:

1. **Heating by the turbulent motions of chromospheric plasma:** These were the first attempts to find a valid reason for the rise in temperatures in the lower solar atmosphere. In the early years, it was proposed that, in case, the features of the solar chromosphere could assumed to have a Maxwellian velocity distribution, then the turbulent motions in the chromospheric plasma could provide the necessary heating. However, these mechanisms were not been able to account for the further rise in the temperature to a million degrees across the solar transition region. A detailed overview for these attempts is given by Mariska (1986).

2. **Energy deposition by the acoustic waves:** The plasma number density in the solar chromosphere shows a rapid decrease with height, and here, the perturbations (acoustic) in the weak magnetic field regions (see, Narain and Ulmschneider, 1990, 1996), can evolve as nonlinear or shock waves, which can dissipate their energies at the transition region (Ulmschneider, 1981; Ulmschneider et al., 2005). The heating is mainly due to the vertical component of the velocities, though, a few studies question the amount of the total acoustic energy flux available for the observed thermal profiles (Fossum and Carlsson, 2005; Kalkofen, 2007).

3. **Role of the magnetic fields (MHD waves):** It is known that in, e.g., homogeneous and uniform plasma, three types of MHD waves are possible, viz, Alfvén and slow or fast magnetoacoustic waves. Osterbrock (1961), showed that all three categories of MHD waves can be damped in the lower solar atmosphere for low magnetic field regions (< 50G). The observations and associated dissipation mechanisms received vast interest from the solar community and is currently the focus of research for the heating in partially ionized (chromospheric) plasma (Khomenko and Collados, 2012; Soler et al., 2013). It was recently shown that, the MHD wave damping can showcase two effects, ohmic dissipation when the field is weak, and frictional heating, for stronger magnetic fields (Song and Vasyliūnas, 2011). For more comprehensive details on the MHD waves in the solar chromosphere see reviews by Jess et al. (2015); Verth and Jess (2016).

4. **By 5-minute oscillations:** Since their discovery in 1960's by Leighton and colleagues, these also were considered as prime candidates for the possible

energy source. The observations of waves with 5 minute periods in regions with strong magnetic fields were reported (Jess et al., 2009; Ulrich, 1996) to have sufficient energies to heat the lower solar atmosphere. However, the damping mechanisms associated with these waves were not clear, and in absence of any such mechanisms, the role of these waves remain questionable. Although, high-frequency Alfvén waves can heavily damp (Leake et al., 2005; Osterbrock, 1961), those with wave-periods of around 5-minutes, might not damp efficiently in the solar chromosphere.

5. **Magnetic reconnection:** It is a localized physical mechanism that involves the rearrangement of the magnetic field lines with release of huge amount of energy. In simplest scenarios, when two magnetic field lines, frozen in the plasma, come close to each other, then at some point in time due to weak non-ideal effects in Ohm's law, they rearrange and reconnect. Though, this idea was proposed as a key mechanism for the release of energy in solar flares (Parker, 1957), it gained concrete observational support after the launch of space-borne instrumentations onboard Yohkoh, and later from SoHO, TRACE, RHESSI and SDO. However, the role of magnetic reconnection in coronal heating was debated, due to it's localized nature and prominence in regions with high magnetic field concentrations (active regions). Later, it was proposed that on much smaller spatial-scales, the reconnection phenomenon occurs as nanoflares and can provide the necessary thermal energy input to sustain the coronal temperatures (Cargill and Klimchuk, 2004). In lower solar atmosphere, the signatures of magnetic reconnection process were routinely observed and reported as bursts (Emslie and Noyes, 1978), explosive events (Dere et al., 1989), blinkers (Harrison, 1997), Ellerman bombs (Rutten et al., 2013), IRIS bombs (Peter et al., 2014), etc.

Apart from the mechanisms mentioned above, more complicated processes, e.g., resonant absorption (see review by, Goossens et al., 2011), phase-mixing (Heyvaerts and Priest, 1983), compressional viscous heating, can also contribute to the heating of the inhomogeneous solar atmosphere. Song and Vasyliūnas (2011) in their study, concluded two major factors for the lack of any conclusive mechanism for the chromospheric/coronal heating. They stressed the confusions related with the radiative cooling along with the temperature rise at the interface region in the available chromospheric models. Furthermore, they highlighted the inaccurate interpretation of the observed perturbations associated with the fine-scale structures, which could be taken as the source of wave energy in the interface-region. The questions about the wave-mode

identification and interpretation forms the central theme of this thesis. The following sections, briefly review the observed fine-scale MFT structures, and the associated dynamical behavior, in terms of the MHD wave-modes.

1.3 Jet-like structures in the Interface-Region

High-resolution observations have shown that the solar interface-region is a highly dynamic, stratified and an inhomogeneous layer, which is populated by the features that evolve over the course of a few seconds to several minutes (Tsiropoula et al., 2012). According to Kalkofen (1990), the structures in the solar chromosphere (interface-region) can broadly be classified into three regimes, based on the strength of the observed emissions:

1. magnetic elements (closed and open) at the boundary of the supergranular cells,
2. bright points (grains) in the cells, and
3. the ambient quiet-chromosphere, also in the cell interior.

The closed magnetic systems that bridge regions of opposite polarities were observed and first reported as low-lying arches in the chromospheric observations and were named as "arch-filament systems" by Bruzek (1967). He showed that these features have an average length of around 30 Mm, and lifetimes of about 30 minutes. Similar features were also reported as "unresolved fine structure" (UFS) by Feldman (1987). Recently, these structures were observed in multiple wavelengths from IRIS spacecraft, with high Doppler velocities ($\sim$80 km/s) and lifetimes of around 200 sec by Hansteen et al. (2014). Nevertheless, one of the most common building blocks of the chromosphere are the thin magnetic flux tube structures (MFTs). These ubiquitous jet-like features when observed, as clusters/bushes, are again classified on the basis of location (on-disk/limb/active/quiet-Sun region), wavelength and physical properties (lifetimes, density, plasma flows, length, etc.). At the limb (disk), these structures are highlighted as intensity enhancements (depressions), suggestive of higher plasma density as compared to the ambient environment. The dynamics and the physical conditions of the lower solar atmosphere are well reflected in observed motions of MFTs and are crucial to the understanding of the mass, energy and momentum transfer across the interface-region. These reasons prompted many observational and mathematical approaches, to gain the necessary insight into the origins and the physical behavior of these structures. Since mid-1970s, papers by Parker (1974a,b) stimulated the efforts

by proposing the hydrodynamic mechanism linked with the turbulent pumping and conregated magnetic fields into the tube-like structures. These efforts were joined by other theoretical works during the same period, investigating the fundamental properties of these small-scale MFT structures (Cram and Wilson, 1975; Defouw, 1976; Roberts and Webb, 1978; Spruit, 1981).

The common mathematical approach[2] in those early attempts were based on the MHD approximations, which were derived from the Maxwell's equations:

$$\nabla \cdot \mathbf{B} = 0 \tag{1.1}$$

$$\frac{\partial \mathbf{B}}{\partial t} = \nabla \times (\mathbf{v} \times \mathbf{B}) + \eta_D \nabla^2 \mathbf{B} \tag{1.2}$$

$$\rho \frac{d\mathbf{v}}{dt} = -\nabla p + \frac{1}{4\pi}(\nabla \times \mathbf{B}) \times \mathbf{B} - \rho g(z) \tag{1.3}$$

$$\frac{d\rho}{dt} + \rho \nabla \cdot \mathbf{v} = 0 \tag{1.4}$$

$$\frac{\partial(\rho^{-\gamma} p)}{\partial t} + \mathbf{v}\nabla(\rho^{-\gamma} p) = 0 \tag{1.5}$$

Here, **B**, **v**, p, ρ, g, represent the magnetic field, velocity, pressure, density and gravity respectively. $d/dt = \partial/\partial t + \mathbf{v} \cdot \nabla$, magnetic diffusivity ($\eta_D = \frac{c^2}{4\pi\sigma}$) with $\sigma = \frac{1.96ne^2}{(m_e \nu_{ei}}$) is the plasma conductivity. The magnetic flux tube with a cylindrical geometry can be considered as a concentration of the magnetic flux/field-lines, for a given surface S, which is bounded by a closed counter C. The magnetic lines of force ($\mathbf{B}(\mathbf{r})$) is then, the solution of the equations,

$$\frac{dr}{B_r} = \frac{r d\phi}{b_\phi} = \frac{dz}{B_z} \tag{1.6}$$

By applying Gauss's theorem to the equation (1.1), the total magnetic flux across the closed surface S is taken as zero

$$\int_S \mathbf{B} \cdot \mathbf{dS} = 0. \tag{1.7}$$

This implied that each field line, that entered the closed surface, also left the surface, while the total magnitude of the magnetic flux in the closed contour C remained constant

[2] *The mathematical description, presented here, is adopted from Ryutova (2015)*

$$\Phi = \int_C \mathbf{B} \cdot \mathbf{dS}. \tag{1.8}$$

This also meant that the cross-section of the closed contour is inversely proportional to the magnetic field strength. For a narrower flux tube, the magnetic field strength is higher and vice-versa.

In order to maintain a hydrostatic equilibrium of a flux tube, let us assume that the enclosed magnetic field only depends upon the axial coordinate (r), $\mathbf{B} = B(0,0,B_z(r))$. Then, the momentum equation (1.3), for this case, becomes

$$-\nabla p + \frac{1}{4\pi}(\nabla \times \mathbf{B}) \times \mathbf{B} - \rho \mathbf{g} = 0, \tag{1.9}$$

where $\mathbf{g}$ is the gravity on solar surface. However, if this term is ignored, then,

$$\begin{aligned} p(r) + \frac{B_z^2(r)}{8\pi} &= p_e \\ p(r) + \frac{B_z^2(r)}{8\pi} &= p_e + \frac{B_{ze}^2(r)}{8\pi}. \end{aligned} \tag{1.10}$$

Here, p_e is the gas pressure outside the flux tube. Equations (1.10) represent the conditions for the static equilibrium of the flux tube, in an external environment, with and without magnetic field (external). However, in the presence of gravity, acting along the negative z-axis, equation (1.9) gives the relation

$$\frac{dp}{dz} + \rho g(z) = 0. \tag{1.11}$$

From the ideal gas law, the density of the plasma can be given as, $\rho = mp/kT$, where 'k' is the Boltzman constant. Therefore,

$$p = p_0 \ \exp\Big(\int_0^z \frac{1}{\Lambda(z)} dz\Big), \tag{1.12}$$

where,

$$\Lambda(z) = \frac{kT}{mg}, \tag{1.13}$$

is the scale height (pressure). The equation (1.12) can also be described in terms of density (ρ) parameter, as,

$$\rho = \rho_0 \frac{T_0}{T(z)} \exp\Big(-\int_0^z \frac{1}{\Lambda(z)} dz\Big). \tag{1.14}$$

Though, the smallest possible observation of the flux tube feature on the Sun depends on the angular-resolution of the telescope, still wide-range of the flux tube structures are routinely observed and analyzed for their physical properties and dynamical behavior. Brief overview of such commonly observed chromospheric MFT structures are as follows:

1. **Spicules:** Reported first as "flames" by Father Angelo Secchi in 1877 from observations at the Vatican Observatory (Secchi, 1877), and later as "wheat-field" or "porcupine" patterns by (Lippincott, 1957), spicules are thin, jet-like structures, observed at the solar limb. Since their first discovery, around 140 years ago, these features, are still, the key observational 'window' for the investigations related with the mass and energy transfer mechanisms across the interface-region. Several excellent reviews on the early works, describing their models for origins (Sterling, 2000), and also the observational properties (Beckers, 1968, 1972; Beckers et al., 1966; Tsiropoula et al., 2012) were given. These features were classified as types- I and II by De Pontieu et al. (2007c), when observed in the high-resolution Ca II-H data from *Hinode*/SOT. It was suggested that type-I spicules are long-lived structures with lifetimes of 3-7 minutes, velocities ($\sim$20 km/s) and bidirectional (upward and downward) mass flows, while the type-II spicules are short-lived (50-100 sec), with higher velocities ($\sim$100 km/s) and unidirectional (upward) flows. However, this classification was later questioned by Zhang et al. (2012), where they did not found any differences in the observed spicule cases, from a similar dataset. Recent, multi-spacecraft, multi-wavelength data analysis for off-limb spicule structures by Pereira et al. (2014), showed that spicules are multi-thermal species (Fig. 1.4) which traverse from one passband to the other, and hence their classification, as types I or II, based on the physical characteristics derived from single wavelength observations, might not be appropriate. Nevertheless, at any given time, around 2×10^7 spicules are found on the solar surface (Judge and Carlsson, 2010), depending strongly upon the quality, threshold intensity and height of the observations. Another important aspect of spicule observation is their inclination with respect to the vertical. The angle of inclination was found in the range $\sim20^\circ$ (Beckers, 1968) to $\sim37^\circ$ (Trujillo Bueno et al., 2005), with an average of 23°.

2. **Mottles:** These constitute one of the most fundamental chromospheric structures, observed on the solar-disk in the quiet-Sun regions (left panel: Fig. 1.5a). In past studies (Bhavilai, 1965; Tsiropoula et al., 1993), these structures were debated as on-disk spicules, and also similar to the fibrils (Foukal, 1971b), in terms

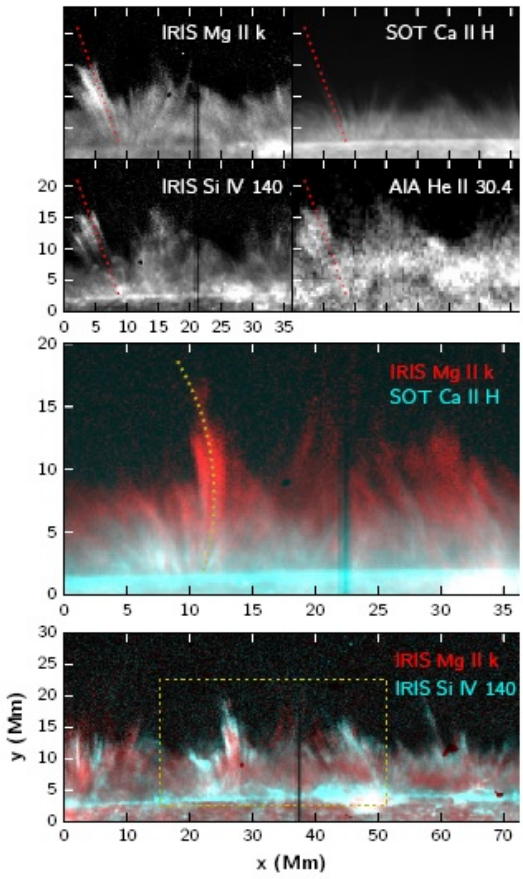

Fig. 1.4 Simultaneous observations of the off-limb spicule structures, by several space-based platforms (*Hinode*/SOT, IRIS, AIA spacecraft), in different wavelengths (marked on the images), indicating a multi/mixed-thermal nature of these structures. The spicules appear longer with more extended lifetimes as percieved before in single-wavelength observations. Image credit: Pereira et al. (2014).

of the origin and physical properties. On-disk, these structures appear in clusters, as dark (absorbing) features in the Hα and Ca II wavelengths. These mottle clusters occur either as *chain*-like patterns, originating from the intergranular lanes between two supergranular cells, or as *rossttes*, which are comparatively larger groups, observed at the junction of three or more supergranular cell boundaries. Sawyer (1972), further classified these structures on the basis of their observed shapes (oval, round, filamentary, arch and lumpy) for horizontal lengths of the order 2-7.5 Mm (Bray and Loughhead, 1974). Though, due to observational challenges, it is hard to determine the exact lifetimes of these structures, but analysis do show mean-lifetime of mottles of the order of 13-14 minutes (Bratsolis et al., 1993).

3. **Rapid Red/Blue shifted Excursions (RREs/RBEs):** These are the sudden, perceptible shift in the Doppler estimates at either wing-positions of the line profile, observed in Ca II and Hα passbands. These were first reported from on-disk observations by Langangen et al. (2008), as the counterparts of the off-limb spicules (type-II) in Ca II line. They reported Doppler shifts in the blue-wing of the line profile, without associated changes in the red-wing, around rosette regions. These rapid blue-shifted excursions or RBEs had an average length of around 1.2 Mm, with measured width of 0.5 Mm. The lifetimes and velocities for these structures were of the order of 45$\pm$12 sec and 15-20 km/s. These were also studied in Hα wavelengths, along with Ca II, by Rouppe van der Voort et al. (2009), using the high-resolution data from CRISP/SST (right panel: Fig. 1.5a). They found that these features appear longer ($\sim$3 Mm) and with comparatively high Doppler velocities ($\sim$35 km/s) in Hα line. Field-aligned flows, transverse and torsional motions were reported, along with other statistical properties, in a series of papers by Sekse et al. (2012, 2013a,b). They reported Doppler velocities of the order of 15-40 km/s in the quiet-Sun regions and around 30-50 km/s in the coronal-holes. The transverse motions were also found to be of the order of $\sim$55 km/s with an average-lifetime of 30 sec, for these features. Kuridze et al. (2015) analyzed the dynamical behavior of these features, observed in Hα spectral line, and attributed the role of transverse velocities (50 - 150 km/s) in the formation and appearance of these jet-like structures.

4. **Fibrils & Dynamic Fibrils (DFs):** These are thin tube-like, elongated, highly dynamic structures, usually observed near regions with high magnetic field concentrations (active regions/plages). Those fibril features observed to close proximity of the sunspots (penumbral-fibrils) show filamentary structures and are closely linked with the low-lying loops, without jet-like behavior. These features are also known as dynamic fibrils (DFs). On contrary, those found near active-region plages, show jet-like behavior and have shorter lifetimes as compared to those observed near sunsport penumbra. Observed in both Hα and Ca II wavelengths, these structures show close resemblance to the mottles in the quiet-Sun regions, in terms of appearance in clusters as *bushes* or *rosettes*. Foukal (1971a,b) in his analysis, proposed compelling relationship between the thin flux-tube structures observed near active-regions and those at the quiet-Sun environment. He provided comparison between the physical parameters, such as, lifetimes, length, density, velocities and the temperature, for the fibril and spicular structures and concluded that, due to the strong magnetic fields, fibrils

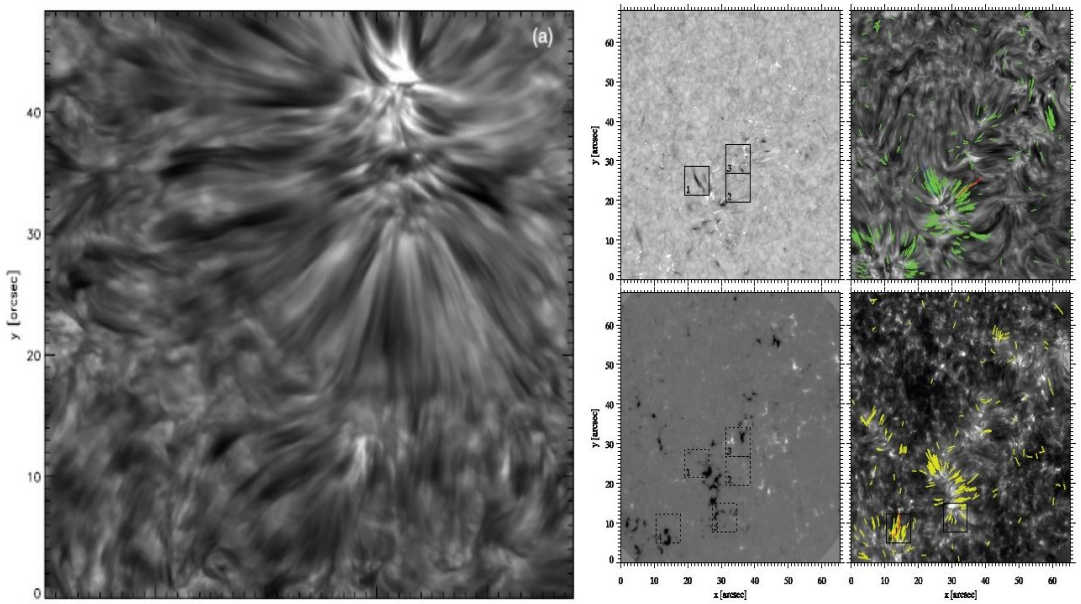

(a) Example of on-disk mottle structures (left), in the Hα line-core position, observed from the Swedish Solar Telescope (SST). The curved/elongated/dark mottle structures are believed to be emanating from the network region visible at the upper right corner of the image. Credit: De Pontieu et al. (2007b). The panels in the right show examples of Rapid Blue-shifted Excursions (RBEs) in Hα line (left: top) with corresponding Fe 630.2 nm blue wing magnetogram (left:bottom). Yellow and green lines (right:top-bottom) show detected paths of Ca II and Hα RBE structures. Image credit: Rouppe van der Voort et al. (2009)

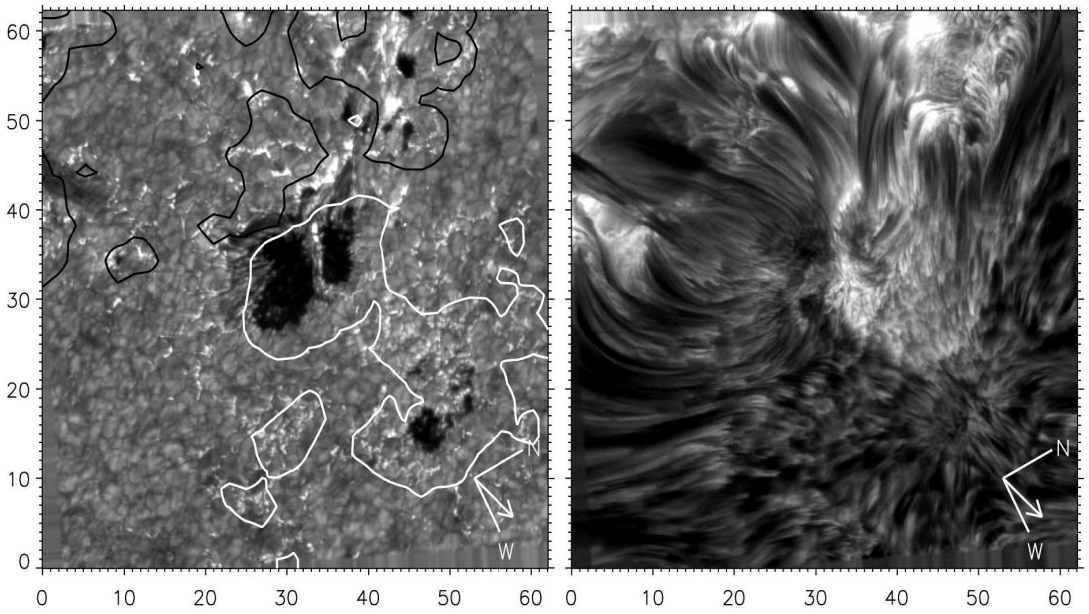

(b) Left and right panels shows an active-region in the Hα wing position and at line-core, observed from the Swedish Solar Telescope. The black and white contours represent the negative and positive magnetic flux, taken from MDI/SoHO magnetogram, along with the overlying dynamic fibril (DF) structures in the Hα observations. Image credit: De Pontieu et al. (2007a)

Fig. 1.5 Examples of chromospheric mottles and RBE structures (top), observed in the Hα observations and dynamical fibril features observed near an active-region (bottom).

are more inclined to the vertical and appeared horizontal in on-disk observations. Also, these structures were much more elongated than both spicule and mottle structures. Their physical parameters were also studied in detail by De Pontieu et al. (2007a) using high-resolution data from the Swedish Solar Telescope in Hα wavelength (Fig. 1.5b). They reported the average length of observed DFs to be 1.25 Mm, with magnitudes in the range 0.4-5.2 Mm. These structures were found not varying much in time (lifetime in range 120-650 sec) with average width of around 340 km, comparative to the estimated widths of 360$\pm$120 km by Morton et al. (2012a) and $\sim$265 km by Gafeira et al. (2017a) for Slender Ca II Fibrils (SCFs) (Gafeira et al., 2017b).

5. **Straws:** These are much thinner counterparts of the mottles and were first reported and labelled by Rutten (2006, 2007), using the high-resolution Ca II H filter at the Dutch Open Telescope (Fig. 1.6a). These features were identified as observationally distinct from other structures in the chromosphere with physical properties, such as highly-dynamic, thin, long, and bright appearance against the dark internetwork background. These structures occur in "hedge-rows" which are bright/thin in Ca II passband, bright/thick/higher in Ly-α, and blurry/dark in Hα wavelengths. It was suggested by Rutten (2006) that these differences might be the result of radiative-transfer effects and local transition-region conditions, however, De Pontieu et al. (2007c) advocated these observed structures to be type-II spicules.

6. **X-ray jets:** Active Region (AR) jets or X-ray jets are the high-energy counterparts of the dynamic features observed in the chromospheric and lower coronal atmosphere (Fig. 1.6b). Primarily, these structures around ARs were first reported by Shibata et al. (1992); Shimojo et al. (1996) using the YOHKOH's Soft X-ray Telescope (SXT), though recently, these were found ubiquitously in quiet-Sun and coronal-hole regions as well (Raouafi et al., 2016). However, irrespective of their location, these structures are observed in X-rays as bright-streaks with corresponding foot-point brightening. Statistically, the average length of these structures is around 15 Mm, lifetimes of duration ranging from 100 sec to $\sim$4 hours, velocities around 100-400 km/s (Shimojo et al., 1996). The estimated energy associated with these jet-eruptions is of the order of $\sim 10^{26-29}$ (Pucci et al., 2013; Shimojo and Shibata, 2000). To explain the origins of these X-ray structures, earlier studies proposed the emerging flux model, which describes the reconnection between the newly emerging flux-elements with the ambient coronal magnetic fields (Shibata et al., 1992). Moreover, newer reports

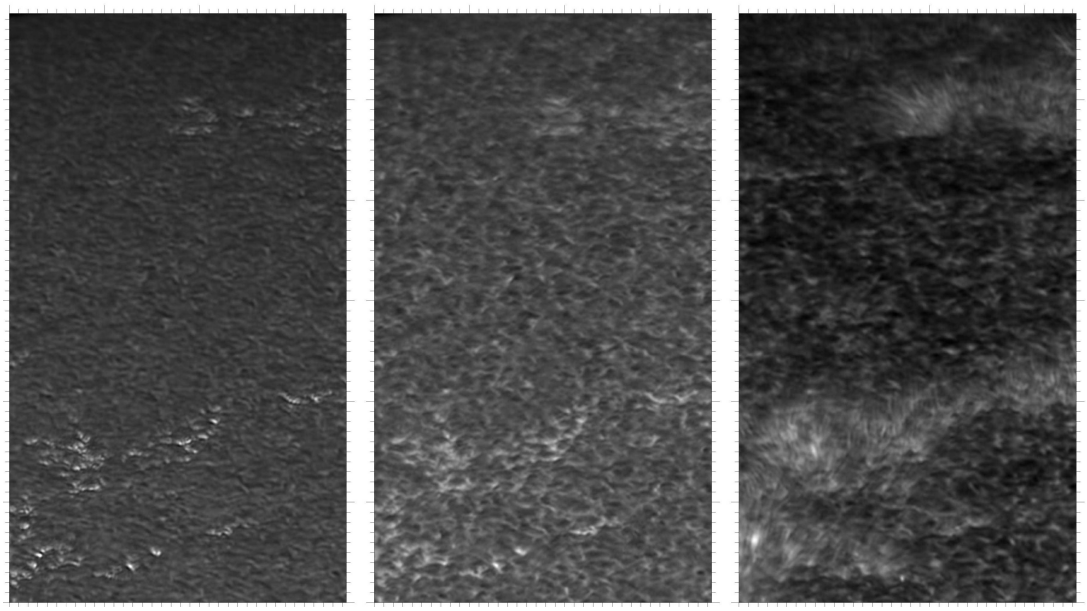

(a) G-band, Ca II H wing and core images of a region, close to the solar limb, taken from the Dutch Open Telescope (DOT). The magnetic network can be seen as bright patches in G-band and Ca II H wing images, along with long, "straw" structures in Ca II H core image. Image credit Rutten (2006)

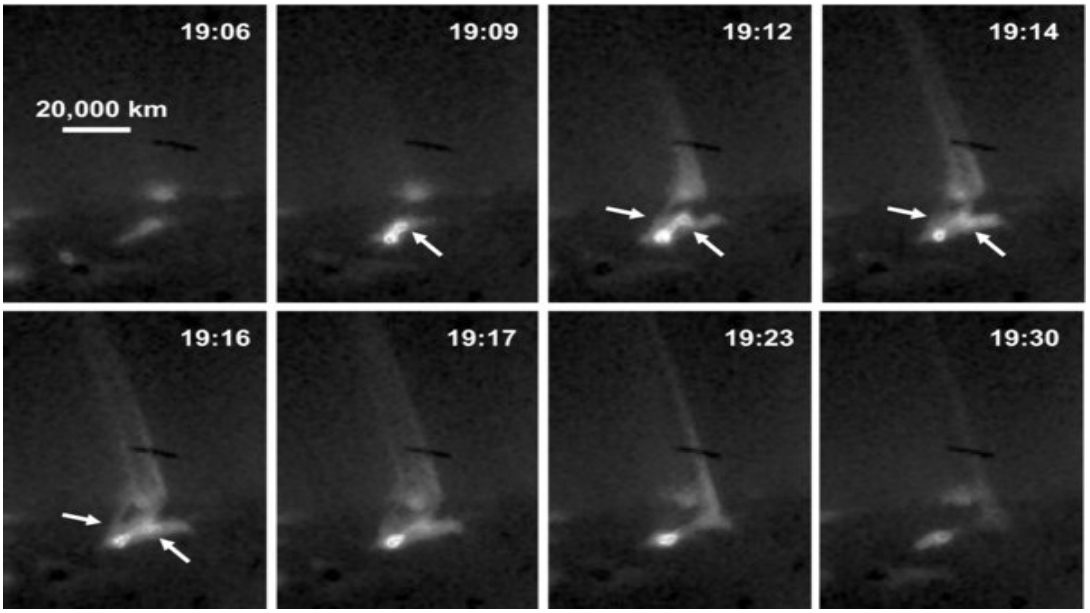

(b) Example of a blowout jet observed in the coronal X-ray emissions from *Hinode*/XRT. Foot-point brightening and the associated filament/arch-like structure is clearly visible, spaning up to 20 Mm. Upward directed arrows mark the brightening in the arch-structure while downward arrows directs to the lower leg of the strand features. Image credit: Moore et al. (2010)

Fig. 1.6 Examples of chromospheric "straw" structures (top), observed in Ca II H observations and the high energy coronal X-ray jet features, with the arch-filament systems and foot-point brightenings (bottom).

also suggest the occurrence of these with the eruption of small-scale filament structures in the solar chromosphere (Moore et al., 2010; Sterling et al., 2015).

For a much more comprehensive overview on the observations and associated properties of these structures, the interested reader is directed to some excellent reviews by Beckers (1972); Bray and Loughhead (1974); Raouafi et al. (2016); Rutten (2006, 2007); Sterling (2000); Tsiropoula et al. (2012).

1.4 Kinematics of spicules

Because of the complex nature of the solar interface-region, and the observational difficulties associated with the superimposed fine-scale MFT structures, the understanding and thus interpretation of the dynamical behavior in these features remained challenging. The kinematic studies of the chromospheric thin MFT structures was pioneered by W. O. Roberts[3] and his colleagues (Roberts, 1945; Roberts et al., 1949; Rush and Roberts, 1954) in their reports for the off-limb spicules. By using a coronagraph with a Lyot filter, these studies reported the rise- and fall-phase of the spicular plasma and found velocities of $\sim$40 km/s with lifetimes of about 120 sec. They concluded that the visible apex of the spicule structure reached its maximum in a 5 minutes lifetime, with the possibility that the plasma might not had shown both the rise- and fall-phase in their observational data. Similar studies on the longitudinal motions of the off-limb spicule structures were also reported by Lippincott (1957) and many others (see review by Beckers, 1968, 1972). Also, the periodic field-aligned mass flows were reported for on-disk mottle structures by Loughhead (1974).

The cross-sectional width of the spicular structures were reported since Father Secchi's first observation of these features. In his work (Secchi, 1877), by visual inspection, deduced the width of the spicules to be of the order of 100-200 km in Hα observations. Many other attempts, quoted in reviews mentioned above, listed the spicular width in the range 100-2500 km, depending on the observed wavelength, apparatus and the involved methods. However, the variations in the cross-sectional width was first reported by Mouradian (1967), where the cross-sectional width was reported to vary with a velocity of 0-70 km/s with an average of 22 km/s. This variation was also correlated with the changes in the observed intensity, as the brighter spicules shown more expansion, as compared to the dark/faded ones.

Transverse motions in spicules were reported as early as mid-1950s from the spectroscopic (Doppler velocity) studies. Michard (1954) reported root mean squared

[3] *Also credited as the first, to use the term, 'spicules' for off-limb jet-like MFT observations*

(rms) Doppler estimates of spicules, from Hα observations, of the order of about $\sim$13 km/s, observed at the poles at a height of around 5 Mm. Athay and Bessey (1964) studied these structures, both on-disk (at equator) and off-limb (at poles) and found the rms velocities in the range 4-9 km/s in Hα and D3 observations. They also discussed the role of projection effects in the measurement of the Doppler velocities for the inclined structures. However, a major impression in these earlier studies was that the spicule motion is unidirectional, i.e., it either moves upwards or downwards, but not both. The spicular plasma was believed to move in a particular direction before getting diffused in the background atmosphere. While, a small number of cases with the Doppler estimate reverse its magnitude, in Hα observations, were observed, but considered unreal. A major paradigm shift in this view came from the studies reported by Nikol'skii and Sazanov (1966), where they showed temporal variations in the estimated Doppler velocities, with a period of around 1 minute. In their analysis, the Doppler velocity magnitudes changed their signatures, which was later confirmed by Zirker (1967), for the observations of MFT structures near plage regions. These early observations on transverse motions in MFT structures continued their trend in the following decades with more reports in 1970's (Kulidzanishvili and Nikolskii, 1978; Nikolsky and Platova, 1971; Weart, 1970), in 1980's (Gadzhiev and Nikolskii, 1982; Hasan and Keil, 1984; Kulidzanishvili and Zhugzhda, 1983), and in 1990's (Papushev and Salakhutdinov, 1994). One of the first space-based observation of spicules came from De Pontieu et al. (2003a,b), where they reported periodic flows in these structures, using data from TRACE satellite, in combination with ground-based observations. Further observations in the EUV wavelengths was reported from SUMER/SoHO data by Xia et al. (2005). They reported $\sim$5 minute oscillations at solar limb locations by analyzing Doppler velocity and intensity maps for the C III 977 Å passband, with spatial resolution of around $1''$.

Earlier studies also showed strong indications of ubiquitous rotational motions in the observed spicular structures. These indications came from the large number of observed cases where the emission from spicule showed a relative-tilt in the spectrograms, measured in Hα and Ca II H/K wavelengths. Initially, tilts in spicule emission spectra were reported by Michard (1956), but the physical mechanism responsible for the tilt was not clear. It was suspected that at lower heights, similar tilts can originate from two neighboring spicules with different spectra. However, this was not the case in the reported studies from Beckers et al. (1966). They sampled the spectra at much greater heights where superimposed spicule cases could be excluded, and the individual spicule structures could be examined in spectrograms. The gradient in Doppler estimates in these cases, from examined spectrograms, could be either in longitudinal

direction (along the spicule) or in direction perpendicular to the spicule axis (across the spicule). In the first scenario, the estimated Doppler velocity would correlate well with the tilt in spectrogram, which implied the overall spicule displacement in the observer's line-of-sight (LOS). However, in the later case, if the Doppler shift did not correlated well, then could have been taken as an indicative signature for the rotation of the spicule axis. The analysis showed a disconnect in the measured Doppler velocities and the observed tilt, further strengthening the implications for spicule rotation. While Beckers et al. (1966) estimated the rotational velocity of the order of 20 km/s, Pasachoff et al. (1968) estimated the velocity, by analyzing multi-wavelength spicule observations, to be around 30 km/s for an average of 2° tilt in the spectra. Avery (1970) also analyzed spicule cases in Ca II-K wavelength and concluded the rotational behavior in spicule structures.

1.5 MHD wave-modes in spicules

Though, these '*historical*' studies (see review by; Zaqarashvili and Erdélyi, 2009) did established the fact that the MFT dynamics constitute the longitudinal or field-aligned motions (upwards and downwards), cross-sectional width variations, transverse motions (both along and perpendicular to the observer's LOS), and the rotational motions, but still, these observed '*independent*' dynamical components were only diagnosed from kinematic perspectives and not from MHD objectives. This can mostly be accounted to the limitations of the existing instrumentation and the observing facilities, with an exception of a few studies, which did attempted to investigate the periodicities in the observed dynamics, as listed above. The advent of modern ground- and space-based facilities allowed higher-resolution (spatial and temporal) data for investigations, which further helped in the progress in the understanding of the oscillatory behavior in the observed (on-disk and off-limb) chromospheric MFT features.

In principle, the MHD wave theory permits the possibility of infinite number of orthogonal wave-mode(s) in the MFT structures, categorized, in the linear domain, by azimuthal (m) and axial (k_z) wavenumbers in the thin-tube approximation, i.e., the radius of the waveguide is very small as compared to the observed length (tube-radius $\ll$ length). The waveguide is assumed to be cylindrical in geometry with the wavenumbers derived from the observed quantities, such as, frequency, phase speed, and the wavelength. Understanding the observed kinematic behavior in terms of MHD wave-mode(s) have certain advantages. Though, multiple MHD wave-modes can exist

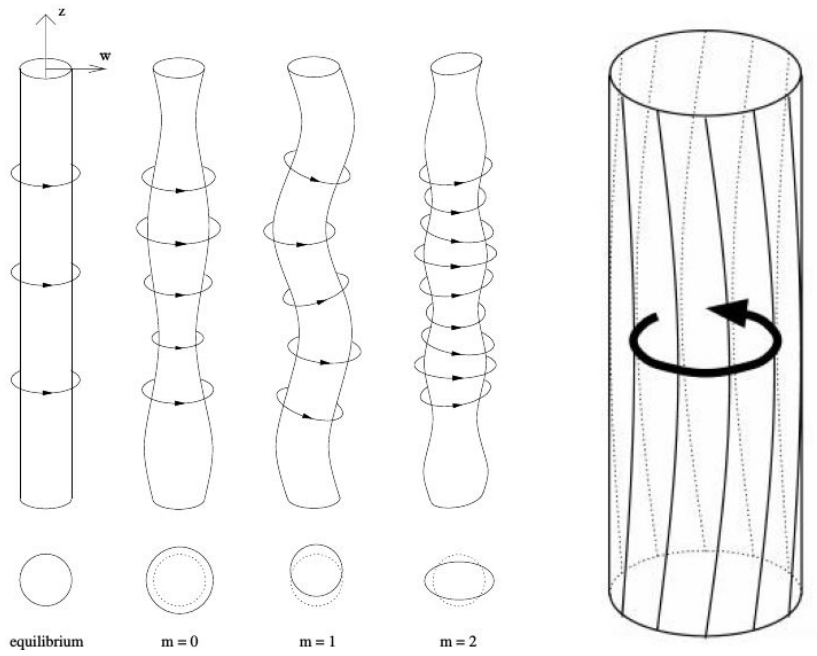

Fig. 1.7 Different possible linear MHD wave-modes (for m = 0 - 2) in a waveguide with a cylindrical geometry. Left to right: Unperturbed or *equilibrium* position/condition of the waveguide, when subjected to periodic axisymmetric cross-sectional width variations, show the sausage wave-mode, with azimuthal wavenumber (m = 0). If in case, the axis of the tube is displaced from its equilibrium position, then it is the kink wave mode, with azimuthal wavenumber m = 1. The higher-order azimuthal wavenumber m = 2, with non-axisymmetric variations in cross-sectional width, could be indicative of fluting wave modes. Last, the axisymmetric torsional Alfvén mode (m = 0), which is essentially a propagating twist of magnetic field. Image credit: Braithwaite (2006); Van Doorsselaere et al. (2008).

superimposed/confined in the MFT waveguides, the identification of the dominant wave-modes could have paramount merits for wave physics. First, the accurate identification of the confined wave-mode can allow us to more precisely estimate the energy budget available for the heating in the interface-region. Each wave-mode can have its discrete damping mechanism, through which the mechanical energy and momentum confined in the waveguide could be dissipated in the surrounding environment. Also, the wave-modes can be used for the estimation of physical parameters (density, magnetic field), which cannot be diagnosed directly from the available observational methods. Until now, due to observational limitations, the observed kinetic behavior is broadly classified in terms of three, low order, fundamental MHD wave-modes, viz, kink, sausage and torsional Alfvén (Fig. 1.7). A few reported cases for these MHD modes are summarized as follows:

1. **Kink (m = 1) wave-mode:** It is ideally the only MHD wave-mode, which independently can displace the magnetic waveguide, with magnetic tension as the

main restoring force (Goossens et al., 2009). Despite the fact that this weakly compressible, non-axisymmetric wave-mode is routinely observed as transverse displacements in chromospheric MFT structures, the interpretation of this kinematic behavior in terms of MHD kink mode was first given by Kukhianidze et al. (2006). By using the Hα data from the 53 cm Lyot coronagraph at the Abastumani Astrophysical Observatory (Georgia), they reported the transverse kink waves of wavelength $\sim$3.5 Mm with a period of 35-70 sec. De Pontieu et al. (2007d) analyzed 94 spicule cases from *Hinode*/SOT data and reported transverse oscillations with amplitudes of the order of 10-25 km/s and period of 100-500 sec. However, they interpreted the oscillations as Alfvén or Alfvénic wave-mode which was strongly debated by some studies (Erdélyi and Fedun, 2007; Goossens et al., 2014; Van Doorsselaere et al., 2008). Similar velocity amplitudes but with periods of the order of 40-50 sec were reported by He et al. (2009). Their analysis also included the estimation of the upward propagation velocity of the waves, which was found in the range 60-150 km/s. Okamoto and De Pontieu (2011) in their analysis of about 89 spicule cases, found that there exists a mixture of waves (upward, downward, superimposed or standing) in these waveguides. Around 59% of the waves were found upward propagating, 21% to be downward while around 20% were believed to be the superimposition of the two above. Measured kink wave properties in spicular waveguides were also used to probe the physical parameters of the ambient solar atmosphere (Abbasvand et al., 2015; Kim et al., 2008; Morton, 2014; Verth et al., 2011). The observed transverse kink waves were further reported by many studies in association with their reconnection-like origins, high-frequency oscillations, multi-threaded structures in recent years (Ebadi, 2013; Ebadi and Ghiassi, 2014; Ebadi and Khoshrangbaf, 2014; Ebadi et al., 2012; Shetye et al., 2016, 2017; Tavabi et al., 2015). Observations of kink wave modes were not limited to off-limb spicule structures, but also in the on-disk MFT features located near active-regions and also in the quiet-Sun chromosphere. Pietarila et al. (2011) identified kink wave signatures in high-resolution (spatial and temporal) Ca II data for fibril structures near an active-region and found the observed wave properties, very similar to those reported for off-limb spicular structures. This was followed by a series of papers from Morton et al. (2013, 2014, 2012b), who reported studies for around 1688 on-disk fibril structures with velocity amplitudes around 5-25 km/s and wave period in the range 94-130 sec, and also recently, by Mooroogen et al. (2017), which is in agreement with the wave properties reported for spicule structures. Other chromospheric features were

also analyzed in a great detail by (Kuridze et al., 2012, 2013) for on-disk mottles and rapid blue/red-shifted excursions, observed in both Hα and Ca II passbands, (Kuridze et al., 2015; Rouppe van der Voort et al., 2009; Sekse et al., 2012, 2013a,b) with transverse velocity amplitudes and periods of the same order as for the spicule structures.

2. **Sausage (m = 0) wave-mode:** This highly compressible and axisymmetric MHD wave-mode is observed as the periodic variation in the cross-sectional width of the feature and associated photometric changes. This wave-mode was first reported by Jess et al. (2012), for on-disk MFT structures using the Hα data from ROSA/DST. The sausage mode observations were found along with the kink wave mode, in agreement to their 2D MHD simulation for the foot-point driver for such motions. Similar observations were reported later by Morton et al. (2012a), also using the Hα data from ROSA/DST. They reported the concurrent observations of sausage and kink wave-modes in fibril structures, with sausage waves having period in range 135-241 sec and transverse velocities of the order 1-2 km/s. Recently, Gafeira et al. (2017a) reported the cross-sectional width oscillations, using *Sunrise* balloon experiment observations, along with the coupled intensity oscillations for on-disk slender Ca II Fibrils (SCF) structures with mean periods 32$\pm$17 sec and 36$\pm$25 sec, respectively, for cross-sectional width and intensity variations. They also concluded that both these oscillating parameters propagate with velocities of $\sim$11 km/s and $\sim$15 km/s, respectively.

3. **Torsional Alfvén (m = 0) mode:** These are *ideally* incompressible wave-modes which can exist with any wavenumber (m), and are observed as periodic axisymmetric red-blue shifts in the spectroscopic (Doppler) measurements. Since, chromospheric MFT structures are rooted in the intergranular lanes, the vortex motions at the footpoint can inject the torsionality or azimuthal shear in these structures. Jess et al. (2009), first reported torsional Alfvén oscillations for a magnetic bright point, with 180° phase-shift across the structure, with no associated intensity and transverse oscillations. De Pontieu et al. (2012) exploited the high-resolution capabilities of the CRISP and TRIPPEL spectrographs at the Swedish Solar Telescope (SST), and resolved the axisymmetric red-blue shifts in spicule structures in both Hα and Ca II H data. They interpreted the Doppler observations, aided with Monte-Carlo simulations, as signatures of torsional Alfvén waves. Torsional motions of the order of 25-30 km/s, along with transverse (15-20 km/s) and longitudinal flows (50-100 km/) were found in their studies. Similar observations for on-disk RRE/RBE structures were reported by

Sekse et al. (2013b). In their studies, they found that these ubiquitous rotational motions are observed, along with, transverse and field-aligned longitudinal flows. However, these studies (De Pontieu et al., 2012; Sekse et al., 2013b) assumed the *independent* nature of the observed kinematic components, confined in the spicular waveguides. Recently, Srivastava et al. (2017), also analyzed Hα imaging-spectroscopy data from CRISP/SST and claimed high frequency ($\leq$ 50 sec) torsional motions in on-disk spicule structures, and interpreted these as torsional Alfvén waves.

Apart from these kinematic components, the longitudinal (field-aligned) motions were also observed and reported by Pereira et al. (2012). They found that spicules (type-I) with relatively longer lifetimes (150-400 sec) in Ca II wavelength, had an upflow/downflow plasma velocities of the order of 15-40 km/s while their more energetic counterparts, type-II spicules with lower lifetime (50-150 sec) had velocities in the range 30-110 km/s. However, Pereira et al. (2014), using multiwavelength observations from IRIS spacecraft, did report that these structures, when faded in a particular passband, do reappear in the other, while reaching much greater heights (20 Mm), with longer lifetimes (500-800 sec) than previously estimated. A more comprehensive overview of the MHD wave-modes in chromospheric MFT waveguides can be found in reviews by Jess et al. (2015); Verth and Jess (2016); Zaqarashvili and Erdélyi (2009). The observed kinematic components as different MHD wave-modes are summarized in the Table (1.1) below:

Feature	Wavelength	Period (sec)	Amplitude (km)	MHD wave-mode	Reference
Spicule	Hα	60	–	–	Nikol'skii and Sazanov (1966)
	Ca II	180 - 420	–	–	Pasachoff et al. (1968)
	Hα	–	–	–	Weart (1970)
	Hα	50-70	–	–	Nikolsky and Platova (1971)
	Hα	180 - 420	–	–	Kulidzanishvili and Nikolskii (1978)
	Hα	180 - 360	–	–	Gadzhiev and Nikolskii (1982)
	Hα	300	–	–	Kulidzanishvili and Zhugzhda (1983)
	Hα	120 - 180	–	–	Hasan and Keil (1984)
	Hα	80 - 120	–	–	Papushev and Salakhutdinov (1994)
	EUV	300	–	–	Xia et al. (2005)
	Hα	30 - 70	–	Kink	Kukhianidze et al. (2006)
	Hα	30 - 110	–	Kink	Zaqarashvili et al. (2007)
	Ca II	150 - 350	200 - 500	Kink	De Pontieu et al. (2007d)
	Ca II	60 - 240	–	Kink	Suematsu et al. (2008)
	Ca II	130	1000	Kink	Kim et al. (2008)
	Ca II	180	700	Kink	–
	Ca II	170	800	Kink	–
	Ca II	48	36	Kink	He et al. (2009)
	Ca II	37	36	Kink	–
	Ca II	45	130	Kink	–

	Ca II	50	166	Kink	–
	Ca II	45±30	55±50	Kink	Okamoto and De Pontieu (2011)
	Ca II	180	725	Kink	Ebadi et al. (2012)
	Ca II	220	670	Kink	Jess et al. (2012)
	Ca II	139	630	Kink	–
	Ca II	65	160	Kink	–
	Ca II	158	410	Kink	–
	Ca II	129	380	Kink	–
	Ca II	105	200	Kink	–
	Ca II	171	190	Kink	–
	Ca II	175	725	Kink	Ebadi and Ghiassi (2014)
	Ca II	–	243±218	Kink	Pereira et al. (2012)
	Ca II	–	463±402	Kink	–
	Ca II	–	245±211	Kink	–
	Ca II	–	342±257	Kink	–
Fibrils	Ca II	135	135	Kink	Pietarila et al. (2011)
	Ca II	–	315±130	Kink	Morton et al. (2012b)
	Hα, Ca II	94±61	71±37	Kink	Morton et al. (2013)
	Hα	116±59	94±47	Kink	Morton (2014)
	Hα	130±92	73±36	Kink	–
	Ca II	83±29	– ±218	Kink	Jafarzadeh et al. (2017)
	Hα	120	–	Kink	Mooroogen et al. (2017)

RBEs	Ca II	–	300	Kink	Rouppe van der Voort et al. (2009)
	Ca II	–	200	Kink	Sekse et al. (2012)
	Hα, Ca II	–	–	Kink	Sekse et al. (2013b)
	Hα, Ca II	–	220	Kink	Sekse et al. (2013a)
Mottles	Hα, Ca II	165$\pm$51	200$\pm$67	Kink	Kuridze et al. (2012)
	Hα, Ca II	–	$\sim$172	Kink	Kuridze et al. (2013)
	Hα, Ca II	180$\pm$10	252	Kink	–
	Hα, Ca II	180$\pm$10	327	Kink	–
Fibril	Hα, Ca II	60-220 (Kink)	400 (Kink)	Kink + Sausage	Jess et al. (2012)
Fibril	Hα, Ca II	232$\pm$8 (Kink), 197$\pm$8 (Sausage)	360$\pm$120 (Kink), 315$\pm$130 (Sausage)	Kink + Sausage	Morton et al. (2012a)
Fibril	Ca II	32$\pm$17	–	Sausage	Gafeira et al. (2017a)
Spicule	Hα, Ca II	100 - 200	–	Torsional (Aflvénic)	De Pontieu et al. (2012)
RBE/RRE	Hα, Ca II	–	–	Kink + Torsional (Aflvénic)	Sekse et al. (2013b)
	Hα	<50	–	Torsional (Aflvén)	Srivastava et al. (2017)

Table 1.1 Summary of the oscillatory behaviors observed in the chromospheric MFT structures and the possible MHD wave-mode(s) associated with them. Part of the table is adapted/modified from Verth and Jess (2016); Zaqarashvili and Erdélyi (2009).

1.6 Outline of the thesis

In this thesis, the dynamical behavior of spicules are analyzed at both pixel- and tube-scale for the accurate interpretation of the confined MHD wave-modes. Novel analysis techniques are developed to combine the observed kinematics in imaging and spectroscopy to better understand the coupled plane-of-sky and line-of-sight dynamics. For the first time, proxies for the plasma and magnetic field perturbations in the ambient chromospheric environment are estimated to accurately identify the wave behavior, along with nonlinear evolution of dynamics over height and time. The newly developed technique provided an unique insight into the behavior of spicule structures, which are mathematically modeled as thin magnetic flux tubes (MFTs). Key kinematic aspects, such as, coupled rotational and transverse nature of kink wave mode, nonlinear kink wave behavior, presence of multiple wave modes (kink, sausage, and torsional Alfvén), which were only postulated in theory and simulation before, were established using the state-of-the-art observational evidence. This thesis provides a step-change in the analysis of imaging-spectroscopy data and interpretation of the observed behavior of thin chromospheric waveguides. The main chapterwise results are as follows:

Chapter 2 will discuss the imaging-spectroscopy data used in the study, Chapter 3 showcase the coupled transverse and rotational (LOS-dependent) nature of the kink wave-mode, and also, its observational differences from torsional Alfvén wave-mode through ambient plasma and magnetic pressure perturbations. The results confirm the coupled transverse and rotational components associated with kink wave mode when observed from different view-angles. Chapter 4, highlights, the coupled nonlinear MHD kink behavior of the spicule dynamics, and its phase relationship with the other observed kinematic components (cross-sectional width, intensity, azimuthal shear/torsion). Chapter 5, emphasizes the evolution of the out-of-phase, transverse components in the observer's POS and LOS, along with complex, non-helical motions, due to the presence of multiple wave modes in the structure. Finally, Chapter 6 concludes the main results from the thesis and also the future/ongoing projects.

Chapter 2

Observations

2.1 Background

To acquire a good quality dataset for the study of the dynamics of the small-scale structures is not an easy task. An observer's ideal wish-list for such a dataset typically consists of the highest possible spatial and temporal resolution with ample spectral line-scans, in optimal/multiple wavelengths to capture the observed phenomenon in a great detail and serve the scientific needs. This further depends upon the target layer (photosphere, chromosphere or corona) in the solar atmosphere, region (active or quiet-Sun) and the location (near-disk or at the limb) on the Sun. Unfortunately, all these requirements are difficult to be met at the same time and often results in the conflicting scenarios, which depend upon the instrumentation and the observational (*e.g.,* seeing conditions for ground-based) limitations. A higher spectral resolution can result in the lower photon flux-count for the detector, causing in an increase in the temporal resolution, in order to compensate the spatial resolution. Again, these two specifications are an utmost requirement for an effective acquisition of the small-scale dynamical behavior shown by the targeted feature(s).

However, during the past few decades, observations from a variety of platforms at ground- (*e.g.,* CRISP/SST; Scharmer et al. (2003, 2008), ROSA/DST; Jess et al. (2010), IBIS/DST; Cavallini and IBIS Team (2004), NST; Cao et al. (2010)), air- (*Sunrise/ImaX;* Solanki et al. (2010)), rocket-borne (*e.g.,* Hi-C; Cirtain et al. (2013), CLASP; Kano et al. (2012)) and space-based facilities (SOHO; Domingo et al. (1995), *Hinode*; Kosugi et al. (2007), SDO; Pesnell et al. (2012), IRIS; De Pontieu et al. (2014)), along with the state-of-the-art processing techniques have provided an enormous wealth of information about the dynamic phenomena that occur in the solar atmosphere over a wide range of spatial, spectral and temporal scales. This chapter, summarizes

the telescope and the instrument used to acquire the data, post-processing techniques involved, and the observed spicule cases, along with their selection criterion and fundamental physical properties (height, lifetime, length, etc.).

2.2 Ground-based observations

Despite the fact that the ground-based observations suffer from the 'seeing-conditions' and the wavelength filtering by the Earth's atmospheric blanket, there are certain relative advantages in using ground-based facilities for the study of the small-scale features in the solar atmosphere. One of the biggest advantages of any ground-based observations, other than the highest possible angular resolution, is the 'customization' of the dataset, to suit the needs of the scientific query. The observer can choose from a combination of imaging, spectroscopy and polarimetry, to access (directly or indirectly) the physical behavior of the feature of interest. Another benefit is from the possibility of upgradation/combination of the instruments at much lower costs when compared to a space-based facility. This thesis used data from the Swedish Solar Telescope (SST), which along with the relevant post-processing techniques involved, are described below.

2.2.1 Swedish Solar Telescope (SST) and the CRISP instrument

The data used in the study are taken from the Swedish Solar Telescope (SST), located on the island of La Palma, at an altitude of around 2400 meters above the sea-level in a 17 meter high tower (Fig. 2.1a). The current facility is the successor of the Swedish Vacuum Solar Telescope (SVST) which became unoperational in August, 2000. SST has an aperture of 98 cm and is equipped with the state-of-the-art modern back-end instruments and Adaptive Optics (A.O.) systems. This 21^{st} century observatory achieved its first-light in March, 2002, with a limited initial set-up. The telescope is a refractor-type with a vacuum tower design. Light enters from the top of the telescope, and is focused for all observable wavelengths by a Schupmann corrector, before being fed onto an observing table. The light then passes through a series of beam-splitters and pre-filters to isolate the intended wavelengths for the observational run. A portion of this light is then passed into the A.O. systems to correct the effects of the seeing throughout the data collection period. The telescope has three major instruments, namely, the CHROMospheric Imaging Spectrometer (CHROMIS), installed in 2016 which operates at wavelengths in the range 380-500 nm, the CRisp Imaging SpectroPolarimeter (CRISP), installed in 2008 which operates from 510 to

860 nm, and the TRI-Port Polarimetric Echelle-Littrow (TRIPPEL), which observes in the wavelength range of about 380-1100 nm.

The data used in this thesis were obtained from the CRisp Imaging SpectroPolarimeter (CRISP) instrument (Fig. 2.1b). The CRISP instrument is usable for the wavelength range 510 – 860 nm and has two Fabry-Pérot Interferometers (FPIs) with a field-of-view (FOV) of $60'' \times 60''$ and a pixel size of approximately $0.059''$. The A.O. system for the telescope consists of a tip-tilt mirror and a deformable mirror to compensate the effects of atmospheric distortions in the images. Details on the instrument are discussed by Scharmer et al. (2008).

2.2.2 The Hα spectral line and data

The wavelength used for the observations is the Balmer series Hα (656.3 nm) spectral line, which is considered to be an excellent tool to understand the behavior of the structures in the solar Interface-region (Leenaarts et al., 2007; Rutten, 2008). The Hα spectral profile is usually an absorption line with the wing-positions highlighting the photospheric contributions when observed on-disk, while the line-core samples the chromosphere (Fig. 2.3). The Hα (656.3 nm) spectral line forms due to the transition of the electrons in between the second and the third energy levels (orbits/shells) of a hydrogen atom. These transitions of electrons in the hydrogen atom primarily follow the mechanisms involving the radiative ionization and recombination of the energy level populations. These mechanisms prevail over other processes that involve collisional transitions between the energy levels, thus making the Hα line more sensitive to the mass density, rather than the local temperature. The regions responsible for the ionization (Balmer and Paschen continua) usually originate in the lower to the middle photosphere and remain nearly constant, irrespective of the chromospheric dynamics in the quiet-Sun environment. It is only for the energetic events (*e.g.,* flares) that when the high-energy electrons are injected into the chromosphere, the Hα line responds to the temperature variations and becomes an emission line. Furthermore, observationally, the Hα chromosphere is finely structured with the magnetic fields highlighted by the absorption of the plasma (Leenaarts et al., 2012) and exhibiting rich dynamics that could be diagnosed with imaging-spectroscopy techniques.

The imaging-spectroscopy technique provides an important diagnostic edge to understand the dynamical behavior of the feature in both the observer's line-of-sight (LOS) and the plane-of-sky (POS), along with other key physical information. The Hα imaging-spectroscopy data (Fig. 2.2) taken in between 07:15-07:48 UT, June 21, 2012, targeting an Active Region (NOAA AR11504) which consisted of 2 sunspots at

(a) The Swedish Solar Telescope (SST) at the island of La Palma, Canary Islands. The primary mirror of the telescope can be seen at the top of the tower building. The building structure itself harbors the vacuum tower beneath it. (Image courtesy: Nabil Freij.)

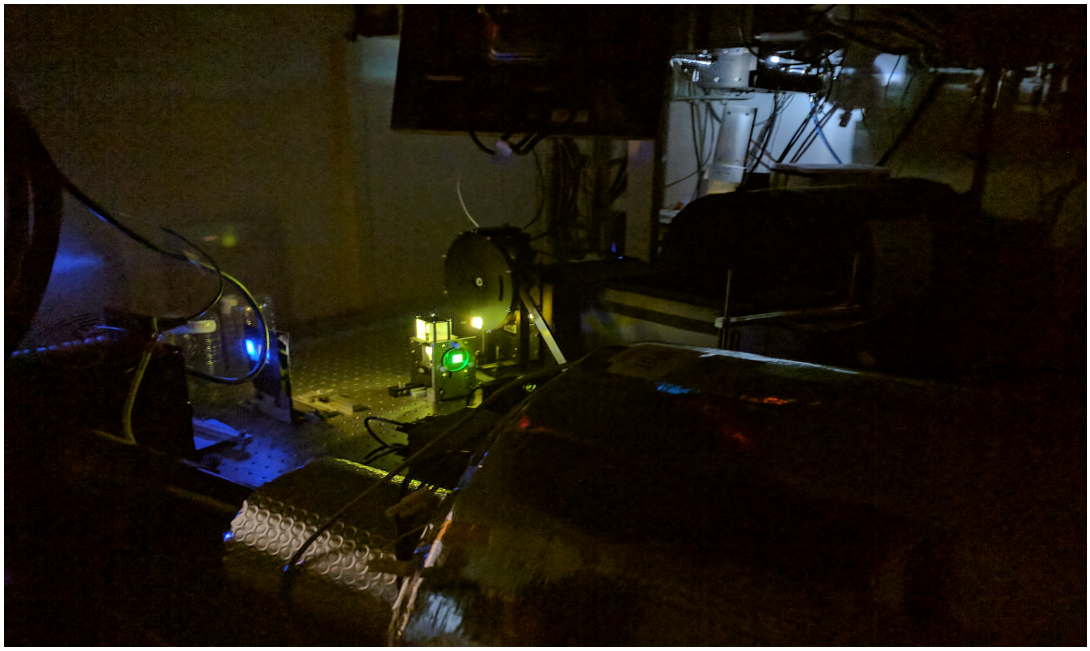

(b) The CRisp Imaging SpectroPolarimeter (CRISP) instrument is shown along with the filter wheel. (Image courtesy: Nabil Freij.)

Fig. 2.1 The Swedish Solar Telescope (a) and the CRISP instrument (b) facilities used to obtain the imaging-spectroscopy Hα data used in the thesis.

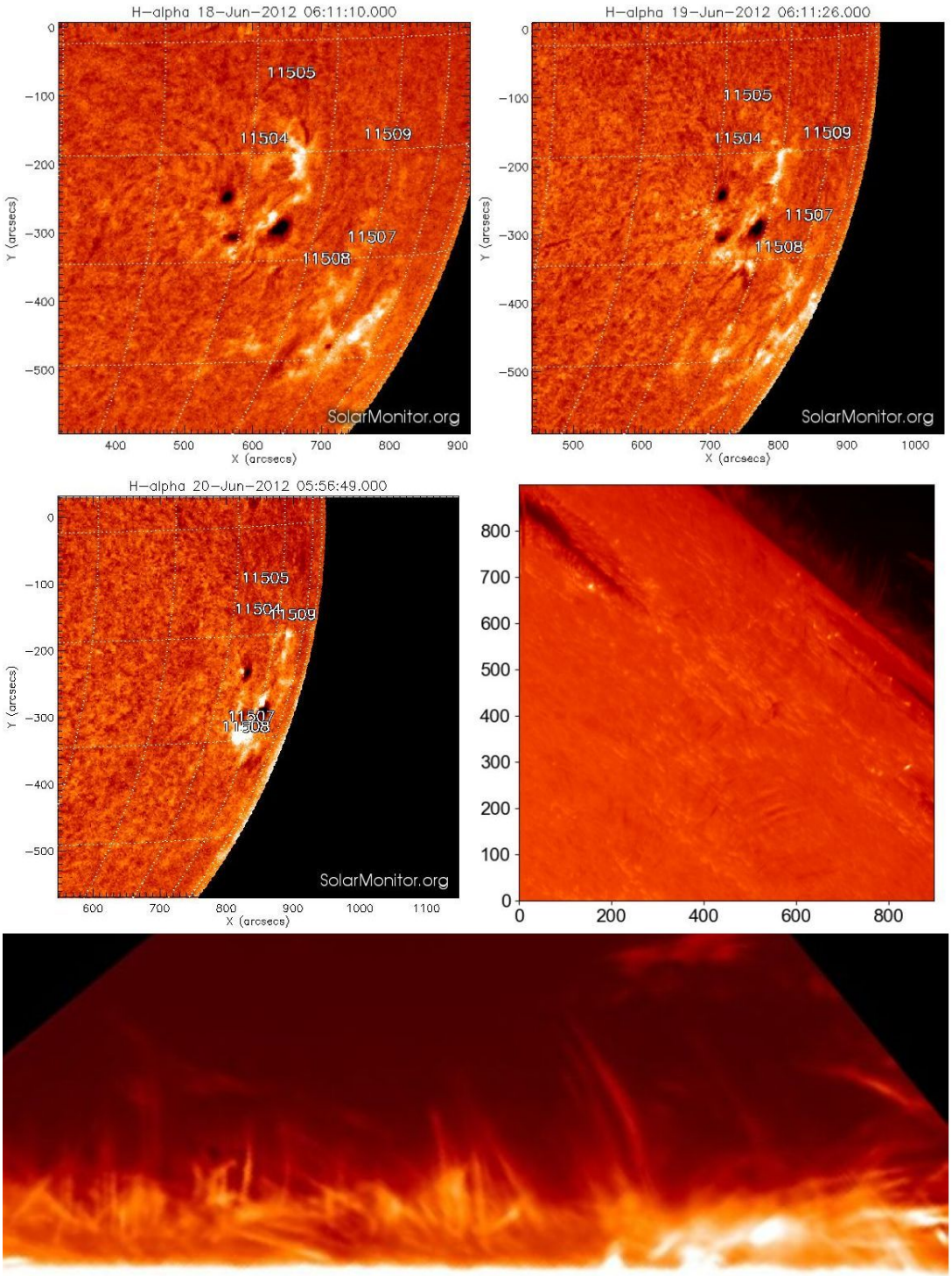

Fig. 2.2 The target region over a course of a few days before the CRISP/SST data were taken. Top panels show the Hα images of the sunspots (taken from www.solarmonitor.org), on 18 and 19 June, 2012, which were the target of CRISP/SST observations used in the thesis. Middle panels show the region on 20 June, 2012, along with the CRISP/SST field-of-view (FOV) at the limb on 21 June, 2012. Bottom panel shows the Hα limb observations with the spicule structures analyzed to understand the dynamical behavior.

the limb position (heliocentric coordinates with respect to disk center, hereby denoted as: $\Theta = 893''$, $\Phi = -250''$). The AR was scanned using 31 equally spaced line positions with 86 mÅ, steps from -1.376 to +1.29 Å, relative to line center, along with additional 4 positions in the far blue wing from -1.376 to -2.064 Å.

The spicule structures are clearly visible at the limb, though it is not apparent from the observations that whether the structures are rooted in an active or quiet-Sun region. CRISP/SST field-of-view shows the active regions and also the plage regions around them, but the spicules are not near any of these and might be originating from somewhere behind. Other ground-based full disk images of previous days were examined and are concluded that the spicules might have originated from a quiet-Sun region. This information is useful for the background magnetic field approximations used in Chapter 3.

2.2.3 Post-processing methods

Once the data are acquired by the instrument at the telescope, they have certain imperfections due to the atmospheric and/or instrument factors. The distortion and/or blurriness in the acquired data are largely due to the turbulence in the Earth's atmosphere, which, to most extent, is controlled by the A.O. system available at the observation site. However, still there are certain essential steps needed to minimize/remove the imperfections and restore the image. The standard procedures (de la Cruz Rodríguez et al., 2015) available in the image pipeline for CRISP data were implemented. Generally, these preprocessing steps include taking target, continuum, flat-fields and dark images, which are described as follows:

1. **Target:** Generally, a target grid is located at the primary focal plane, in front of the observing instrument. These frames show a grid of lines, which are used to focus and align the cameras, and are important for further image reconstruction.

2. **Continuum:** These data are taken with the same parameters as with sunlight but using a continuum source, in order to test the transmission of the scanning narrow-band channel.

3. **Flat-fields:** These are the image frames taken to account the sensitivity at each pixel. The camera is operated with the same scanning parameters, but by avoiding any solar structures. The telescope is pointed at a random location around the solar disk center at quiet-Sun regions.

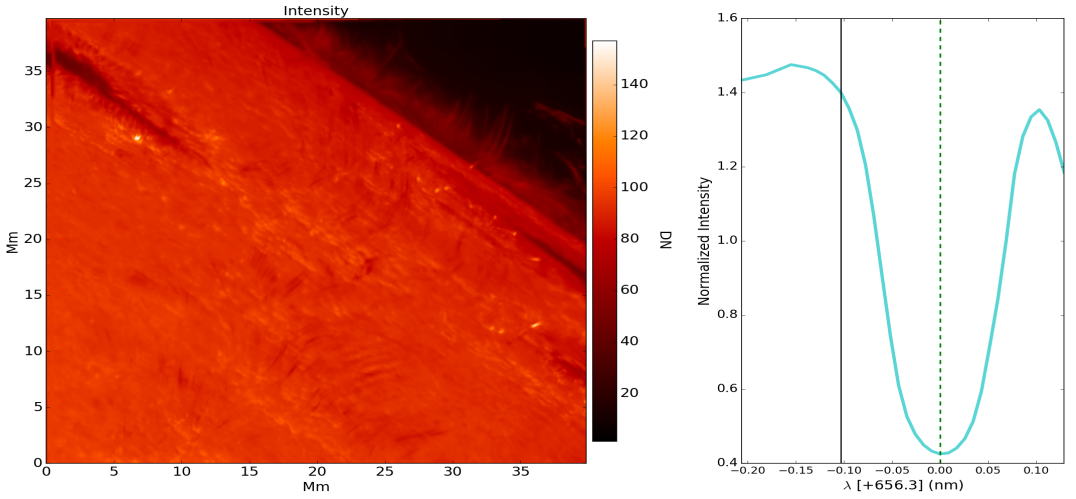

(a) CRISP/SST field-of-view (FOV) image at the line-scan (λ_s) position -1.032 Å from the line-core, showcasing the spicule structures at the limb and also contributions from the photosphere.

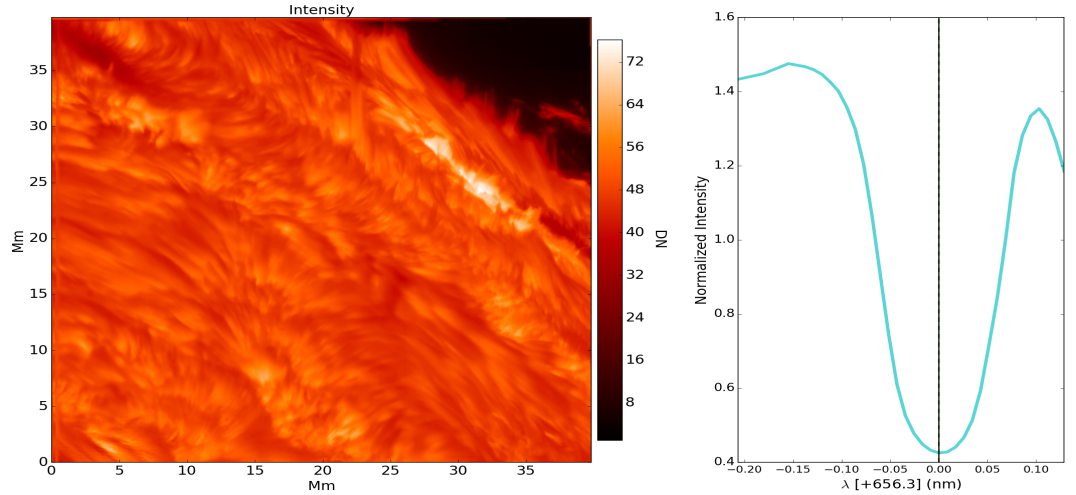

(b) CRISP/SST field-of-view (FOV) image at the Hα line-core, showing the solar chromosphere.

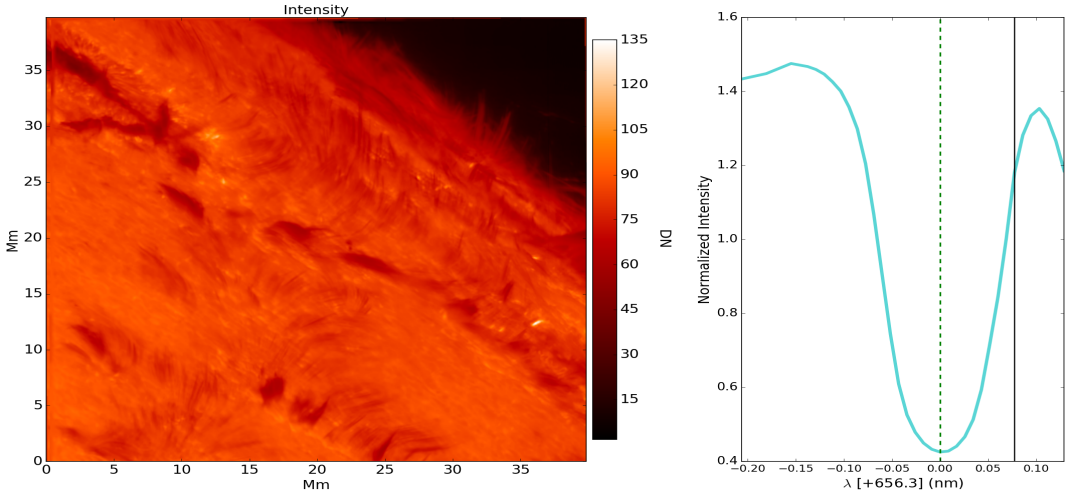

(c) CRISP/SST FOV at the line-scan (λ_s) position +0.774 Å from the line-core.

Fig. 2.3 Panels showing (a-c) the samples of imaging-spectroscopy data taken on June 21, 2012, at three line-scan positions of the Hα spectral profile, at both wing and core positions, respectively. Contributions from the photosphere and the chromosphere are clearly visible with fine-scale spicule structures on-disk and at the limb. Dashed vertical-lines in the right panels mark the position of the line core, in the plot of the Hα line-profile.

4. **Darks:** These are the random photon-noise that is present within the camera. These are collected by operating the camera with closed lens and same exposure as that for science observations. This instrument effect is then removed from the scientific data.

The instrument effects are then reduced in the pre-restoration images by using the following:

$$\text{Reduced Frame} = \frac{(\text{Raw Frame}) - (\text{Mean Dark})}{(\text{Mean Flat field}) - (\text{Mean Dark})}$$

The data obtained from the observations are further processed by image reconstruction techniques. These include speckle and blind deconvolution methods, which are used to minimize the aberrations in the obtained data to achieve the spatial resolution close to the diffraction limit of the aperture of the telescope. The data, used in the thesis, were processed using the Multi-Object Multi Frame Blind Deconvolution (MOMFBD; van Noort et al., 2005) image restoration algorithm.

2.3 Candidate spicule cases

The final science-grade data of $\sim$30 min duration had a pixel size of 0.059$''$ ($\sim$43 km), angular-resolution of 0.13$''$ ($\sim$95 km), and a cadence of 7.7 sec. Note that for this dataset, there were no simultaneous observations in the continuum available to normalize the Hα spectral line profiles to. The data at the solar limb, showed spicule structures (Fig. 2.3) at far-wing positions in the Hα line profile. Spicules appear in clusters or bushes which makes identification and tracking of individual structures a challenging task. Eight spicule structures (Fig. 2.4) were selected for the analysis, presented throughout this thesis, on the basis that they were distinct enough from the background and other features in the image frame during their lifetime in the respective line-scan positions. The observed physical parameters (*e.g.,* lifetimes, inclination, length etc.) are given in Table 2.1 and were found consistent with previous reports (Tsiropoula et al., 2012). The average lifetime of spicules under study was about 127 sec while the projected inclination angle with respect to the vertical was about 25.47°. Subsequent space- and ground-based, full-disk images from earlier dates (Fig. 2.2) support the fact that the observed off-limb spicules originated from a quiet-Sun region, nearly along the same projected LOS as the observed active region, although this could not be validated from the obtained ground-based telescope data used in the thesis.

In Table 2.1, λ_s is the line-scan position from Hα line core, used in this study, while T_i is the time when a spicule first appeared in the observed line-scan position while T_{tot} is the total lifetime of the spicule structure. Apparent visible geometric length (from foot-point to apex) and apex-height (above the visible chromosphere), of the spicules under study are shown in the next columns. Inclination angle indicates the tilt of spicules w.r.t. the vertical. For spectral analysis in the subsequent chapters (4 and 5), following the Nyquist criterion, the theoretical pixel (cadence) resolution allowed us to detect MHD waves in the spicular waveguide with wavelength longer than 86 km (15.4 sec).

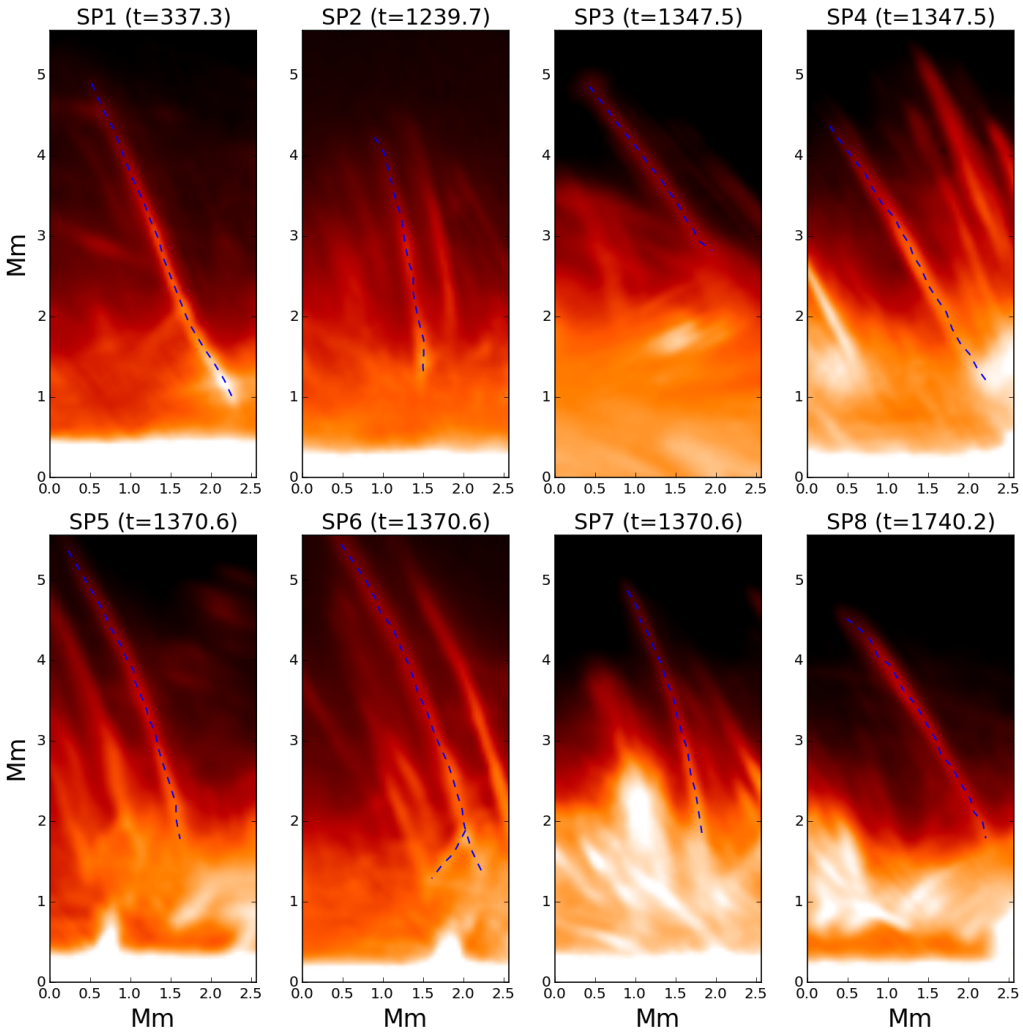

Fig. 2.4 Panels showing examples of Hα limb spicules (marked by the dashed line with physical properties in Table 2.1), at different line-scan positions, along with the time (in seconds) of first appearence (since the start of the observation), taken in between 07:15-07:48 UT, June 21, 2012. Features were selected for least possible superposition from any nearby structures during their lifetime in observed line-scan positions. In this thesis, two spicules are discussed in detail, in Chapter 3, as being representative examples of having their bulk transverse motion mostly in the POS (SP5) or along the LOS (SP8). Spicule (SP1) is used as a case study for the next consequent Chapters (4 and 5).

Table 2.1 Physical properties of the eight spicules analyzed for the dynamical behavior and associated magnetohydrodynamical (MHD) wave-modes. The estimation of velocities in both the observational planes (plane-of-sky [POS] and line-of-sight [LOS]) are discussed in detail in Chapter 3. The dominant plane of transverse motion for the given velocity range is shown in the last column. The table is adapted from Sharma et al. (2017).

Spicule	λ_s (Å)	T_i (min)	T_{tot} (s)	Length (Mm)	Height (Mm)	Inc. Angle (°)	POS_{vel} (km/s)	LOS_{vel} (km/s)	$Plane_{trans}$
SP 1	-1.204	5.9	100.1	4.1	4.9	23.6	-11.6 - 16.7	-37.1 - 25.0	LOS
SP 2	-1.209	19.5	84.7	2.5	4.1	13.0	-5.6 - 11.1	-13.5 - 24.1	LOS
SP 3	+0.430	21.8	92.4	2.2	4.8	35.7	-16.7 - 16.7	-13.0 - 44.7	LOS
SP 4	-1.032	21.9	61.6	3.7	4.4	32.2	-16.7 - 27.9	-8.8 - 1.8	POS
SP 5	-1.032	21.6	215.6	3.8	5.3	21.4	-27.9 - 33.5	-12.0 - 10.0	POS
SP 6	-1.118	22.3	123.2	3.8	5.4	24.5	-16.7 - 22.3	-8.2 - 12.4	POS
SP 7	-1.204	33.5	84.7	2.5	4.4	20.2	-11.6 - 11.6	-22.9 - 29.5	LOS
SP 8	-0.946	25.2	254	3.1	4.4	33.0	-5.6 - 11.6	-17.9 - 29.3	LOS

Chapter 3

Dynamical behavior at pixel-scale: Kink versus Torsional Alfvén[1]

3.1 Background

Spicules show transverse oscillations that are ubiquitously observed in the solar atmosphere from both ground- and space-based observatories (De Pontieu et al., 2007d; Ebadi and Ghiassi, 2014; Kukhianidze et al., 2006; Rouppe van der Voort et al., 2009; Tavabi et al., 2015). It is believed that these oscillations are due to the confined magnetohydrodynamic (MHD) kink wave-mode in the spicular waveguides. Since, it is the only independent wave-mode that can displace the axis of the magnetic waveguide as a whole (Edwin and Roberts, 1983), it is also the easiest wave-mode to be detected in the solar observations. However, kink wave-mode suffers from a popular misconception that it has only the transverse component associated with it, without the involvement of any other motions.

It is analytically and numerically shown (see e.g., Goossens et al., 2014) that the MHD kink-mode is transverse within the tube boundary along with the dipolar external plasma displacement-field. This indicates that the overall displacement-field of the waveguide due to the kink-mode is actually the sum of both transverse (internal) and rotational (external) motions, whose spectroscopic profiles depend strongly upon the observer's line-of-sight (LOS). Spectroscopic (Doppler) observations show the LOS dependent red-blue axisymmetric profiles for the transverse kink-mode, similar to those from the $m = 0$ Alfvén wave-mode. Observations reveal that chromospheric spicules display transverse kink motions, it is thus possible that the Doppler signatures

[1]This chapter is based on **Sharma, R.**, Verth, G and Erdélyi, R., 2017, "Dynamic Behavior of Spicules Inferred from Perpendicular Velocity Components", *The Astrophysical Journal*, **840**, 2.

for both kink and torsional Alfvén wave-modes can show resemblance and could lead to the misinterpretation of the dominant wave-mode and is a subject of a heated debate (Erdélyi and Fedun, 2007; Erdélyi and Taroyan, 2008; Goossens et al., 2014; Van Doorsselaere et al., 2008).

The aim of this investigation here is to combine the line-of-sight (LOS) and the plane-of-sky (POS) velocity components, using the high spatial/temporal resolution Hα imaging-spectroscopy data from the CRisp Imaging SpectroPolarimeter (CRISP) based at the Swedish Solar Telescope (SST) to achieve a better insight into the underlying nature of these motions as a whole. Though, imaging and spectroscopy data were analyzed before separately, in the previous studies for the wave-mode identification, they lacked a combined overview of the confined wave dynamics. The estimated 3D velocity vectors from the imaging and spectroscopic data and the other derived quantities (e.g., magnetic pressure perturbations) were used, for the first time, to identify the MHD wave-mode(s) responsible for the observed spicule motion. A number of independent examples were examined where the spicule bulk transverse motion is either dominant in the POS or along the LOS of the observer.

In this chapter, we will discuss the 3D velocity vector reconstruction for spicule structures. The newly developed technique provided the much looked-after prospect into the fine-scale time/space plasma evolution of the coupled transverse and rotational motions in spicules and the identification of the confined wave-mode, observed in these structures. It is, here, shown that the counter-streaming action of the displaced external plasma due to spicular bulk transverse motion had a similar Doppler profile to that of the $m = 0$ torsional Alfvén wave when this motion is predominantly perpendicular to the LOS. Furthermore, the inferred magnetic pressure perturbations supported the kink wave-mode interpretation of the observed spicule bulk transverse motion rather than any purely incompressible MHD wave-mode, e.g., the $m = 0$ torsional Alfvén wave.

3.2 Methods

The imaging-spectroscopic data is essentially 4-dimensional (4D), at each pixel, with 2 spatial (x,z), one spectral ($\lambda(I)$, taken as -y) and a temporal (t) dimension, projected on a 2D grid. This information is used to derive the perpendicular dynamical components in the observer's LOS and POS planes. The integrated-intensity (imaging) data at any particular line-scan position, where the spicule structure had a clear contrast to the background emission, over time (x,z,t) is used to estimate the transverse POS motions (V_x, V_z), while spectroscopic data (x,y,t) is used for the Doppler velocity (V_y)

estimations for each frame. The observed spicule structures extend from the upper photosphere to the lower corona and with an inclination angle relative to the plane of the photosphere, indicative of the local magnetic topology. The observed inclination can further influence the observed brightness, apparent height and the Doppler velocity (Athay and Bessey, 1964) of the feature, as discussed in the previous chapter. It must be noted that spicule inclination depends strongly on the observed location (poles or equator), with higher inclination angles (w.r.t the normal) at the equator. These can have profound effects on the observed dynamical behavior and the associated wave physics (*e.g.*, phase speeds, cut-off frequencies). Figure 3.1 depicts a cartoon of a 3D spicule structure whose LOS integrated-intensity is projected on to a 2D image plane, along with the co-ordinate system used in the thesis and the resultant velocity vectors from the estimated velocities in the perpendicular planes (POS-LOS) of observations.

3.2.1 Estimation of POS velocity components

The x- and z-components of the velocity vectors in the POS domain were estimated from the contrast-enhanced intensity images, using the Fourier Local Correlation Tracking algorithm (FLCT; Fisher and Welsch, 2008). The original concept of FLCT is based on the study of November and Simon (1988) and was later improved by Fisher and Welsch (2007). This method relies on the cross-correlation of the intensity features observed in the successive image frames to estimate the POS motions. For any two given images $I_1(x,z,t_1)$ and $I_2(x,z,t_2)$, a region (sub-image) is selected, defined by the Gaussian window, for which the intensity variations over the spatial scales is estimated, which for the given time difference, provides the velocity vectors. This process is repeated by varying the pixel location for the entire image. However, it must be noted that, like many other optical-flow estimation methods, the FLCT algorithm also has certain inherent limitations. The main assumption for this technique is that any variation in the pixel intensity-value is entirely due to the plasma motion and not because of any thermal/seeing changes. Further, utmost caution is to be exercised, in case, multiple features are present in the observer's LOS, restricting the use of this technique for only the least superimposed structures present in the dataset. Three input parameters are generally required for the FLCT algorithm to estimate the velocity; a sigma value, that specifies the size of the window for correlation function, a minimum intensity threshold and a function 'K' which serves as a low-pass filter to reduce the high-frequency noise. These input parameters for the FLCT routine were rigorously tested by varying the region enclosed by the sub-image, by changing the width of the Gaussian window and/or sigma parameter. Also, an artificial shift was introduced in the

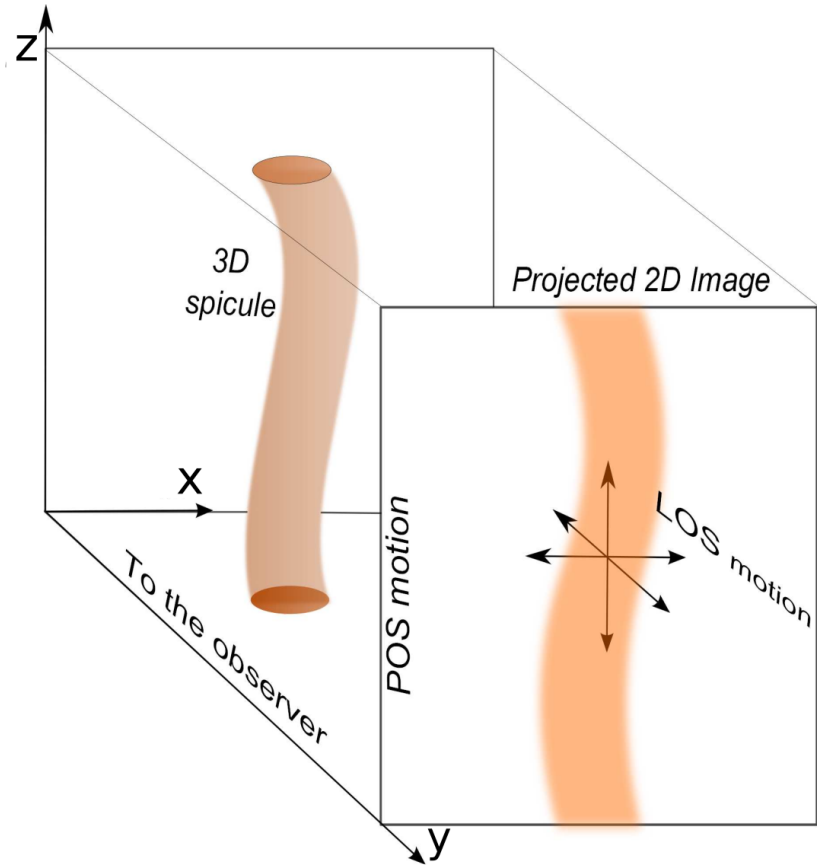

(a) A cartoon depiction of the LOS-intergrated spicule intensity projected on to a 2D image plane. Here, the spicule is projected on to the xz-plane with z-axis normal to the observed limb/surface and y-axis along the observer's LOS. The actual 3D plasma velocity is the resultant of the estimated LOS and POS components at each pixel. Figure adopted from (Sharma et al., 2017).

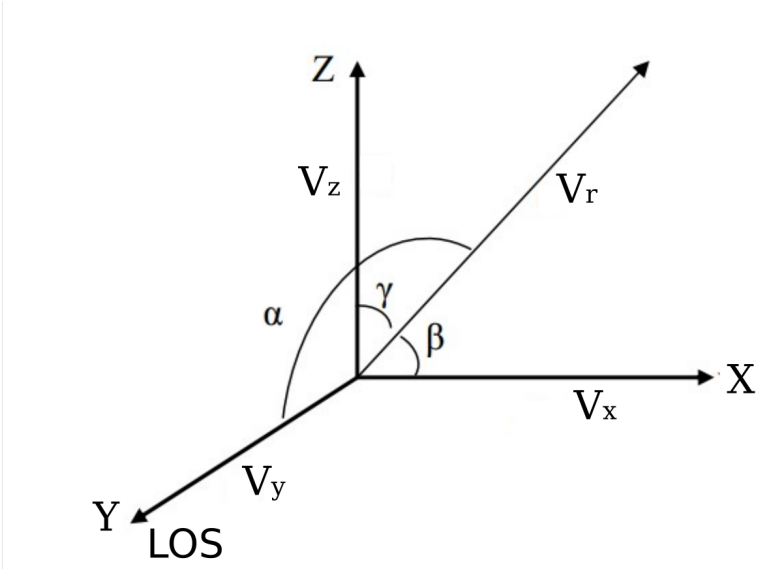

(b) Representation of the coordinate system in which the resultant velocity vector ($\vec{V}_r$) is estimated from the POS ($\vec{V}_x, \vec{V}_z$) and LOS ($\vec{V}_y$) velocity components. The observer's LOS is along the y-axis. The inclination of the resultant vector, with both planes of observation is represented by 'γ, β' (POS) and 'α' (LOS) in this coordinate system.

Fig. 3.1 Cartoons showing the projection of the 3D spicule structure on a 2D image plane, along with the coordinate system used.

Table 3.1 List of the analyzed spicule cases and the associated FLCT parameters, with estimated POS velocity vectors

Spicules	Intensity		FLCT parameters		POS Velocity Range	
	Min (DN)	Max (DN)	σ	K	V_x (km/s)	V_z (km/s)
SP1	-682	16189	4	0.2	-11.2 - 16.7	-5.6 - 43.5
SP2	-427	6107	4	0.2	-5.6 - 11.1	-13.5 - 12.3
SP3	-1079	14733	5	0.2	-16.7 - 16.7	-13.2 - 9.9
SP4	-1177	14011	3	0.3	-16.7 - 27.9	-17.7 - 11.6
SP5	-1053	14659	3	0.3	-27.9 - 33.5	-27.8 - 22.9
SP6	-1079	14733	4	0.2	-16.7 - 22.3	-16.7 - 18.8
SP7	-439	18044	4	0.2	-11.6 - 11.6	-16.7 - 43.5
SP8	-548	16374	5	0.2	-5.6 - 11.6	-6.6 - 8.3

Note: Intensity magnitudes and other used FLCT parameters depend on the line-scan position of the respective spicule cases.

test-images to determine the most probable set of the parameters that match the shift. The time-distance analysis for the spicule structures at different heights also provided estimates for the possible spatial changes with time. FLCT parameters were updated for these changes to derive the most optimal velocity outputs for the observed features. A list of FLCT parameters used in the analysis of the observed spicule cases, with estimated POS velocity range is given in Table 3.1. Unfortunately, there are no direct methods that could estimate the errors associated with these velocity measurements, but, it is advised for the interested reader to refer to the Appendix section of Freed et al. (2016), where the uncertainties associated with the input region-of-interest (ROI) for the FLCT algorithm is discussed.

The velocity vector ($\vec{V}_x$ and $\vec{V}_z$) estimation from the two images $I_1(x,z,t_1)$ and $I_2(x,z,t_2)$, involves the following operations:

1. Computation of the sub-images: The pixel at which the velocity is to be computed, a windowing function is used to ignore the parts of the image which are far away from that pixel. This localization is carried out by multiplying each of the two images by a Gaussian of width σ, centered at the pixel location (x_i, z_i). Here, the resulting images are denoted as sub-images S_1 and S_2, and are given as:

$$S_1^{i,j}(x,z) = I_1(x,z)\ \ e^{-[(x-x_i)^2+(z-z_i)]^2/\sigma^2} \tag{3.1}$$

$$S_2^{i,j}(x,z) = I_2(x,z)\ \ e^{-[(x-x_i)^2+(z-z_i)]^2/\sigma^2} \tag{3.2}$$

2. Computation of the correlation function: For the $(i,j)^{th}$ pixel, the cross correlation function of sub-image 1 with sub-image 2 is defined by:

$$C^{i,j}(\delta x,\delta z) = \int\int dxdz\ \ S_1^{i,j^*}(-x,-z)\ \ S_2^{i,j}(\delta x - x,\ \ \delta z - z) \tag{3.3}$$

3. Estimation of the velocities: For each pair of sub-images S_1 and S_2 centered at the position (x_i,z_i), the shifts δx and δz are estimated in such a manner that it maximizes the cross-correlation function C(δx, δz). The amplitude of these shifts is then divided by the cadence ($\delta t = t_2 - t_1$) between the two images 1 and 2, for the velocity vectors determination by the FLCT routine.

$$V_x = \frac{\delta x}{\delta t}, V_z = \frac{\delta z}{\delta t} \tag{3.4}$$

3.2.2 Estimation of LOS velocity components

Various methods were tested to estimate the LOS velocity component from the Hα spectroscopy data. Preliminary estimates were done with the Dopplergram technique (Leighton et al., 1962) that uses the line-scan positions ($\pm\delta\lambda$) in red (R) and blue (B) wings of the line-profile, equidistant from the reference position or the line core (λ_c). The difference in intensity magnitudes ($R-B$) between the line-scan positions, divided by the sum of the total intensities ($R+B$) at the selected line-scan positions, provides an approximation of the Doppler shift at each pixel. However, the conversion of the estimated shift to velocity requires a careful calibration using the Hα atlas profiles from the Kitt Peak solar spectral atlas (Brault and Neckel, 1987). This posed a problem as the reference atlas is derived from averaging observations from disk center of the quiet Sun, while the data used in our study is taken for the limb. Thereafter, the Lambdameter method (Deubner, 1974) was tested over the observed line-profiles for the Doppler velocity measurements. For a given length $2\delta\lambda$, this method seeks the wavelength of the middle point of a threshold chord of the given length that fits into the line profile. It uses the inner wings to infer the Doppler shift instead of the

line-center. Generally, this method yields the intensity of the chord as well, and the series of such wavelength-intensity pairs obtained for the different values which leads to the construction of the bi-sector of the line-profile. The bi-sector of a line-profile provides much information on the velocity field and the formation of the line. This method, however, failed to work for the asymmetric line profiles present in the input ROI. Also, the observed features were resolved at the far-wings of the line-profile, which could had resulted in the erroneous estimation of the Doppler velocity.

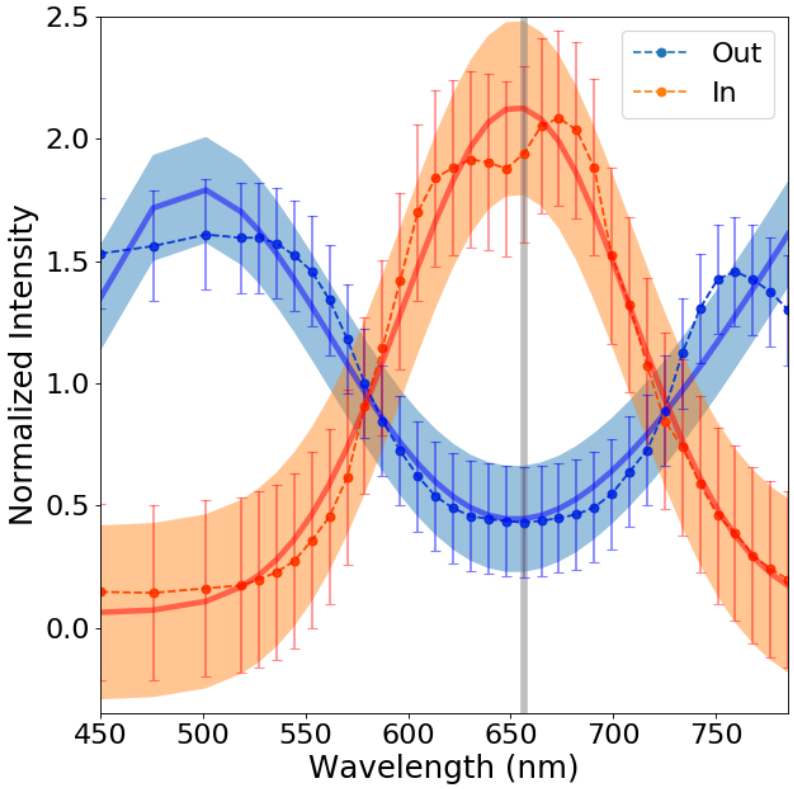

Fig. 3.2 Examples of double-Gaussian fit to the line-profile of pixels, both inside and outside the spicule structure. The dot-dash line marks the normalized intensity magnitudes at line-scan positions on either side of the line-center (marked as vertical line) with $\pm\sigma$ as error-bars. The solid line is the double-Gaussian fit with σ confidence level of overall fit as highlighted region for both line-profiles. Vertical solid like marks the position of the Hα line center (λ_c). Figure adopted from (Sharma et al., 2017).

To cope up with these problems, the spectroscopic measurements in the Hα spectral line with all 35 line-scan positions were used with a fitting procedure to estimate the LOS velocity component. The line-fitting procedures depend significantly on the shape of the line profile, thus prevented the use of a simple function. The pixels nearer to the disk had different line profiles as compared to those higher in the atmosphere. The asymmetry (Fig. 3.2) in the observed shape of the line-profiles

is primarily due to the emission and radiative transfer effects (*e.g*, central reversal) arising due to inhomogeneous structure of the chromosphere (Lites et al., 1978), at the pixel location and/or other mechanisms attributed to the multiple thread-like structure in spicular waveguide. Skogsrud et al. (2014) proposed the potential explanation for observed asymmetry as the LOS superposition effect from multiple threads in spicule structure. Similar explanation was also postulated by Antolin et al. (2014), where they showed that multiple thread-like features could be generated by a combination of the LOS angle and K-H vortices resulting from large amplitude transverse MHD wave propagation (Scullion et al., 2011). For all these reasons, a double-Gaussian function was employed for the Doppler signal estimation, given by:

$$I(\lambda) = b + I_1 \exp\left\{\frac{(\lambda-\mu_1)^2}{2\sigma_1^2}\right\} + I_2 \exp\left\{\frac{(\lambda-\mu_2)^2}{2\sigma_2^2}\right\}. \tag{3.5}$$

where $I(\lambda)$ is the discrete intensity line profile, 'λ' is the wavelength, 'b' is the background signal level, 'I' is the intensity, 'μ' is the mean of the distribution, and 'σ' is the standard deviation. The number in subscript refers to the two Gaussians. The goodness-of-fit for the double-Gaussian fit at each pixel were evaluated by Chi-squared test. The mean location between the two peaks is then subtracted from the line center of the Hα profile (656.3 nm) to estimate the shift in wavelength ($\delta\lambda$), due to LOS plasma motions. The Doppler velocity at each pixel is then estimated as

$$V_y = \frac{\delta\lambda}{\lambda} \times c \tag{3.6}$$

The estimated LOS and POS velocity vectors with mean errors $\pm$ 4.34 km/s and $\pm$ 2.76 km/s respectively, were then combined to determine the 3D velocity vector ($\vec{v_r}$), estimated as $\vec{v_r} = \sqrt{V_x^2 + V_y^2 + V_z^2}$, at each pixel (Fig. 3.3, for the SP5 ROI) projected on to the 2D image plane. With time cadence (δt), the resultant 3D velocity vector ($\vec{v_r}$) also provided the displacement ($\vec{\xi}_r = \vec{v_r}\delta t$) and acceleration ($\delta\vec{v_r}/\delta t$) magnitudes at each pixel, allowing a more detailed insight into the time and space evolution of the plasma dynamics of the spicules.

3.2.3 Estimation of other derived parameters

The spicule undergoes bulk transverse motion, therefore, it pushes the surrounding magnetic and plasma environment resulting in external pressure perturbations. This behavior is even predicted by the linear kink wave theory, although it must be noted that it is the restoring force of magnetic tension that dominates over any plasma and

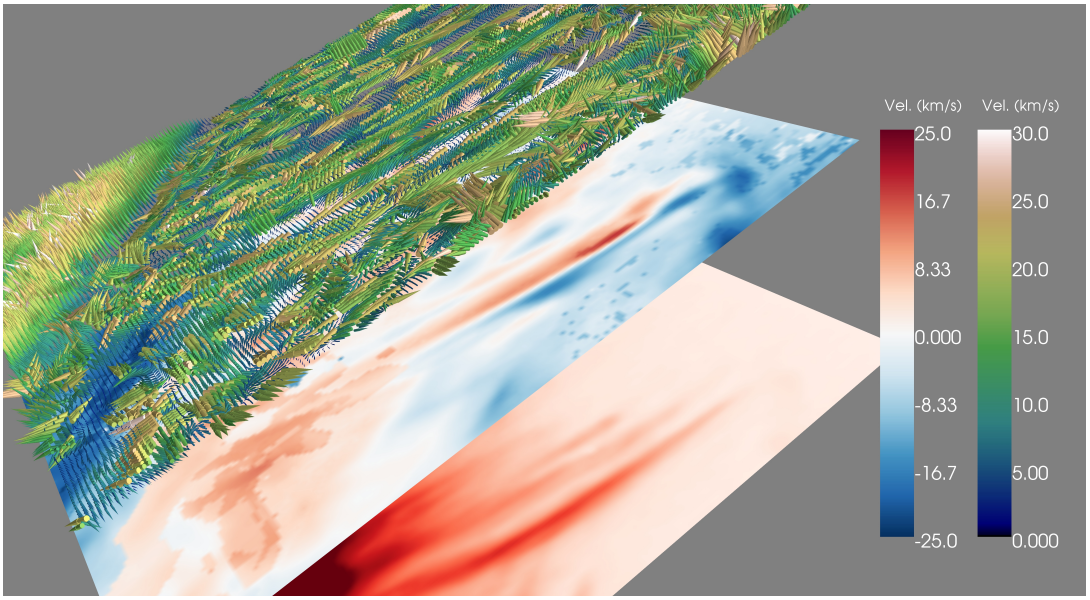

Fig. 3.3 Resultant 3D velocity vectors for the observed spicule (SP5) from imaging (POS) and spectroscopy (LOS) data. Bottom slice shows the spicule observed in Hα data while the middle slice shows the red-blue axisymmetric Doppler velocity estimates for the same. Top slice highlights the resultant velocity vectors used to derive the other estimates (acceleration, magnetic pressure perturbations), which are further employed to identify the confined wave-mode in the analysis.

magnetic pressure perturbations in this regime. Detection of these accompanying pressure changes could be taken as a supporting evidence for the spicular dynamics due to the confined kink wave-mode. These become even more important when the conventional methods to interpret the imaging-spectroscopy data provide a much confusing picture of the wave-modes in spicular waveguides. For the bulk transverse motions, orthogonal to the observer's LOS, $m = 0$ torsional Alfvén wave-mode have similar axisymmteric rotational signatures as expected from the $m = 1$ kink wave-mode (see, Fig. 3.7(c)).

Approximation of the plasma pressure variations can be derived from the estimated velocity vectors. If the total area and mass at each pixel were assumed constant, the pressure (plasma) is then directly proportional to the acceleration[6], which is estimated as the difference in velocities over time, for any two consecutive data frames. However, the estimation of magnetic pressure is not that straightforward. The information on the magnetic properties in the chromosphere is the *'missing link'* between the knowledge of the photospheric and the coronal magnetic fields. The previous attempts to measure the magnetic field strength for chromospheric structures resulted into inconsistent estimation due to the difference in the use of the observational wavelengths (Na

[6] $p = \frac{f}{A} = \frac{ma}{A} \sim a$, with, pressure ($p$), force ($f$), mass ($m$), area ($A$) and acceleration ($a$)

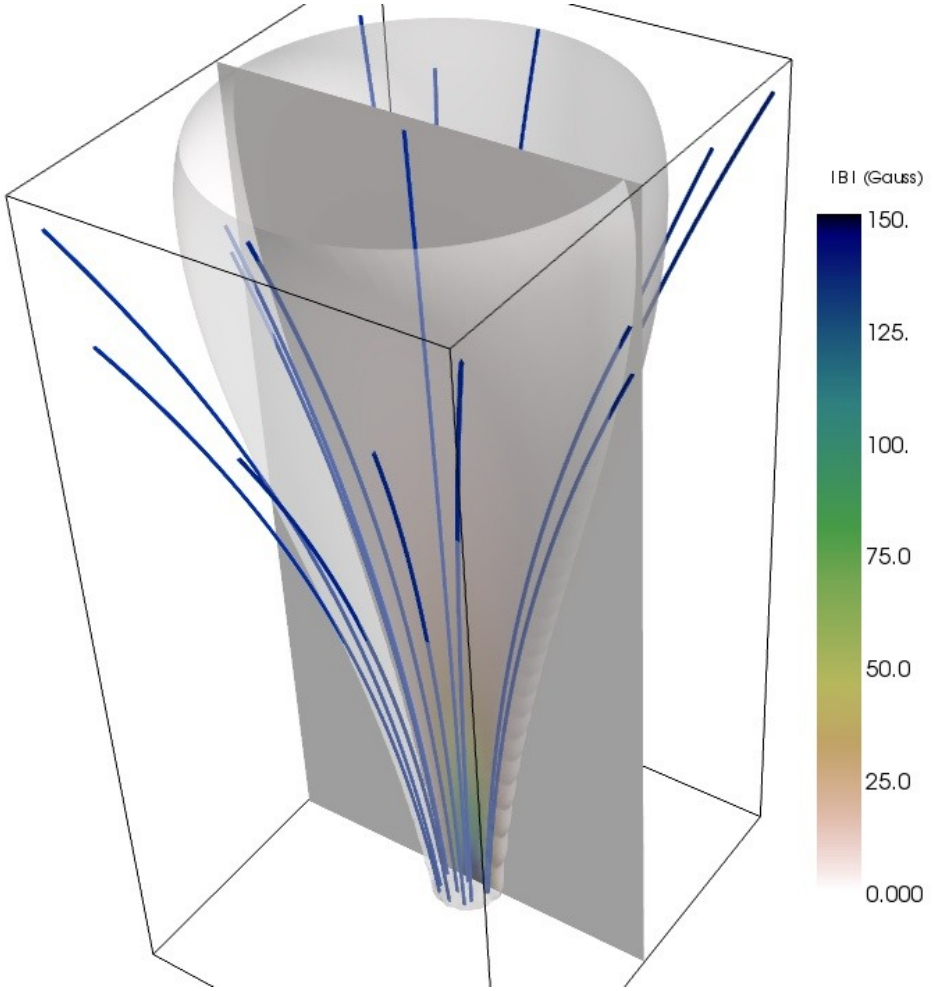

Fig. 3.4 3D rendering of the background magnetic field along with the selected field lines. The isosurface illustrates the expanding intergranular magnetic field with an exponential drop in magnetic field strength with height. A vertical 2D slice of the background magnetic field is shown in the middle which is used to estimate the associated model magnetic field perturbations from an observed spicule's velocity field. Figure adopted from (Sharma et al., 2017).

I, Ca II, He I) and/or instrumentations. Previous reports include studies from e.g., Trujillo Bueno et al. (2005), where using Stokes profile of He I (1083 nm) triplet, they measured field strengths of 10 G. They also pointed out that significantly stronger fields could also be present which was later supported by López Ariste and Casini (2005). Recently, Suarez et al. (2015), reported the magnetic field estimates for spicules with variations in height and inclinations, but like previous studies, these were not been able to provide any conclusive insight. Also, other methods, like, Zeeman splitting and gyroresonant emission didn't proved much effective yet for the turbulent chromospheric environment.

Since the motivation here is to only infer the magnetic pressure changes and not the accurate estimation of chromospheric magnetic fields, we simply used a model

background magnetic field and estimated the perturbations in this assumed magnetic field due to the observed temporal and spatial evolution of the spicule's velocity field. The background magnetic field is modelled to be in pressure balance condition with the surrounding stratified quiet-Sun atmosphere. The magnetic field emerging from the photospheric footpoint undergoes an exponential expansion, till the transition-region heights due to drop in plasma pressure and dominance of magnetic pressure in lower corona (see Fig. 1.3). The 3D model background field (as shown in Fig. 3.4) chosen here is self-similar and the external atmospheric parameters are taken from Vernazza et al. (1981). Conveniently, this class of the magnetic field is given by a simple closed analytical expression. The effects of horizontal inhomogeneity and magnetic tension forces are, however, neglected, though those may have significant effects on the pressure balance. The magnetic field arrangement is such that it purely describes a vertical magnetic field along the axis of the tube with decreasing field strength in height and radius. The complexity of the background magnetic field construction is restricted only to the structure of quiet-Sun conditions in lower solar atmosphere with transition-region gradients, while other factors, such as, axial asymmetry, torsion, plasma inhomogeneity, etc, are avoided. For the full description of methods employed to construct such a field, along with boundary conditions and tests are given by, e.g. Gent et al. (2013); Shelyag et al. (2008). It is known that intergranular magnetic fields are measured to be between 100-200 G for quiet-Sun region (Trujillo Bueno et al., 2005), therefore we choose the foot-point magnetic field to be 150 G.

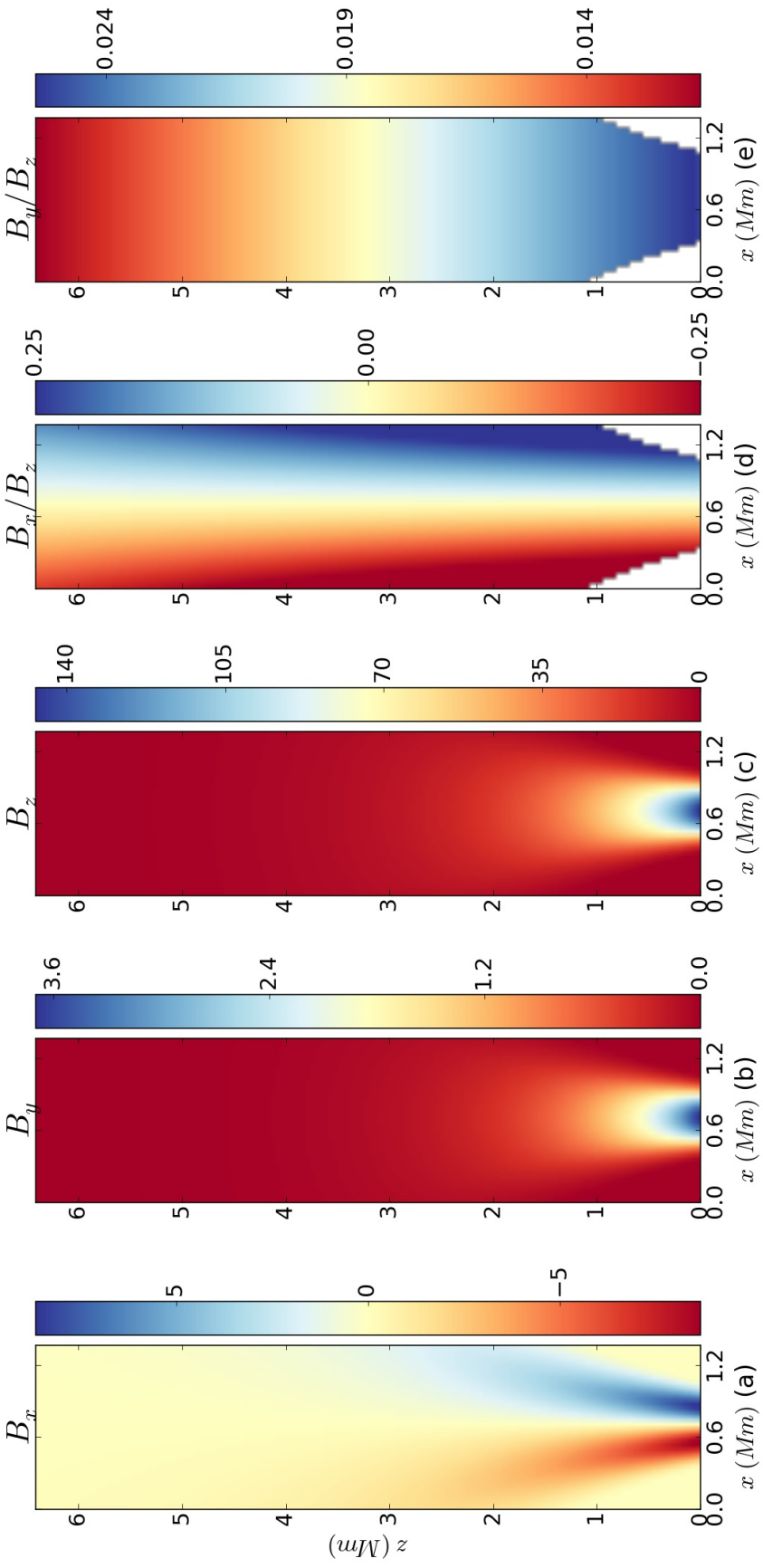

Fig. 3.5 Components of the model background magnetic field used to approximate the magnetic pressure perturbations due to spicule dynamics. Panels (a-c) shows all three components (x,y,z) respectively, of background field (B). The ratios of the model magnetic field components (B_x/B_z and B_y/B_z) are shown in panels d-e.

In order to have an estimate for the perturbations in magnetic pressure for the given background magnetic field , we employ the 3D velocity vector components in the linearized induction equation. The velocity vectors, $\mathbf{v}(x,y,z,t)$, in terms of the tube displacement, $\xi(x,y,z,t)$ can be given as $\mathbf{v} = \delta\xi/\delta t$. The components of the model background magnetic environment ($\mathbf{B}_0$) are shown in Figure 3.5. The induction equation can thus be expressed as

$$\delta\mathbf{b} = \nabla \times (\delta\xi \times \mathbf{B}_0). \tag{3.7}$$

Since, $\delta\xi_n = \xi_n - \xi_{n-1}$ is the change in the displacement of the tube at a given frame number 'n', the perturbed magnetic field, relative to '$n-1$' frame, can be rewritten as

$$\delta\mathbf{b}_n = \nabla \times \left[\left(\xi_n - \xi_{n-1}\right) \times \mathbf{B}_0\right]. \tag{3.8}$$

The LOS component of the perturbed magnetic field is then

$$\begin{aligned}\delta b_{y,n} = &\frac{\delta}{\delta x}(B_{0x}\delta\xi_{y,n} - \delta\xi_{x,n}B_{0y}) - \\ &\frac{\delta}{\delta z}(B_{0y}\delta\xi_{z,n} - \delta\xi_{y,n}B_{0z}).\end{aligned} \tag{3.9}$$

Here, B_0 and $\delta\xi$ with subscripts x,y,z refer to the components of the background magnetic and estimated displacement fields. Equation (3.9) is applied in the Sections 3.3.1 and 3.3.2 for two particular spicules, SP5 & SP8, to model LOS magnetic field perturbations with their observed velocity field dynamics as an input. Physical characteristics of both spicule cases are given in Chapter 2. Spicules SP5 & SP8 are here discussed in detail since they are representative examples that have their transverse motion mostly in the POS or along the LOS.

3.3 Results

From the eight selected spicules, as shown in the previous chapter, about 40 % (SP4, SP5, SP6) had the POS as the dominant plane of the bulk transverse motion[9], while the other 60 % (SP1, SP2, SP3, SP7, SP8) have their transverse motion mainly along the LOS. Velocity-vector maps, along with other derived quantities (SP5, Fig. 3.6: resultant displacement, acceleration and magnetic field perturbations) were constructed

[9]The spicule has motions both parallel and perpendicular to observer's LOS, but here, the dominating plane of motion is considered.

by combining the LOS and POS velocity estimates at every pixel in the 2D image frame. The detailed analysis of spicules SP5 and SP8 are presented in this section for the identification of the confined wave-mode in these structures.

3.3.1 Case 1. Transverse motion dominant in POS

Figure 3.7 shows an intensity image (I) of spicule SP5 observed at -1.032 Å, from the Hα line core position and the difference image (δI), along with the perturbed LOS Doppler velocity (δV_y), magnetic field (δb_y) and acceleration estimates. The selection of this particular line scan position is due to clear observation of the spicule feature for most of its lifetime. Difference image is acquired by subtracting two consecutive intensity images ($I_{n+1} - I_n$), while the perturbed Doppler velocity is obtained by removing the average Doppler velocity of the entire ROI from each pixel. It can be seen that for the observed spicule, the LOS Doppler velocity (Fig. 3.7c) shows Doppler shift red-blue asymmetry across its width which has previously been interpreted as the signature of m = 0 torsional Alfvén waves by De Pontieu et al. (2012). Estimates for acceleration (Figure 3.7d) show LOS magnitudes up to 1 km/s^2 along the spicule. For our chosen background magnetic field the magnitude of the LOS perturbation shown in Figure 3.7e is up to 0.3 G. The magnitude of the perturbed magnetic field when compared to the background field is of the order of $\sim$ 0.01 - 0.13.

The POS displacement of spicule SP5 as a function of time can be seen in Figure 3.8. This indicates that there is a dominant component of the bulk transverse motion in the POS. At the transverse anti-nodes, indicated by the black arrows, it can be seen in Figure 3.8b that the LOS velocity shows the same red-blue asymmetry across the spicule width as shown in Figure 3.7c. The kink wave model shown in Figure 3.12a,b indicates that this asymmetry in Doppler velocity can be attributed to its associated $m = 1$ dipolar velocity field if the LOS is approximately perpendicular to the bulk transverse motion. This is an alternative explanation to the $m = 0$ torsional Alfvén wave interpretation of De Pontieu et al. (2012). Also, note that the Doppler shifts are higher around the boundary of the spicule indicating strong counter-streaming in the external plasma.

Although previous studies interpreted the transverse waves observed in spicules with the Solar Optical Telescope on-board Hinode as being incompressible, Figure 3.8d shows that by substituting the estimated velocity field from both imaging and spectroscopy in Equation 3.9, a perturbed LOS component of the magnetic field is a natural consequence. Taking this as a proxy for magnetic pressure variations along the spicule, this questions the idea that these motions are incompressible. In fact, the kink wave

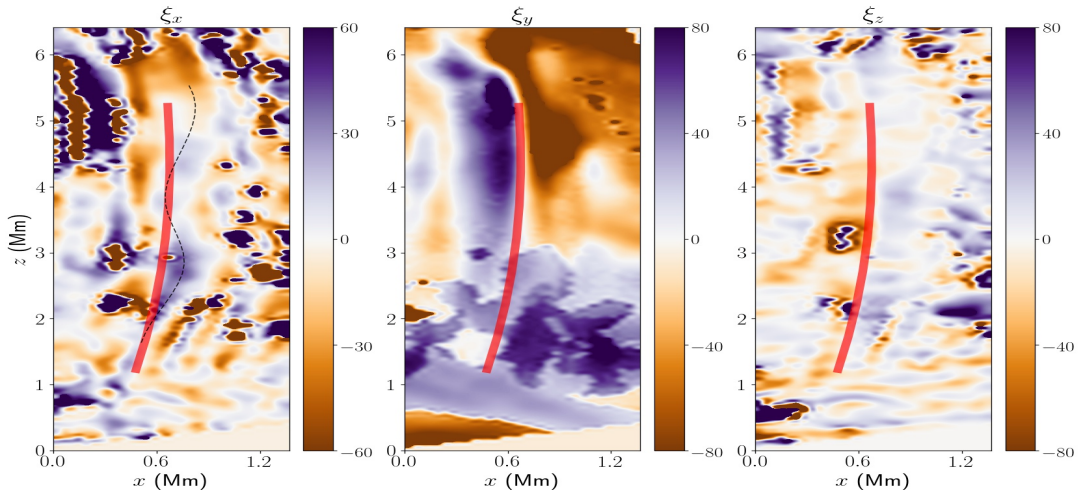

(a) Transverse displacement (ξ) components estimated from imaging (POS) and spectroscopy (LOS) data.

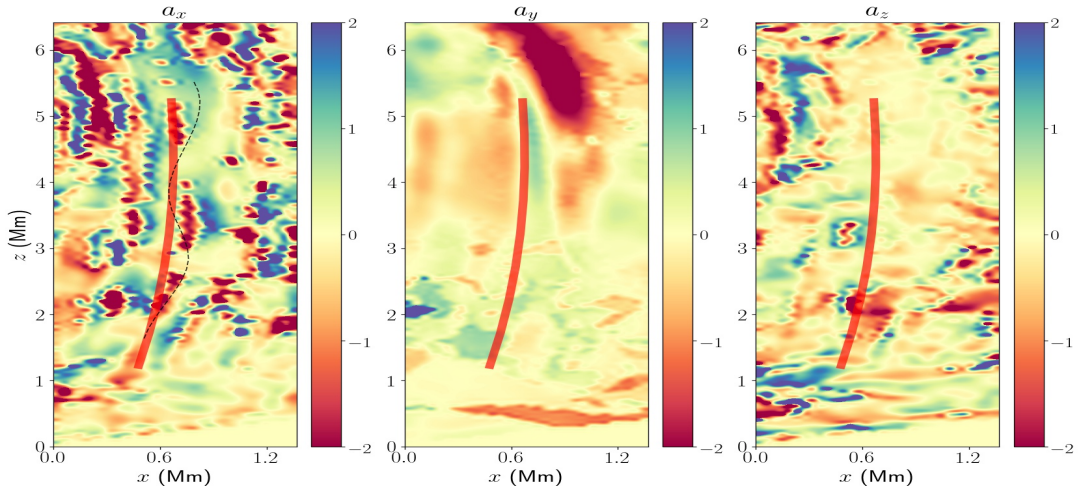

(b) Acceleration parameters (a) at each pixel, used as proxy for plasma pressure perturbations associated with spicule dynamics.

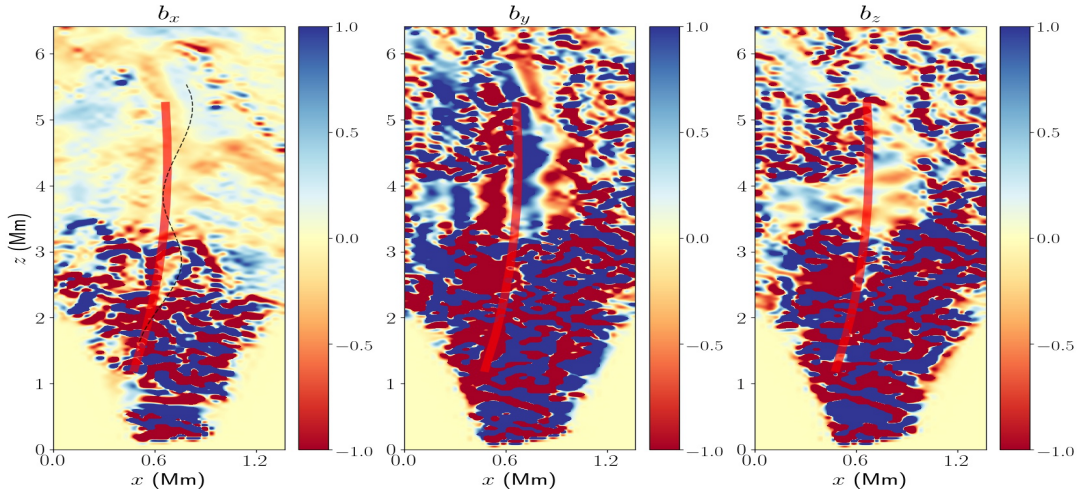

(c) Magnetic pressure perturbation (b) components estimated by substituting 3D velocity vectors in the induction equation.

Fig. 3.6 Components of the estimated [top:] displacement ($\xi_{(x,y,z)}$), [middle:] acceleration ($a_{(x,y,z)}$) and [bottom:] magnetic pressure perturbation ($b_{(x,y,z)}$) parameters for spicule (SP5) at a given time ($t = 46.2$ sec). Red line marks the position of spicule structure from Hα intensity image. Dashed-line marked over x-component (traced by eye) shows the possible kink-behavior in the estimated parameters due to POS motion.

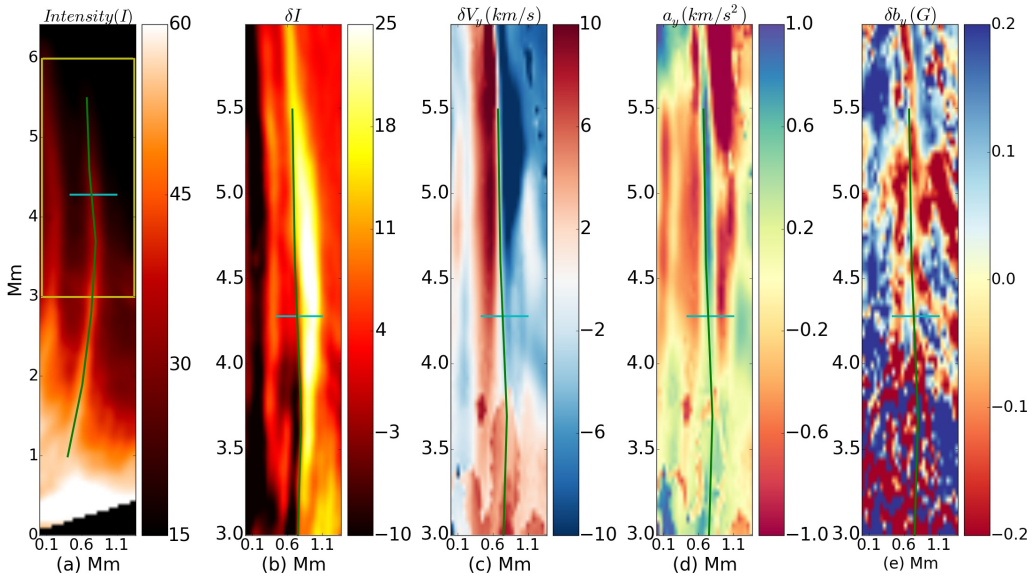

Fig. 3.7 Panels show observed and estimated parameters of spicule SP5 (marked by line). In panel (a), the ROI is highlighted in the Hα intensity image. Panels (b) to (e) show the intensity difference (δI), Doppler velocity (δV_y), acceleration (a_y) and the LOS magnetic field perturbation (δb_y), respectively. The horizontal line marks the location of slit used for time-distance plot shown in Figure 3.8. Analysis of the intensity and Doppler shifts provided POS and LOS velocity and acceleration components while the LOS magnetic field perturbation is used as a proxy for pressure changes in the vicinity of the spicule. Figure adopted from (Sharma et al., 2017).

model in Figure 3.12(a-b) predicts such asymmetric pressure variations across the width of the spicule if the LOS is approximately perpendicular to its bulk transverse motion. There is also supporting evidence of this asymmetry at the positions of the black arrows in Figure 3.8d.

3.3.2 Case 2. Transverse motion dominant along LOS

Figure 3.9 shows a comparison of the observed spicule (SP8) at the line scan position, λ_s = -0.946 from line core, along with other estimated quantities. The slice across the spicule to produce the time-distance plots in Figure 3.10 is shown in Figure 3.9a. It can be seen from the Figures 3.9c and 3.10b that the Doppler velocity is symmetric across the width of the spicule. This is consistent with the kink wave model shown in Figure 3.12(c-d), where the bulk transverse motion is along the direction of the LOS. This interpretation does not permit the appearance of apparent $m = 0$ torsional Alfvén wave and is consistent with what we actually observe.

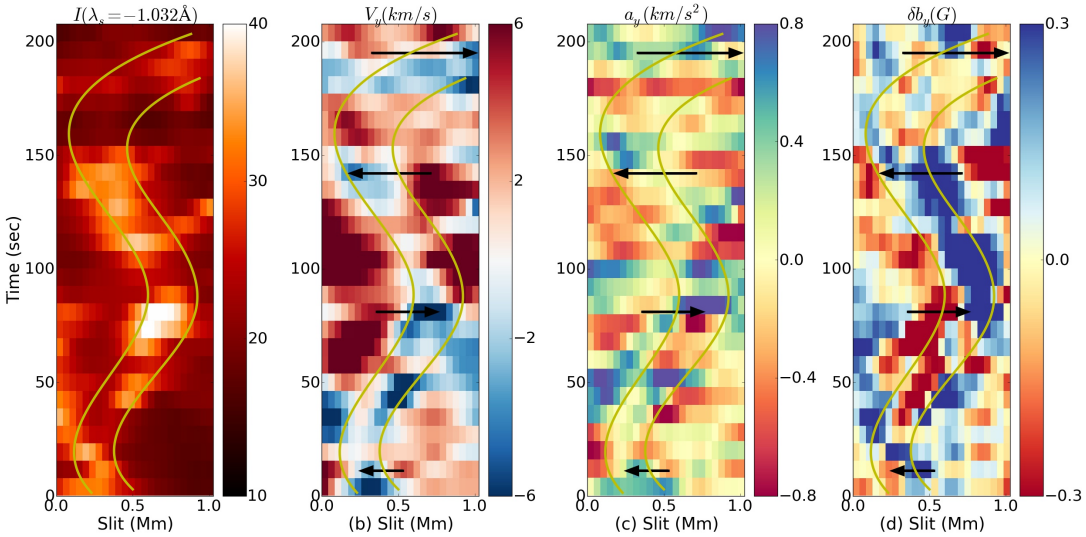

Fig. 3.8 Panels show (a) Hα intensity (I) profile for spicule SP5 with its POS transverse displacement highlighted by yellow lines (traced by eye). In panel (b) the positions of the arrows show that the Doppler velocity has a transverse red/blue asymmetry which alternates with time. The arrows also mark the direction of spicule transverse displacement. In panels (c) and (d), at the arrow locations their is also evidence in transverse asymmetry in both acceleration and the perturbed LOS magnetic field. Figure adopted from (Sharma et al., 2017).

If the LOS is perpendicular to the spicule axis, $m = 0$ motion is independent of the azimuthal viewing angle, however, $m = 1$ motion is not. In ideal conditions, the torsional motion associated with $m = 0$ Alfvén wave is confined in the waveguide (Fig. 3.11) and would not cause any compressions/rarefactions in the ambient atmosphere. This will result in the axisymmetric Doppler signature generated from motions within the structure and will remain unaffected from the observer's position, parallel or perpendicular to the structure. In contrast to this, the Doppler signature for $m = 1$ kink wave would be a sum a rotational motion (due to external displaced plasma) and transverse motion (due to tube displacement). This will strongly depend on the view-angle, and influenced by the direction of dominant bulk transverse motion (see Fig. 3.12). From the data analyzed here, spicules which do not have a notable transverse POS motion do not exhibit the Doppler red-blue asymmetry across their widths which De Pontieu et al. (2012) interpreted as $m = 0$ torsional Alfvén waves. Therefore, this supports the idea that the asymmetric Doppler shift across spicules shown in Figure 3.12c and 3.7b is actually due to $m = 1$ rather than $m = 0$ rotational motion. In such a scenario, the rotational and transverse motions could be coupled (see e.g., Goossens et al., 2014) and this should be the focus of a future study.

The kink wave model of Figure3.12(c-d) suggest that when LOS bulk motion, observed as the Doppler velocity, is dominant for a spicular structure, the associated

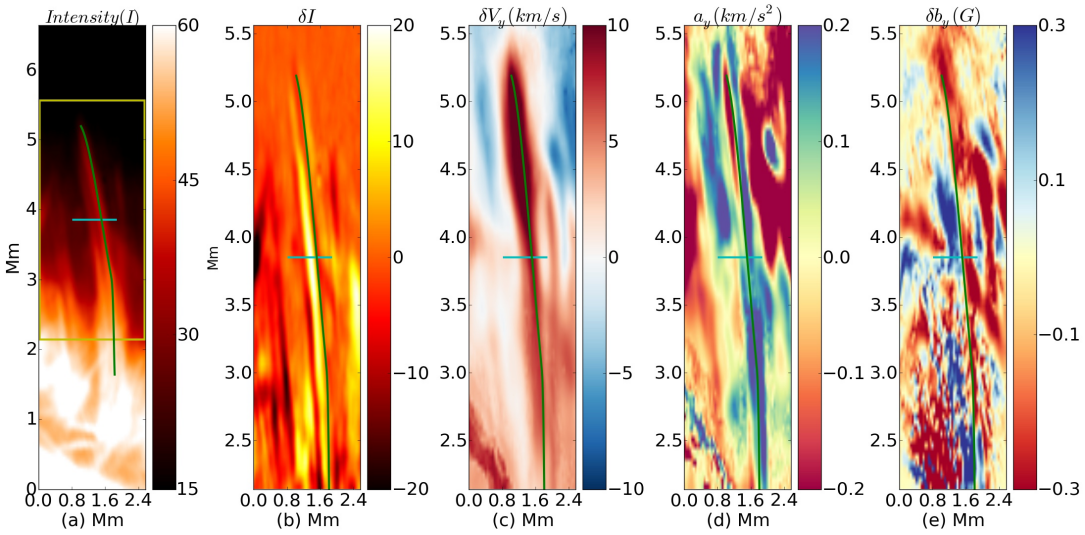

Fig. 3.9 Panels show observed and estimated parameters of spicule SP8 (marked by line). In panel (a), the ROI is highlighted in the Hα intensity image. Panels (b) to (e) show the intensity difference (δI), Doppler velocity (δV_y), acceleration (a_y) and the LOS magnetic field perturbation (δb_y), respectively. The horizontal line marks the location of slit used for time-distance plot shown in Figure 3.10. Figure adopted from (Sharma et al., 2017).

magnetic field component experiences compression or increase in magnitude. However, comparison between Figure 3.10b and d shows a more asymmetric profile for the modeled magnetic perturbation. Since the time-distance plots of Figure 3.10 also show a weaker but still noticeable transverse displacement in the POS, this could be due to external pressure gradients in the spicule's environment, or indeed another kink wave polarized at a different angle. The kink wave model illustrated in Figure 3.12 assumes that there is only one kink wave present and that the spicule is undergoing a "*free oscillation*". Of course, this is highly idealized and the assumption of a quiescent environment may be far from reality. However, in agreement with Case 1 in Section 3.3.1 our modeling suggests that pressure forces in and around spicules play a part in their observed dynamics and that the initial interpretation of incompressible motion by previous studies (De Pontieu et al., 2007d) may have been too simplified.

3.4 Conclusion

I now summarize the key findings of this chapter. Here, the spicule structures, assumed as cylindrical magnetic waveguides are having higher plasma densities when compared to the background atmosphere. Theoretically, these flux tubes can support a superposition of MHD wave-modes with any azimuthal wavenumbers (m). However,

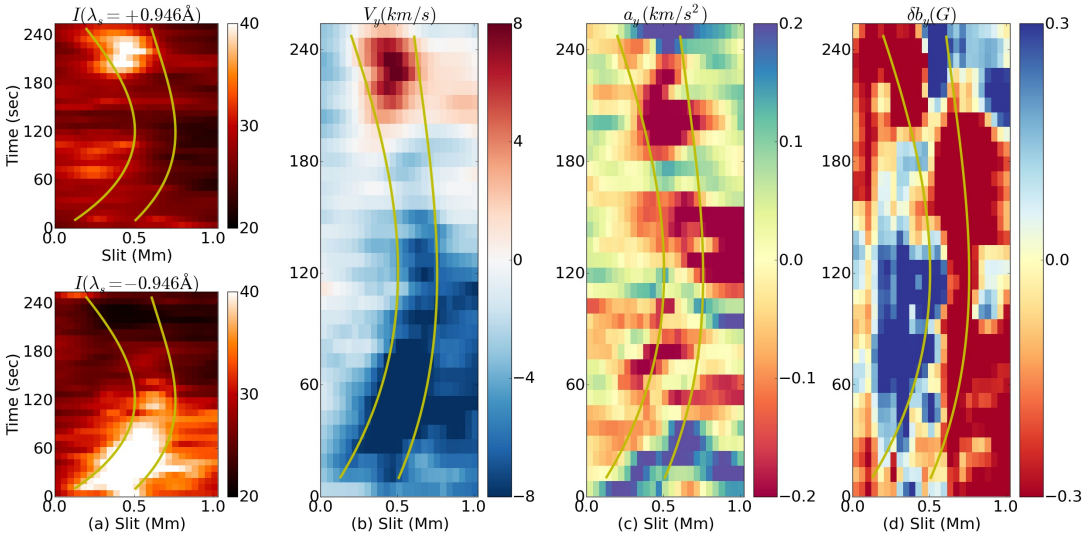

Fig. 3.10 A comparison of time-scale evolution of observed/estimated parameters for spicule SP8. Panel (a) shows Hα intensity (I) profiles at line-scan positions ($\pm\lambda_s$=0.946) and panel (b) shows Doppler shifts providing evidence that the bulk transverse motion of the spicule is along the LOS. Panels (c) and (d) show variations in acceleration (a_y) and the modelled LOS magnetic field perturbations (δb_y) along the spicule. The yellow lines (traced by eye) mark the location of the spicule. Figure adopted from (Sharma et al., 2017).

up until now, only the low-order m modes were observed and reported in the previous studies, as listed in the Introduction section. Since, the observational signatures (spectroscopic/Doppler) for torsional Alfvén wave and kink wave are very similar (see Figs. 3.11 and 3.12(a)), the correct interpretation of the confined wave-mode in spicule structures is highly important to quantify the energy estimates and dissipation mechanisms. Many earlier works, listed in the Introduction section and else, interpreted the red-blue axisymmetry as a conclusive evidence for torsional Alfvén wave, and reported it as such, or under 'Alfvénic' label. This interpretation was questioned by Erdélyi and Fedun (2007), Erdélyi and Taroyan (2008), Van Doorsselaere et al. (2008), and Goossens et al. (2014), in their studies.

The newly developed technique (velocity vector reconstruction and subsequent derivatives) explores the wave-mode identification problem by analyzing the perturbations resulted due to kink wave dynamics. Ideally, when these denser flux tubes move in the chromospheric environment under the influence of kink wave-mode, these should, create perturbations in nearby chromospheric magnetic and velocity fields. These perturbations would be, in general, the displacement of both magnetic and velocity fields, which when observed, can provide clues to distinguish between dynamics if resulting from a kink mode or a torsional mode. The torsional mode

should not displace the magnetic flux tube structure. The observed dynamics would be the intrinsic motion of the tube itself, with a minimal effect on the external plasma.

There could be an argument here that, in case, the tube is swaying in $frozen-in$ condition, with external magnetic and plasma fields, showing the torsional motion, as observed in Doppler estimates as red-blue axisymmetry. In that case, there could not be any relative changes in magnetic and plasma pressures at nodes and anti-nodes of tube motion. The same argument applies in case, the tube is stationary and the chromospheric plasma is turbulent. Still, an observer, would not see any patterns in plasma and magnetic pressures around spicule structure, relative to torsional motion. However, if the tube is oscillating under the influence of kink wave-mode, it will perturb the external plasma and magnetic environment. The external plasma would be displaced, while ambient magnetic fields would experience consequent compression and rarefaction, due to the spicular motion. The displaced surrounding plasma, due to the assumed cylindrical geometry, would certainly have its contribution in observed Doppler velocity estimates, which would further depend on the location of the observer (or Line-of-Sight: LOS), relative to the tube motion.

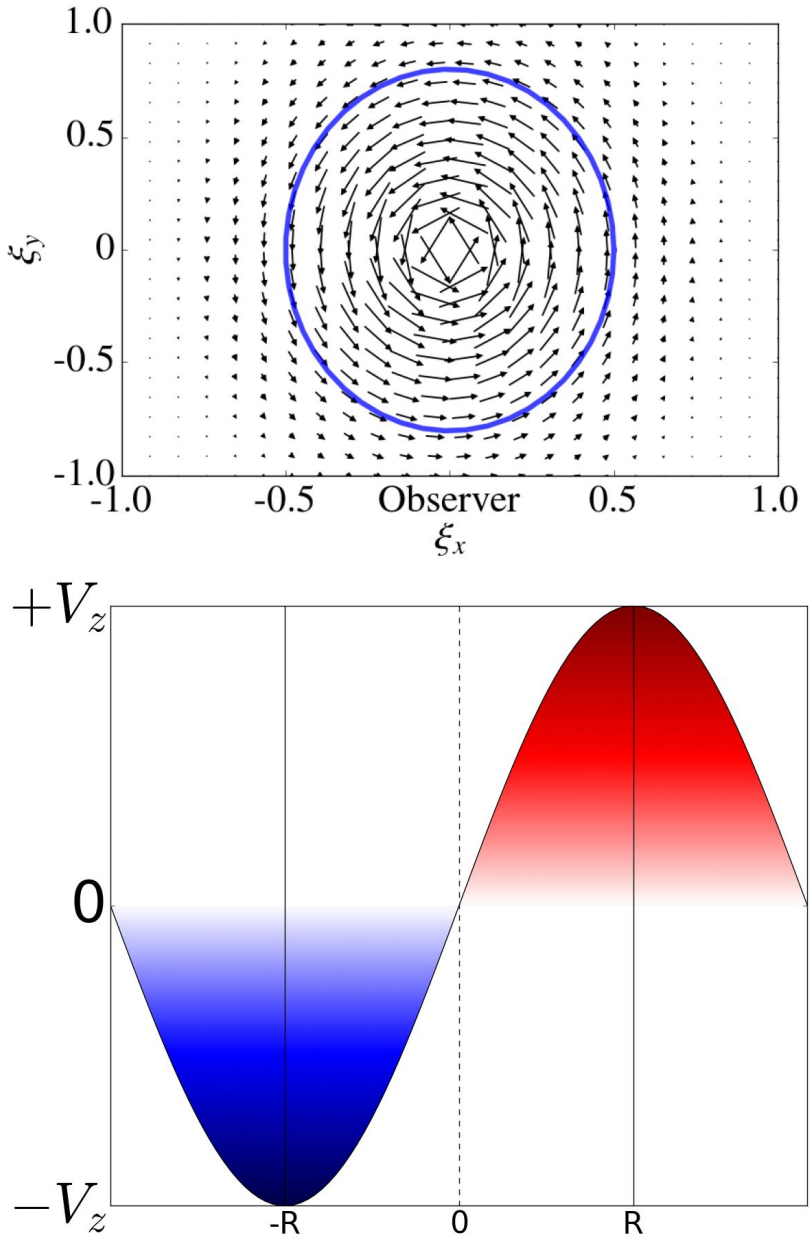

Fig. 3.11 Figure corresponding to a spicule with confined torsional Alfvén wave mode. The top panel show the plasma displacement field (ξ) in the *xy*-plane with the observer's LOS along the *y*-axis. In ideal conditions, the flux tube is not displaced from its axis, however, the plasma motion is restricted within the tube's cross-section, marked here as circle with radius (R). Corresponding profile for LOS Doppler velocity (V_y) is given in panel below, which resembles that from the spicule undergoing kink oscillation.

Fig. 3.12 Figure corresponding to a spicule undergoing linear kink wave motion where the bulk transverse motion is perpendicular [panels (a) and (b)] and parallel [panels (c) and (d)] to the LOS. The plasma is assumed to be optically thick. The top row shows the spicule's displacement field (ξ) in the xy-plane with the observer's LOS along the y-axis. The arrow at the centre of the spicule marks the direction of its motion and the perturbed magnetic pressure color-coded around its boundary. Corresponding profiles for Doppler velocities (V_y) and the perturbed y-component of magnetic field (δb_y) are given in panels below for the spicule with radius (R). Figure adopted from (Sharma et al., 2017).

From the two representative cases, in the first case (SP5), the bulk motion, of the spicule structure is perpendicular to the observer's LOS. In the integrated-intensity images, an observer will see the swaying motion of the waveguide, indicating the presence of a kink-mode instability. Doppler estimates of the same structure would give an axisymmetric red-blue profile, which previously has been interpreted as a conclusive signature for the torsional Alfvén wave by many authors. Here, we further analyzed the plasma (Figure 3.7b,d and 3.8c,d) and magnetic (Figures 3.7e and 3.8d) pressures, to determine whether the observed wave-modes are torsional Alfvén or kink. Difference images, e.g. Figure 3.7b, clearly show enhanced intensity in the direction of spicule motion and same in acceleration (see Figure 3.7d), which could be taken as a proxy for pressure at each pixel, considering mass and area at the pixel as unity. The changes in both magnetic and plasma pressures can also be seen in time-distance plots (Figure 3.8), where the nodes and anti-nodes due to the kink wave, and associated Doppler, acceleration and δb_z perturbations are marked with arrows. The expected profiles for external plasma displacements, Doppler velocities and magnetic pressure perturbations are shown in Figure 3.12a,b.

In the second case (SP8), the bulk velocity is parallel to the observer's LOS, so only the red or blue components, indicating motion towards or away from the observer is seen. In this case, the counter-streaming action of external plasma due to spicule motion won't be visible, but there would be perturbations in plasma (Figures 3.9b,d and 3.10c,d) and magnetic (Figures 3.9e and 3.10d) pressures. The profiles for this scenario are shown in Figure 3.12c,d.

Chapter 4

Dynamical behavior at tube-scale: Nonlinear Kink or Coupled MHD modes[1]

4.1 Background

Bulk transverse oscillations are commonly observed in spicule structures and were identified as the kink wave-mode (De Pontieu et al., 2007d; Ebadi and Ghiassi, 2014; Kukhianidze et al., 2006; Tavabi et al., 2015), in their on-disk counterparts or RBE/RREs (Rouppe van der Voort et al., 2009), in mottles (Kuridze et al., 2012, 2013) and in fibrils (Pietarila et al., 2011). These motions had previously been reported, both on-disk and at solar limb, with periodic structural distortions of the flux tubes, observed as cross-sectional width and associated photometric variations. Longitudinal (field-aligned) motions associated with mass flows and a mix of propagating (upward/downward) and standing transverse waves along the spicule structures were also reported, and are listed in the Introduction chapter. All these motions, along with rotational motions, were routinely observed/interpreted and were reported as independent magnetohydrodynamical (MHD) wave-modes (kink, sausage and Alfvén).

Presence of concurrent independent wave-modes in localized magnetic flux tubes (MFTs) were also claimed in a few studies. Transverse oscillations along with cross-sectional width variations interpreted as kink and sausage MHD wave-modes in spicule structures were reported by Jess et al. (2012). Morton et al. (2012a), also found ubiquitous signatures of transverse, cross-sectional width and intensity oscillations in

[1]This chapter is based on **Sharma, R.**, Verth, G and Erdélyi, R., 2018, "Evolution of complex 3D - motions in spicules", *The Astrophysical Journal*, **853**, 1.

on-disk fibril structures. They postulated that these independently excited wave-modes at MFT foot-point can undergo mode-coupling and can also exchange energies through mode-conversion mechanism at $\beta = 1$ layer in solar transition region. Morton et al. (2012a) claimed that simultaneous nonlinear kink and sausage waves were present in chromospheric MFT structures. Sharma et al. (2017) showed that the rotational motions in spicules appeared either axisymmetric or non-axisymmetric depending on the line-of-sight with respect to the bulk transverse motion. Cross-sectional and intensity oscillations in on-disk slender Ca II-H fibrils (SCFs) were recently reported by Gafeira et al. (2017a) and interpreted as sausage mode waves.

In the linear regime, the cross-sectional width and associated photometric variations are signatures for both $m = 0$ sausage and $m \geq 2$ fluting modes in MFT structures. Beyond the small amplitude regime, the nonlinear kink mode can also distort the cross-sectional width/shape and induce stronger density/intensity variations, resulting in accelerated wave damping due to coupling to higher order fluting modes (Ruderman et al., 2010; Ziegler and Ulmschneider, 1997a,b). Recent numerical simulations (Magyar and Van Doorsselaere, 2016) have shown for coronal loop structures that nonlinear kink oscillations are coupled to the $m = 2$ fluting mode, and cause the cross-sectional width and intensity fluctuations, with half the period of the kink mode. All these factors can result in ambiguity in the identification of MHD wave-modes in the Sun's atmosphere.

This chapter explores the complex and coupled evolution of plasma 3D motions in spicules by examining the phase-relationships between the resultant tube displacement (ξ_r), cross-sectional width (W'), intensity (I), and azimuthal shear/torsion (ξ_t) components in spatial and temporal domains. The different dynamical components, which were earlier reported as independent MHD wave-modes, could in fact be the nonlinear properties of the confined kink wave-mode, which is responsible for the overall displacement of the spicule structure. However, these could also be understood in linear MHD domain as discrete wave-modes, but under certain assumptions regarding twist, irregular geometry and/or fine-tuning of the driver at the flux tube footpoint.

4.2 Methods

The estimation of the different dynamical components (longitudinal, transverse, cross-sectional width, azimuthal shear/torsion) associated with the spicule motion are discussed in this section. According to the Nyquist criterion, the pixel (cadence) resolution of the Hα data used in the study, allowed us to detect any MHD waves confined in

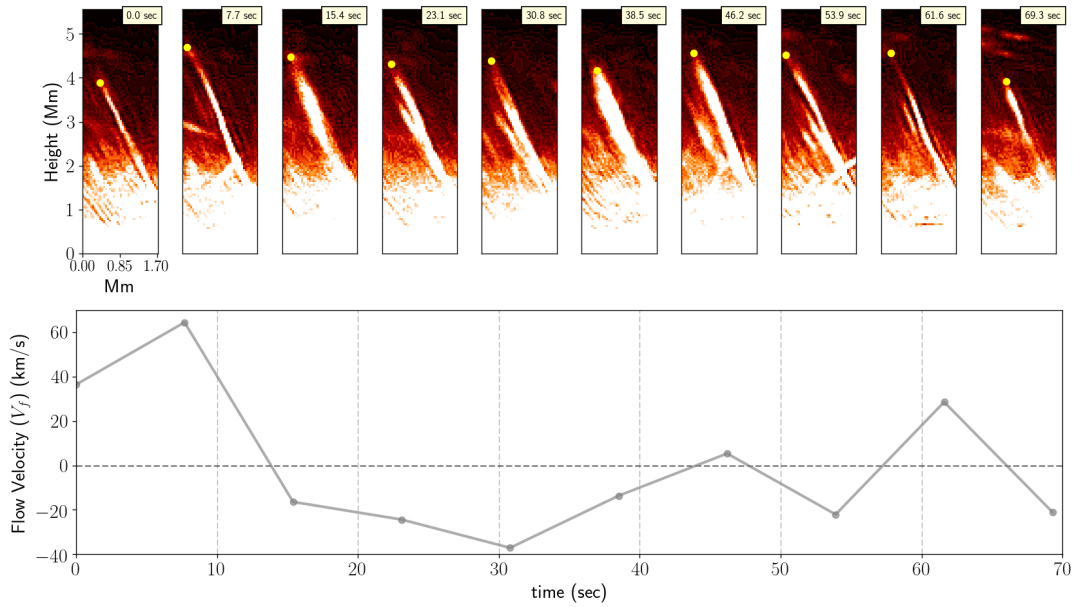

Fig. 4.1 Top panel shows the temporal evolution of the spicule (SP1) structure at -1.204 Å, from the Hα line core, with the apex marked with a yellow dot in the unsharp-masked (USM) images. The longitudinal motion of the marked position is used as a measure of field-aligned flows (V_f) along the spicular waveguide, shown in the lower panel.

the spicular waveguide with wavelength greater than 86 km (15.4 sec), though, the angular-resolution restricts any observed wave behavior below ∼100 km to be unrealistic. The least-superimposed spicule structures outlined as high intensity features were studied, with a case study (SP1), presented here for detailed analysis and is shown in the Figure 4.1.

4.2.1 Longitudinal (field-aligned) motions

Longitudinal or field-aligned motions associated with the mass upflows and downflows were analyzed by tracking the visible apex of the spicule (SP1) structure in intensity images. The underlying assumption is that the apparent changes in the apex location of the spicule structure, at each time frame, is solely due to the plasma motion, and not due to any thermal or seeing effects. The apex of the inclined spicule structure is visually enhanced with respect to the background emission by the use of an unsharp-mask (USM) procedure[3] for correct estimation of the height. The temporal evolution of the spicule apex (marked as yellow dot) is shown in Figure 4.1.

[3]https://docs.scipy.org/doc/scipy-0.13.0/reference/generated/scipy.misc.imfilter.html

4.2.2 Transverse displacement

Transverse motions as observed in the plane-of-sky (POS) and the line-of-sight (LOS) domains by imaging-spectroscopy were used to estimate the resultant motion of the spicular structure. These perpendicular displacement components were measured using the time-distance (TD) diagrams, generated by applying the cross-cuts on intensity (for POS) and Doppler (for LOS) images. The intensity images at Hα line-profile wing positions were used to estimate the POS displacement (ξ_p). The spicular feature was further enhanced with respect to the background emission by the use of an USM procedure[4]. Perpendicular to the spicule axis, cross-cuts were placed at every fourth pixel ($\sim$172 km apart) in height. Similar cross-cuts were also made for the original (non-unsharp masked) images for error estimation. The oscillatory axis of the spicule structure in the resulting TD diagrams was located as the nearest pixel with the maximum intensity magnitude at each time-step.

The estimated LOS Doppler velocity (V_y'), using a double-Gaussian function, required correction due to the inclination of the observed structure. Since, the observed structure is inclined to an angle ($\psi = 23.6^\circ$) with the normal, there will be certain contribution from the vertical flow component to the estimated Doppler velocity. This relationship between vertical flow velocity (V_f), estimated from the longitudinal displacement of the apex position between the two consecutive images (Fig.4.1), and the apparent LOS velocity was given by Athay and Bessey (1964). According to them, the apparent LOS velocity ($\bar{V_y}$) component from the flow velocities can be given as

$$\bar{V_y} = \frac{2}{\pi} V_f \ \sin\psi. \tag{4.1}$$

This contribution from these vertical flows to the Doppler velocity measurements is then removed for accurate LOS transverse estimates. The corrected LOS velocity component (V_y), for each time step is given as, $V_y = V_y' - \bar{V_y}$. The displacement in the LOS direction is then, $\xi_l = V_y \cdot \delta t$, where δt is the time cadence. The resultant displacement (ξ_r) is further given as $\xi_r = \sqrt{\xi_p^2 + \xi_l^2}$.

4.2.3 Cross-sectional width and intensity fluctuations

The width of the spicule structure was estimated by fitting a Gaussian function with a linear background to the cross-sectional intensity profile (Fig. 4.2a,b). The linear background term in the function incorporates the contribution from the ambient plasma

[4]https://docs.scipy.org/doc/scipy-0.13.0/reference/generated/scipy.misc.imfilter.html

and the geometrical effects of the structure on the radiated optically thick emission. These estimates over the height excluded the regions near the foot-points and at the diffuse apex (Fig. 4.2d) of the spicular feature because of flattened/non-Gaussian intensity profiles. Contribution from the background intensity flux near the spicule foot-point and/or from weak contrast in spicule and background intensities at apex can result in a nearly-flat intensity profile which can led to the erroneous estimation of the Gaussian width, and hence was not taken into account.

The Gaussian function fitted to the cross-sectional intensity profile $I(x)$ at each height of the spicular structure is given by

$$I_{fit}(x) = a \exp\left\{\frac{(x-\mu)^2}{2\sigma^2}\right\} + b. \tag{4.2}$$

Here, $I(x)$ is the intensity profile across the MFT structure, 'a' is the peak flux, 'μ' is the central position of the Gaussian-fit, 'σ' is the Gaussian width while 'b' is the linear background contribution. The cross-sectional width (W') of the spicular structure is approximated as the Full-Width Half-Maximum (FWHM) of the Gaussian-fit and is given as $2\sigma\ (2ln2)^{1/2}$. The mean magnitude of the estimated FWHM for all heights is considered as the unperturbed width (W) of the spicular waveguide. Averaged intensity magnitudes at ± 1 pixel to central position (μ) of the Gaussian-fit is taken for the photometric analysis.

4.2.4 Azimuthal shear/torsion

Torsional motion in spicular structures were reported before by De Pontieu et al. (2012), where they used the relative tilt in the horizontal wavelength directions in the observed spectrograms to measure the magnitude of azimuthal shear/torsion (ξ_t). Here, the gradient in the Doppler velocities (V_y), at the unperturbed width (W) of the spicular waveguide is used to estimate the angular displacement or azimuthal shear/torsion. In the presence of any shear forces, the magnitude of the Doppler velocities at the two ends would be unequal, with one edge leading the other. Figure 4.2b, shows that the net velocity ($V_2 - V_1$), between the two edges of W, provide the displacement (AB) at the leading edge of the spicular cross-section. For the given radius (OA) of the unperturbed cross-section, the shear-angle (θ) at the tube center, is given by

$$\theta = tan^{-1}\left(\frac{AB}{OA}\right). \tag{4.3}$$

The angular displacement (AB') is then taken as $\xi_t = AB' = \theta \cdot OA$. The temporal evolution of the perturbed azimuthal shear/torsion ($\delta\xi_t = \xi_t - \bar{\xi}_t$, where $\bar{\xi}_t$ is the mean magnitude of azimuthal shear/torsion parameter at any height) is given in Figure 4.3e.

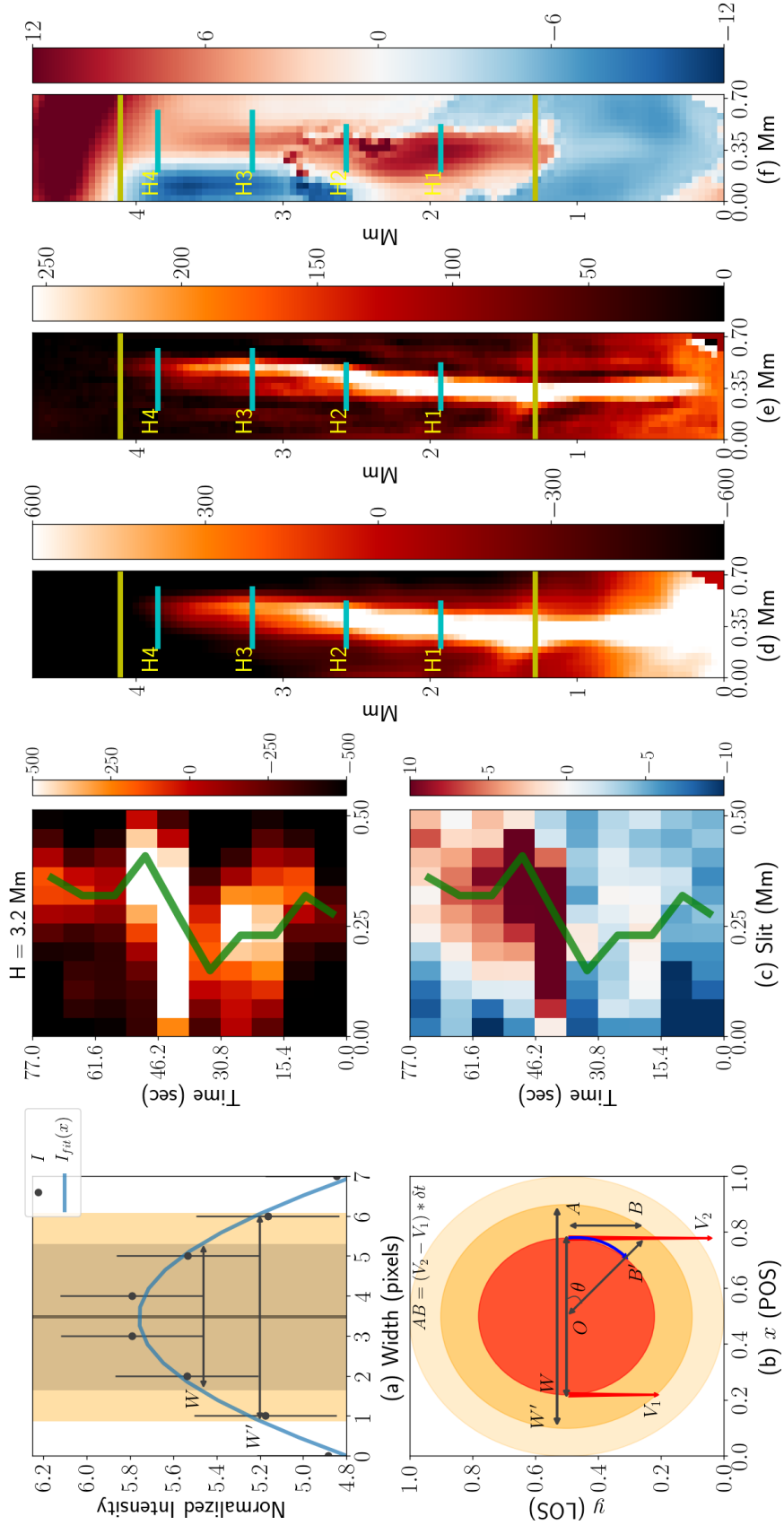

Fig. 4.2 Panel (a) shows an example of the Gaussian-fit ($I_{fit}(x)$) to the normalized intensity, along with $\pm\sigma$ error-bars, across the width for the spicule (SP1). The FWHM of the Gaussian-fit is taken as the measured width (W'), peak (marked as a vertical line) as the center of the spicular waveguide, and the averaged FWHM is highlighted as the unperturbed width (W). Bottom panel (b) showcase the measured width (perturbed and unperturbed) with y-axis directing towards the observer's LOS, while the x-axis marks the POS of the observations. LOS velocities (V_1, V_2), at edges of unperturbed width were used to measure the azimuthal shear/torsion ($\delta\xi$). Top and bottom panels in (c) show sample time-distance (TD) plots at H = 3.2 Mm for intensity (top) and Doppler estimates (bottom). Pixels tracing the structure are highlighted by a line-overplot (green line). Consecutive panels (d-e) show the spicule structure in Hα intensity, unsharp-masked and Doppler velocity (V_y', km/s) respectively. Transverse, cross-sectional width and intensity oscillations are studied for region marked in between the yellow lines, with four sample cross-cuts (H1, H2, H3 and H4) marked to highlight the variations in the estimated parameters at different heights over time.

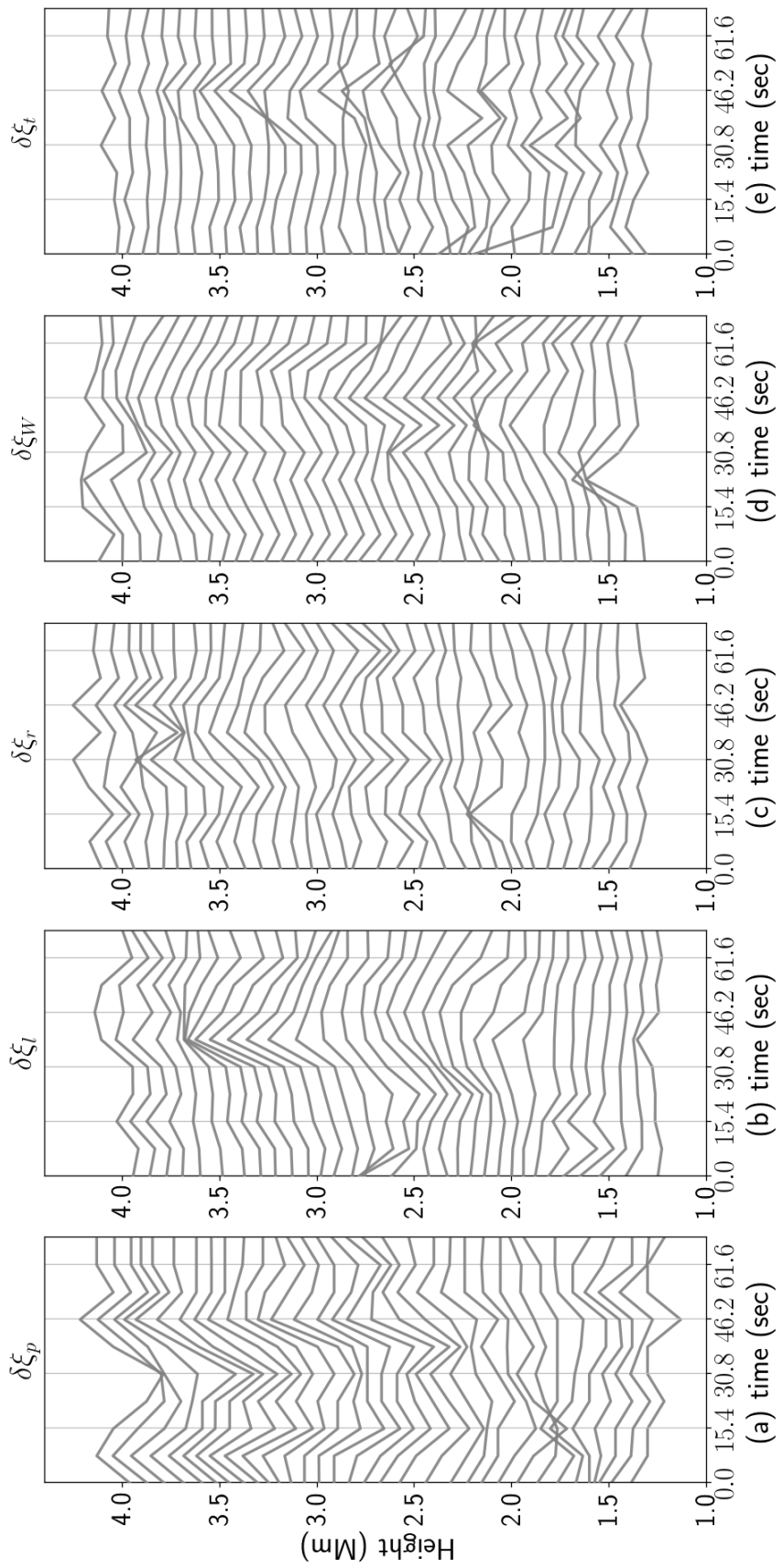

Fig. 4.3 Evolution of the time-distance (TD) behavior for the spicule structure with height, sampled at every four pixels (∼172 km) apart. Panel (a-c) shows transverse components estimated in POS (a: $\delta\xi_p$), LOS (b: $\delta\xi_l$) and the resultant (c: $\delta\xi_r$). Panel (d) plots the variations in cross-sectional width estimates ($\delta\xi_W$), while the azimuthal shear/torsion ($\delta\xi_t$) components are shown in panel (e). The magnitude of the parameters shown here is in 'km'.

4.2.5 Multitaper Spectral Analysis and phase-relationships

To analyze the phase-relationships between the oscillatory behavior of the spicular structure with the cross-sectional and photometric variations, we used the Multitaper Spectral Analysis (MSA) method (Percival and Walden, 1993; Thomson, 1982). This method overcomes the problems (like inefficiency and spectral leakage) posed by discrete Fourier transform (DFT) methods for small data samples. Other techniques available for nonlinear analysis, like, Empirical Mode Decomposition (EMD) and Recurrence Quantification Analysis (RQA), were not employed due to small sample (temporal) size. For datasets with relatively small sample-size, estimating the amplitude and phase between corresponding component frequency (spatial or temporal) could suffer from the inefficient statistical approximation of the parameters. Though, this problem could be tackled by the use of a sliding window (single-taper) with the assumption that the input signal is stationary, nevertheless it can further lead to spectral leakage and contribute to the erroneous estimation of the amplitude and phase angle. A possible solution to the above is the use of 'multitaper' functions. A number of tapers are applied to the data sample and power spectrum is estimated for each of those tapers. The resulting averaged spectrum provides the best estimate of any low-amplitude harmonic oscillations in a relatively short sample size with a high degree of statistical significance. This technique has previously been tested (Komm et al., 1998) and used for the solar data analysis in a variety of spatial and temporal scales (Kilcik et al., 2010; Mufti and Shah, 2011; Prestes et al., 2006) etc.

The method used in this analysis is adapted from van Hoek et al. (2016). Here, in our case, the spectrum ($\hat{g}$) is estimated in the wavenumber (k_z) and frequency (f) domains by taking Q tapers to obtain a set of Q eigenspectra including 'q' eigencomponents using the observed parameters (i and j) with N data points and a constant sampling interval, so that $u = 1, 2, 3, \ldots N$. For a given domain (F) in the spatial (k_z) or temporal (f) regimes, the set of eigenspectra of i is defined as

$$\hat{g}_{ii}^{q}(F) = \left| \sum_{i=1}^{N} i(u) o_q(u) e^{(-Fu)} \right|^2 , \tag{4.4}$$

where, $o_q(u)$ is the data taper for the q^{th} eigencomponent and e^{-Fu} is the Fourier transform. The set of data tapers have the shape of Slepian sequences (Slepian, 1978) and provide a good protection against leakage. The final multitaper ($\hat{g}^{MT}$) is estimated by taking the mean as

$$\hat{g}_{ii}^{MT}(F) = \frac{1}{Q} \sum_{q=1}^{Q} \hat{g}_{ii}^{q}(F). \tag{4.5}$$

The cross-spectral density (CSD) provides an estimate of the strength of the coupling between the observed parameters and further the evolution in wavenumber domain. This is computed using the real valued power-spectral density (PSD) estimate for 'i' defined as $\hat{g}_{ii}^{MT}(F)$ and the complex conjugate of the PSD estimate of j defined as $\hat{g}_{jj}^{*MT}(F)$ and given as

$$\hat{g}_{ij}^{MT}(F) = \frac{1}{N}\sum_{n=1}^{N} \hat{g}_{ii}^{MT}(F)\hat{g}_{jj}^{*MT}(F). \tag{4.6}$$

The phase-angle estimate ($\varphi(F)$) gives an approximation of the relative perturbations between the observed parameters and with that from ambient atmosphere. The estimate is bounded between $\pm\pi$ and is the phase difference at each wavenumber bin between i and j. It is calculated from the imaginary and the real part of the CSD

$$\varphi(F) = tan^{-1}\left[\frac{\text{img } \hat{g}_{ij}^{MT}(F)}{\text{real } \hat{g}_{ij}^{MT}(F)}\right], \tag{4.7}$$

where, img$\hat{g}_{ij}^{MT}(F)$ is the imaginary part while real$\hat{g}_{ij}^{MT}(F)$ is the real part of the estimated CSD. The estimated CSD and mutual phase angles for observed parameters are shown in Figures 4.5 and 4.6. The CSD evolution for wavenumber (k_z) and frequency (f) bins are shown for transverse displacement ($\delta\xi_r$), cross-sectional width ($\delta\xi_W$), and intensity (δI) variations for the observed spicule structure.

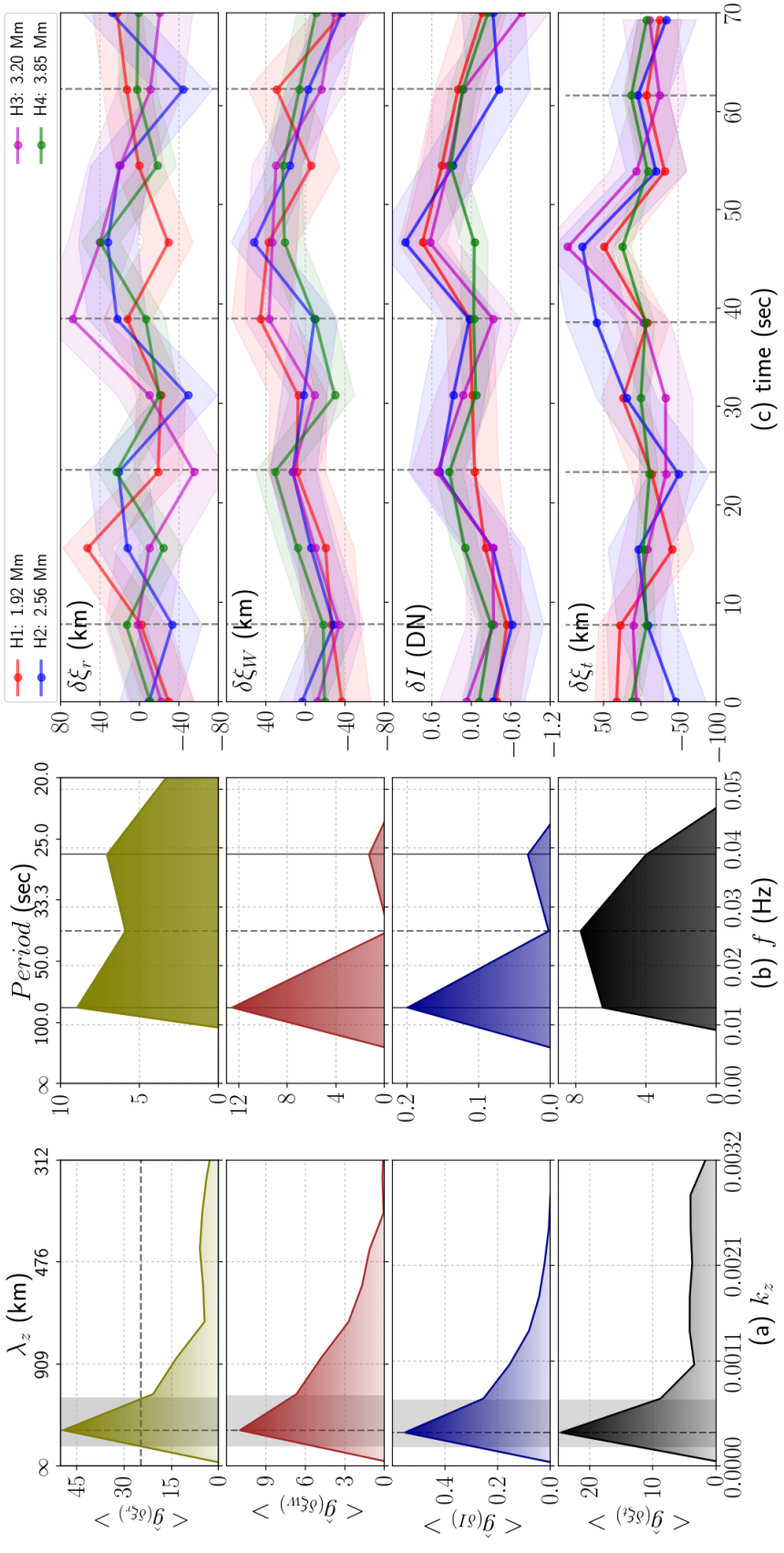

Fig. 4.4 Here, the spectral and temporal variations in transverse displacement ($\delta\xi_r$), cross-sectional width ($\delta\xi_W$), intensity (δI) and azimuthal shear/torsion ($\delta\xi_t$) parameters are shown. Panel (a) shows the temporally averaged spectral profiles (top to bottom: displacement, width, intensity, azimuthal shear), in wavenumber (k_z) domain, with the mean power (taken as background noise) removed. Shaded-region highlights the half-max (horizontal dashed-line) width of the distribution of the peak spectral power (vertical dashed-line). Panel (b) shows similar analysis in frequency (f) domain with primary and secondary peaks in resultant displacement, cross-sectional width and intensity marked with solid lines at 0.013 Hz (77 sec) and 0.039 Hz (25.6 sec). The peak in azimuthal shear/torsion is marked at 0.026 Hz (38.4 sec) with a dashed-line. Panels (c) show the time evolution of the parameters for the heights (H1, H2, H3, H4) marked in Figure 4.2. Examples of in-phase and out-of-phase oscillations are marked with vertical dashed-lines.

4.3 Results

The case (SP1), analyzed here in detail, had a length of 4.1 Mm with the apex-height reaching up to 4.9 Mm from the visible limb at an inclination of 23.6° from the normal. The temporal evolution in imaging showed nearly constant inclination of the structure, with apex (marked in Fig.4.1) undergoing periodic variations along the inclined length. The average longitudinal flow velocity (V_f) is about 41±28 km/s, which is consistent with the previous reports for MFT waveguides (De Pontieu et al., 2007c; Pereira et al., 2012; Sekse et al., 2013b). From the analysis of the 3D velocity components, as discussed in the previous chapter (Chapter 3), the concurrent rotational and transverse motions in spicules were most consistent with the kink-mode, confined in the analyzed spicular waveguides.

The temporal evolution of the transverse motion of the spicule structure at different heights were studied by TD diagrams, generated by the procedures described in Section 2.2. A visual inspection of a sample TD plot in the imaging-spectroscopy (Fig.4.2c) at 3.2 Mm, shows the bulk transverse displacement of the spicule with the observed wave period comparable to the feature's visible lifetime at the line-scan position (±1.204 Å, from the Hα line core). This gives an impression of the presence of a single *pulse* being responsible for the translation of the structure, with maximum transverse displacement of 180±70 km from its mean axis. This *pulse-like* behavior, in other similar features, was also evident (Fig. 4.7) from the past statistical studies (De Pontieu et al., 2007c; Okamoto and De Pontieu, 2011), where the observed lifetimes coincided with the wave-periods estimated from TD cross-cuts. Recently, Martinez-Sykora et al. (2017) modeled the spicule-like events and attributed the role of an impulsive release of the magnetic tension (*whiplash*-effect), responsible for the observed behavior of spicular structures. Similar explanation for the observed behavior was forwarded by Kuźma et al. (2017), which favored the role of the confined velocity-pulse for the dynamics of the spicule structures. TD plots at every second pixel, over height, in imaging and spectroscopic observations (Fig.4.3a,b), respectively, were used to study the evolution of the spicule dynamics in time and to generate the resultant displacement profiles (Fig.4.3c) which reflect the true motion of the waveguide. Here, it should be noted that previous studies (Jess et al., 2012; Morton et al., 2012a) only considered the MFT motion confined in a particular plane, whereas, the transverse spicular dynamics is the resultant of the observed motion in the perpendicular planes (POS & LOS).

The perturbed resultant displacement ($\delta\xi_r$) along with the cross-sectional width ($\delta\xi_W = W' - W$, Fig.4.3d), intensity (δI) and azimuthal shear/torsion ($\delta\xi_t$, Fig.4.3e), with average magnitude of 44±39 km, variations were examined in both spatial and

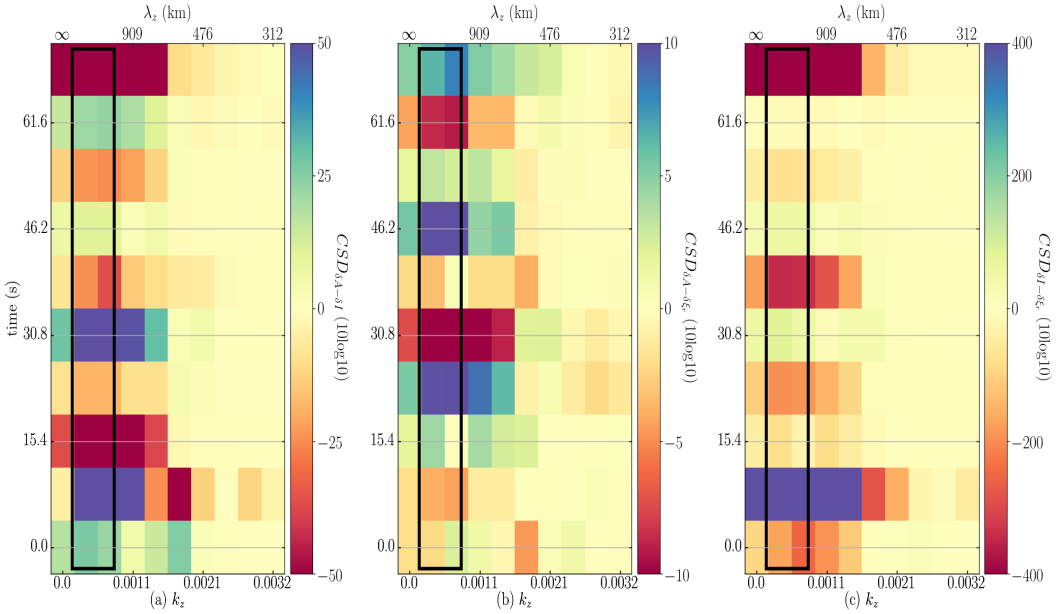

(a) Estimated Cross-Spectral Density in wavenumber (spatial) domain over time. Peak spectral power distribution-width (Fig. 4.4(a)) is highlighted with a black box.

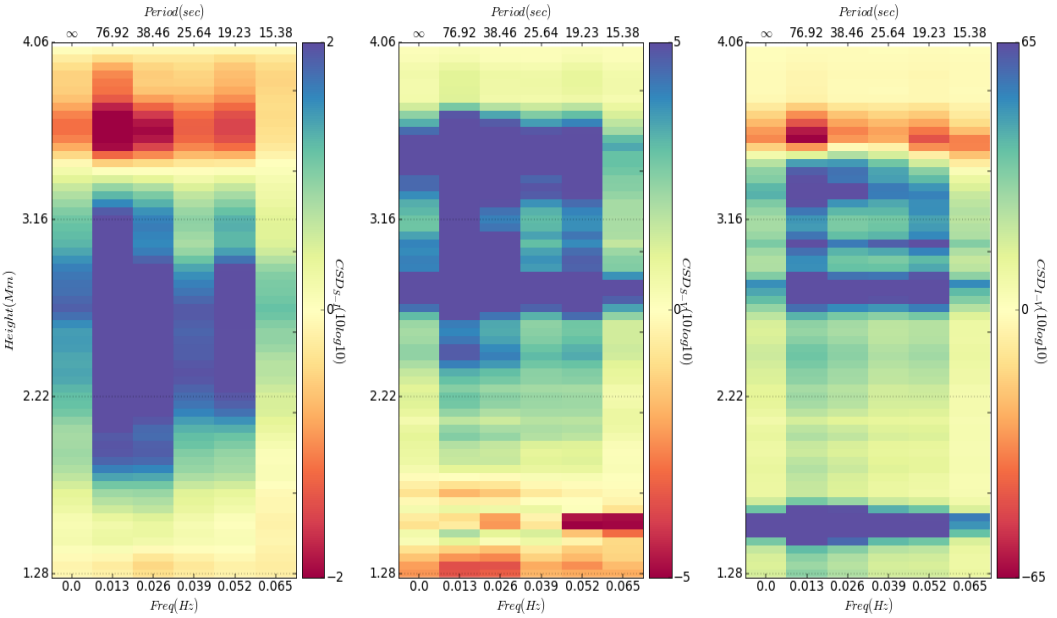

(b) Cross-Spectral Density in frequency (temporal) domain over height.

Fig. 4.5 Sample plots showing the spectral distribution of the estimated cross-power between the resultant transverse displacement ($\delta\xi_r$), cross-sectional width (δW) and the intensity (δI) parameters with time/height and concentration of their mutual energies for wavenumber (top: k_z) and frequency (bottom: f) bins. Panels (a, b, c) show Cross-Spectral Density (CSD) for cross-sectional area - intensity, cross-sectional area - displacement and intensity - displacement estimates, in the respective plots.

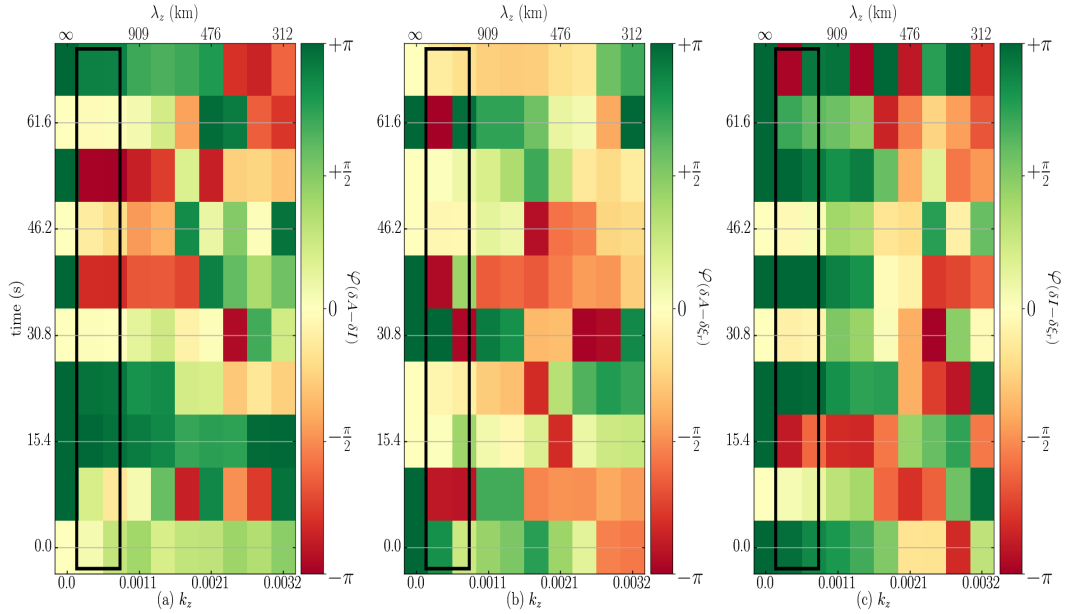

(a) Estimated phase-angle in wavenumber (spatial) domain over time. Peak spectral power distribution-width from Figure 4.4(a) is highlighted with a black box.

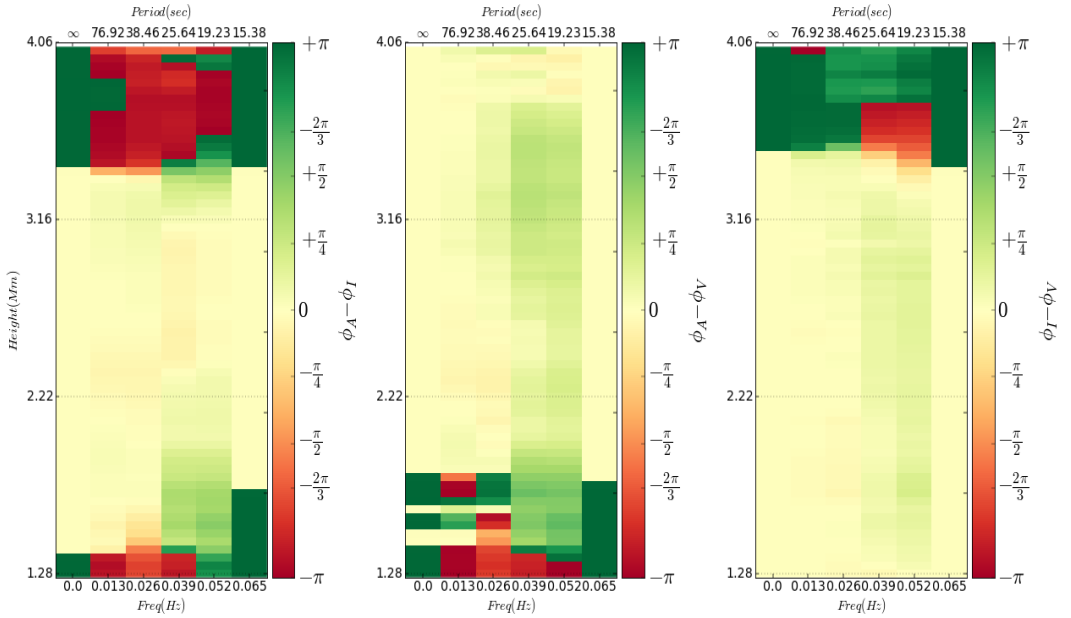

(b) Phase-angle distribution in frequency (temporal) domain over height.

Fig. 4.6 Spectral distribution of phase-angle (φ) between resultant transverse displacement ($\delta\xi_r$), cross-sectional width (δW) and intensity (δI) parameters with time/height for wavenumber (k_z) and frequency (bottom: f) bins. The distribution in both the respective domains is bounded in $\pm\pi^\circ$ range.

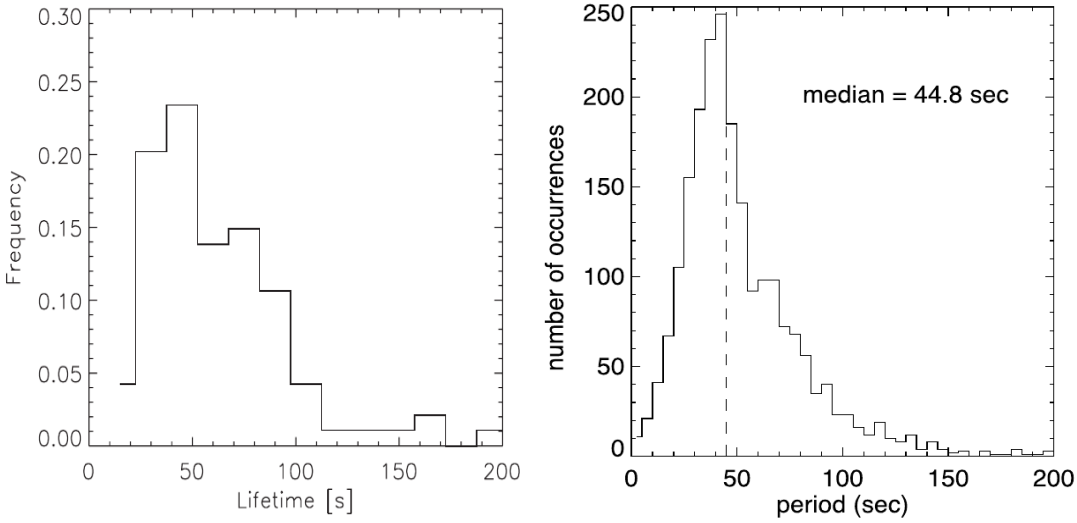

Fig. 4.7 Panels showing comparison between the observed lifetimes and wave-periods for spicules analyzed from Ca II-H data, obtained from *Hinode*/SOT. Left panel, taken from De Pontieu et al. (2007c). shows most probable lifetimes (∼45 seconds) for spicules, while right panel shows the median wave-periods of around 44.8 seconds, taken from Okamoto and De Pontieu (2011).

temporal domains to understand any possible relationships between these observed parameters. The unperturbed cross-sectional width (W) is found to be 156±24 km, as compared to 360±120 km for on-disk fibril structures (Morton et al., 2012a), 260 km for RBE/RREs (Kuridze et al., 2015) and on-disk SCF structures by Gafeira et al. (2017a). The power-spectral density (PSD) estimate is taken at each time-step (t) for $t = 1,2,3,...T$, over height to understand the wavenumber (k_z) dependence of these parameters over time. Similar estimates were taken at each height (H) over time, to analyze the evolution of observed parameters in the frequency (f) domain. The averaged-PSD is then defined as $< \hat{g}_{ii}(k_z) >, < \hat{g}_{jj}(f) >$ and given as

$$< \hat{g}_{ii}(k_z) >= \frac{1}{T} \sum_{t=1}^{T} \left| \hat{g}_{ii}(k_z) - \bar{g}_{ii}(k_z) \right|, \tag{4.8}$$

$$< \hat{g}_{jj}(f) >= \frac{1}{H} \sum_{H=1}^{H} \left| \hat{g}_{jj}(f) - \bar{g}_{jj}(f) \right|, \tag{4.9}$$

where, $\bar{g}_{ii}(k_z)$ and $\bar{g}_{jj}(f)$ are the mean magnitudes of the estimated PSDs taken as the background noise and are removed at each time/height-step.

The estimated averaged-PSD for displacement ($\delta\xi_r$), cross-sectional width ($\delta\xi_W$), intensity (δI) and azimuthal shear/torsion ($\delta\xi_t$) fluctuations are shown in the Figure

4.4a,b in the wavenumber (k_z) and frequency (f) domains respectively. The region enclosed (λ_z = 4454 - 1451 km) by the half-max of the peak PSD (λ_z = 2800 km) of the resultant displacement and the subsequent parameters, is highlighted by the shaded region (Fig. 4.4a). The coincided peak PSD magnitudes for all the four observed parameters indicate a strong coherence between these observables at smaller (larger) wavenumbers (wavelengths). The remainder region with increasing wavenumber (k_z) shows an exponential decay in averaged-PSD estimates for all the observed quantities. The strong coherent behavior between these observables is also evident in the frequency (f) domain. In here, the results are two-fold.

First, the observed parameters ($\delta\xi_r, \delta\xi_W, \delta I$) show peaks at 0.013 Hz (77 sec) and 0.039 Hz (25.6 sec), i.e., a secondary peak at around thrice the frequency of the primary peak, marked by the vertical solid lines in Figure 4.4b. Second, the azimuthal shear/torsion ($\delta\xi_t$) component shows a peak at 0.026 Hz (38.4 sec), at twice the frequency ($f_{\delta\xi_t} = 2f_{\delta\xi_r}$) at the primary peak (at 77 sec) of the resultant displacement and other observables. This peak in the averaged-PSD magnitude for the azimuthal shear/torsion component is located at the "first harmonic", where the other observables show a deficit in the frequency domain. This subsequent period-doubling and -tripling pattern in frequency domain (Jiang et al., 1998; Linsay, 1981) for observables could indicate the nonlinear nature of the spicular dynamics. However, the existing nonlinear-kink (analytic/numeric) models have only produced period-doubling (Magyar and Van Doorsselaere, 2016; Ruderman et al., 2010; Ziegler and Ulmschneider, 1997a,b), and have not yet produced period-tripling. The 3D visualizations of these coupled dynamical components are shown in Figure 4.9.

The observed coupled transverse and non-/axisymmetric deformation of the MFT cross-section could partly be due to the injected photospheric perturbations (as assumed in previous studies) and/or as a consequence of the flux tube to maintain the local pressure equilibrium at the tube surface. The transverse dynamics of the waveguide, in principle, should be resisted by the inertia of the spicular plasma (ionized, partially-ionized and neutrals). This can result in a non-axisymmetric deformation of the MFT cross-section with an anti-correlation between plasma and magnetic pressures, in an attempt to maintain the overall pressure equilibrium. While, the gradients in the plasma pressure due to confined kink waves were already reported as acceleration at the transverse nodes by Sharma et al. (2017), it is highly reasonable to assume the deviation of spicular cross-sectional geometry to a non-circular case, to compensate the asymmetry in pressure distribution between forward and backward sides of the moving waveguide (see upper panel, Fig.4.9).

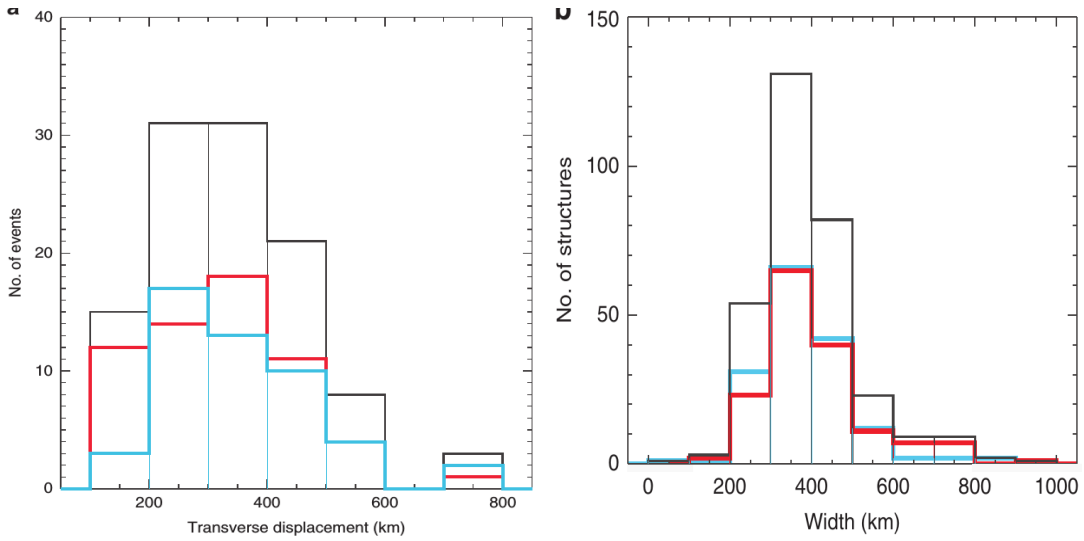

Fig. 4.8 A comparison between the observed transverse displacement and cross-sectional width for the on-disk Hα fibril structures is shown. Left panel shows the transverse displacement of the observed waveguides, which for most of the cases had nearly the same magnitude as for the cross-sectional width ($\sim$300 km). The plots here are taken from Morton et al. (2012a).

The physical explanation is well supported by the observed amplitudes for perturbed transverse displacement ($\delta\xi_r$) and the cross-sectional width ($\delta\xi_W$) oscillations, which are comparable (Fig. 4.4c). Similar observations (Fig. 4.8) were reported by Morton et al. (2012a) for on-disk fibrils. Since, the overall cross-sectional width and the associated photometric variations are directly related to the pressure perturbations, linked with the tube dynamics, it is expected for these to be coupled at similar wavenumbers and frequencies. This aspect is statistically supported by the observations of comparable periods for cross-sectional width and intensity oscillations for on-disk SCF structures, reported recently by Gafeira et al. (2017a).

The coupling between the transverse ($\delta\xi_r$), cross-sectional width ($\delta\xi_W$) and the azimuthal shear/torsion ($\delta\xi_t$) parameters could also be attributed to the magnetic tension forces and/or longitudinal plasma pressure perturbations. When the local curvature is formed between the mean-axis and the maximum displacement, there will be components, both perpendicular (vertical) and along (horizontal) the direction of transverse displacement. Over a single wave-period, these vertical components will reverse their sign twice as compared to the horizontal component. It must, however, be noted that similar vertical components associated with plasma pressure changes would also be present in the spicule due to cross-sectional width variations. The frequency analysis, as shown in Figure 4.4b, hints towards the proposed mechanism, with the azimuthal shear/torsion component ($\delta\xi_t$) having twice the frequency ($f_{\delta\xi_t} = 2f_{\delta\xi_r} =$

$2f_{\delta\xi_W}$) as compared to that of the primary peak in the frequency for the transverse displacement ($\delta\xi_r$) and cross-sectional width variations ($\delta\xi_W$). Similar interpretations were proposed by (Ulmschneider et al., 1991; Ziegler and Ulmschneider, 1997a) for their numerical analysis of the dynamics of the thin MFT structures. These changes in the vertical component will result in longitudinal compressions and rarefactions which will further perturb the associated Lorentz forces, visible as the azimuthal shear/torsion (see lower panel, Fig.4.9). Under the influence of longitudinal compressions and rarefractions, the perturbed azimuthal shear/torsion ($\delta\xi_t$) will further showcase upward and downward motions along the spicular structure (see, supplementary material for Fig.4.9). This longitudinal motion of the perturbed Lorentz forces was highlighted by Kitiashvili et al. (2013) in their numerical simulations of vortex tube dynamics.

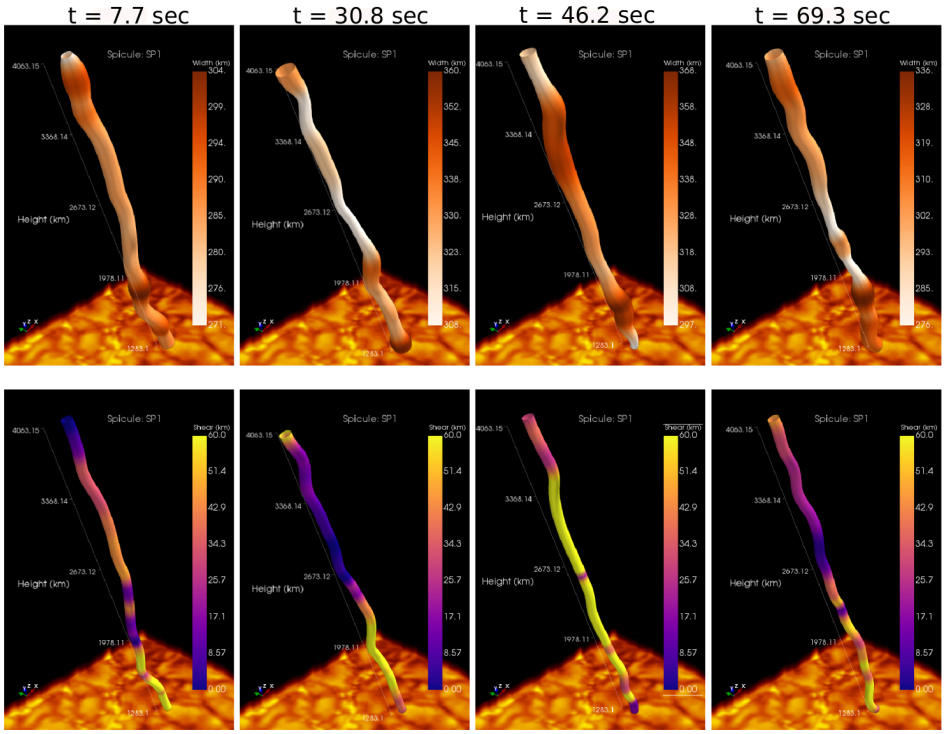

Fig. 4.9 3D visualizations of the coupled evolution of resultant transverse displacement (ξ_r), cross-sectional width ($\xi_{W'}$) and azimuthal shear/torsion (ξ_t) parameters are shown for an arbitary view-angle. Top panel highlights coupled transverse and width (W'), with intensity taken in proportion to cross-sectional variations at four time-steps (7.7 sec, 30.8 sec, 46.2 sec, 69.3 sec). The visualization here assumes an axisymmteric variation in the cross-sectional width. Bottom panels showcase the transverse and azimuthal shear components. The azimuthal shear/torsion component magnitude exhibits field-aligned upward and downward motions, possibly due to perturbed Lorentz forces.

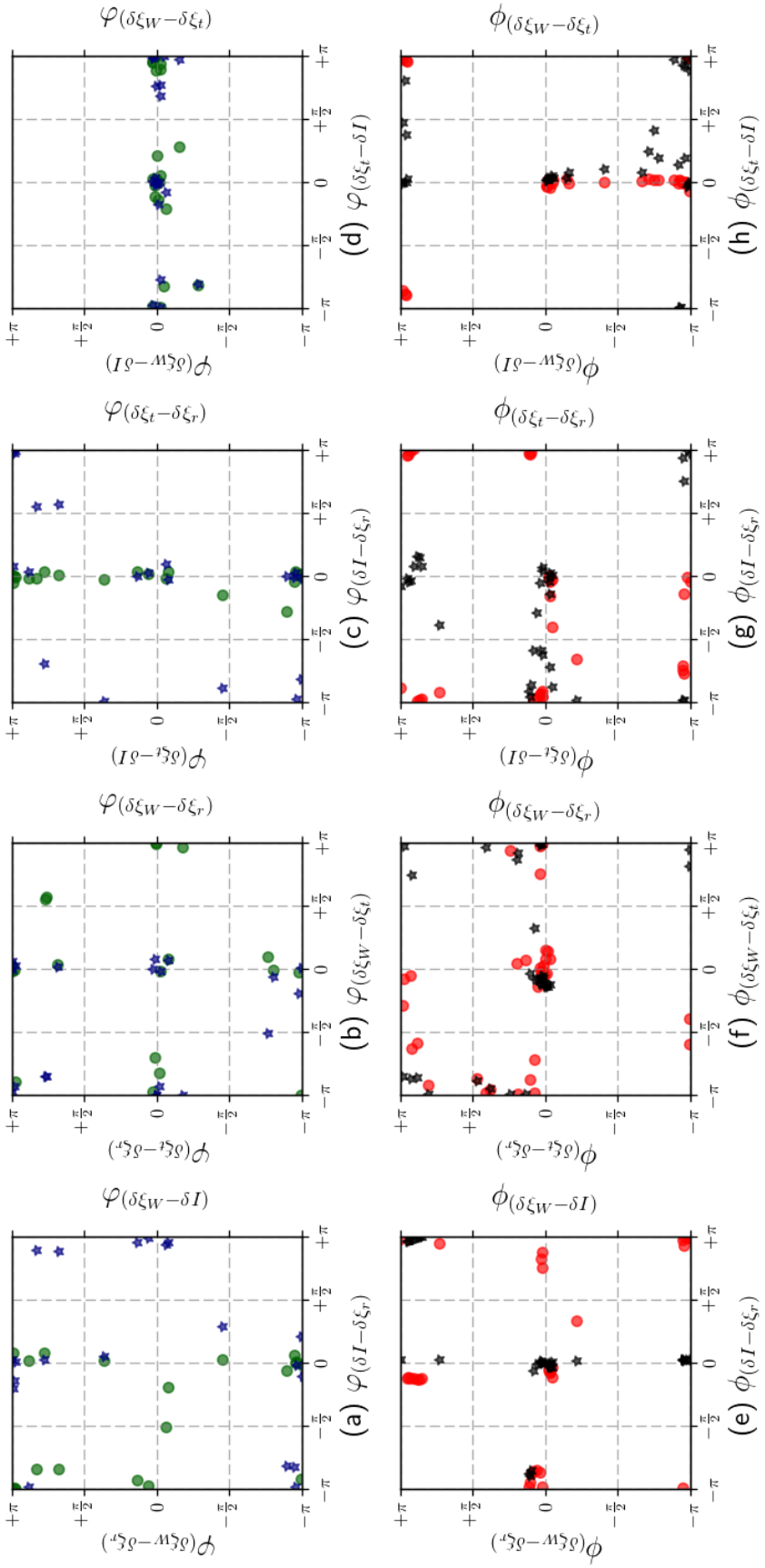

Fig. 4.10 Scatter plots showing mutual variations of the estimated phase relations in frequency (a-d: f) and wavenumber (e-h: k_z) domains for different observables. The mutual phase relations between the parameter-pairs on x-axis and y-axis (on left) are marked as circle, while the relationship with the parameter-pairs between x-axis and y'-axis (on right) are marked here as star. The phase differences are mostly concentrated around 0° and $\pm\pi$° with a deviation of $\pm$30°. Any further deviation of the mutual phase relations could be indicative of the nonlinear evolution and/or background noise contribution from the small-scale dynamics at the spatial/temporal scales below current observational resolution limit.

The strong coupling between the observables is also evident from the evolutionary trends estimated at different heights. Figure 4.4c shows the observed parameters at four consecutive heights (1.92, 2.56, 3.20, 3.85 Mm) above the visible limb with σ error marked as shaded regions. A visible overview of the cross-sectional width ($\delta\xi_W$), photometric (δI) and azimuthal shear ($\delta\xi_t$) components show clear signatures of both in-phase and out-of-phase behavior with the resultant displacement ($\delta\xi_r$) of the spicular waveguide. For better understanding of the coupled behavior, the phase relationships between paired parameters were estimated using the cross-spectral densities (CSD) in the spatial and temporal domains by the procedure described in section 3.5. The mutual variations in-between the estimated phase angles show the phase difference congregated around 0° and $\pm 180^\circ$ with a deviation of $\pm 30^\circ$ for the spectral bins located in wavenumber (λ_z in highlighted region, Fig. 4.10a-d) and frequency (f = 0.013 Hz, Fig. 4.10e-h). However, the phase angles for cross-sectional width, intensity and azimuthal shear/torsion pairs in wavenumber (Fig. 4.10d) and frequency (Fig. 4.10h) domains appears to be strongly concentrated around 0° indicating collective behavior, rather than uncoupled azimuthal shear/torsion and sausage-type motions.

4.4 Conclusions

The main conclusions from the study, presented in the chapter, are as follows:

1. For the first time, the resultant displacement ($\delta\xi_r$) estimated from both the POS and LOS velocity components were analyzed with the cross-sectional width ($\delta\xi_W$), photometric (δI) and azimuthal shear/torsion ($\delta\xi_t$) variations for off-limb spicules. Time-distance (TD) plots show the displacement of the oscillatory axis of the spicular structure in both the perpendicular planes of motion, indicating the presence of the kink wave-mode, with periodic longitudinal (field-aligned) flows (V_f). Observations of spicular waveguide and TD analysis further reflected the '*pulse-like*' behavior of the wave mode with the dominant period of the order of the flux-tube's lifetime.

2. Concurrent temporal and spectral (k_z, f) analysis showed profound coupling between the observables ($\delta\xi_r, \delta\xi_W, \delta I, \delta\xi_t$) over the tube/period-scale, supported by the mutual phase relationships. The frequency (f) analysis showed a period-doubling and -tripling aspect for these quantities which could indicate the nonlinear behavior of the system. An important aspect to note here is, that the peak-frequency of the azimuthal shear/torsion component was located exactly

where other observables had lost their power densities, with the frequency (period) twice (half) as that of the primary peaks of the transverse displacement and cross-sectional width variations. The observed behavior could also be explained in terms of the linear MHD theory, with independent wave-modes coupled in the presence of the magnetic twist (internal and/or external) and/or irregular shape in MFT waveguides (Giagkiozis et al., 2015; Terradas and Goossens, 2012). Due to the presence of the twist, a single *pulse-like* driver can result in the coupling observed in wavenumber and frequency domains. However, in the absence of the twist, a fine-tuning would be essential for all the drivers of the kinematic parameters, associated with the observable wave-modes, which is highly unlikely.

3. The investigation opens a way to obtain more accurate information about the actual complex 3D spicular motion, whose components were earlier identified ubiquitously/independently as transverse, field-aligned, rotational and cross-sectional motions by the numerous studies listed in the Introduction section. This study also provides much needed insight into the coupled behavior of the different dynamical components of the spicule motion.

Chapter 5

Coupled evolution of transverse dynamics with height: Helical vs. Non-helical motions

5.1 Background

Kinematic wave-modes, that include the transverse oscillations, along with the associated cross-sectional width and azimuthal shear/torsion variations were found omnipresent, in both, on-disk and off-limb MFT structures, and are key to the conduct of the energy across the interface-region. These motions reflect the dominant linear/nonlinear MHD wave-mode behavior, confined in the observed thin MFT waveguides, and were primarily analyzed, for their *independent* evolution in time and also for the estimation of associated wave energy flux. A few, theoretical (e.g., James et al., 2003; Shibata and Suematsu, 1982), as well as, observational (e.g., Khutsishvili et al., 2017; Morton, 2014; Stangalini et al., 2017; Zaqarashvili and Skhirtladze, 2008) studies, however, did examined the evolution of the longitudinal wave motion, to understand the origin and dynamics of the transverse motions.

De Pontieu et al. (2007d) observed the ubiquitous transverse motions in the spicule structures, in the *Hinode*/SOT data, and reported the presence of the Alfvén wave-mode in chromospheric MFT structures, though, this interpretation was later questioned in many consequent studies (e.g., Erdélyi and Fedun, 2007; Van Doorsselaere et al., 2008; Zaqarashvili and Erdélyi, 2009). However, Zaqarashvili and Skhirtladze (2008) suggested that the helical kink motions could be responsible for the observed transverse oscillations in the observed spicule structures. They proposed that a MFT waveguide emanating from the solar photosphere, could experience continuous buffeting from

the granular cells at its foot-point. This photospheric buffeting action can inject (single/multiple) kink pulse in the observed feature, which while propagating up, through the stratified solar atmosphere, appears like transverse oscillation, as reported by De Pontieu et al. (2007d). They further highlighted the *helical* behavior of the polarized dynamic components of the injected kink pulse, in different planes of motion (towards and perpendicular to the observer's LOS).

Though, kink waves can displace the flux tube axis, the degree of polarization and the associated plane of dominant motion will depend strongly on the foot-point driver. In case, multiple kink waves are injected into the waveguide, the resulting transverse motion would be more complex and the linear superposition of the injected waves. Zaqarashvili and Skhirtladze (2008), for two linear kink waves, polarized in perpendicular planes, suggested that the overall *helical* transverse motion would be circularly polarized, for equal amplitudes of the two kink waves, and elliptically polarized, for unequal kink amplitudes, with dominant motion in the plane of the kink wave with the higher amplitude. Stangalini et al. (2017) traced the photospheric foot-point motions and concluded the observed foot-point motions to evolve into the helical kink behavior, in the chromospheric flux tube structures.

However, it must be noted that, these studies only considered the superposition of the linear kink waves in spicular structures, without any possible contribution from the other observed kinematic components (e.g., cross-sectional width and azimuthal shear/torsions). This chapter investigates the complex motions of the spicule structures across the interface-region, through spatial-, temporal- and spectral-analysis. Observed dynamic parameters, with associated multiple/nonlinear wave-modes are examined, to understand the overall transverse motions, for the structures in complex chromospheric environment.

5.2 Method and analysis

For the sake of continuity, the spicule case (SP1) analyzed for the nonlinear kink behavior in Chapter 4, is used again for the study. The observed physical parameters (height, length, lifetime, inclination, etc.) of the spicule are summarized in Table 2.1. The estimation of the observed kinematic components, like transverse displacement in both LOS and POS planes, resultant transverse motion, cross-sectional width and azimuthal shear/torsion for the spicule (SP1), from imaging-spectroscopy data are discussed in detail in Chapter 4 (Section 4.2). All these observables were found strongly coupled in spatial-, temporal- and spectral analysis, with fixed phase relationships.

Moreover, nonlinear evolution of these coupled parameters was highlighted by the period-doubling, -tripling character in the frequency domain, in Chapter 4. Here, the principal aim is to analyze the evolution of the estimated kinematic components over height and time, and to identify the presence and signatures of multiple kink (linear/nonlinear) in the spicule structure, which could affect its observed dynamics. For this purpose, at each time-step, the observed POS and LOS transverse components, over height, are projected on the plane (of motion), as *Lissajous-like* plots [1]. These plots showcase the transverse behavior as helical/non-helical across the interface-region. To understand the coupled evolution in the spectral domain, the power-spectral density (PSD) estimate is taken at each time-step (t) for $t = 1,2,3,...T$, over height to understand the wavenumber (k_z) dependence of these parameters over time. Similar estimates were taken at each height over time, to analyze the evolution of observed parameters in the frequency (f) domain. The PSD is then defined as $\hat{g}_{ii}(k_z), \hat{g}_{jj}(f)$ and given as

$$\hat{g}_{ii}(k_z) = |\hat{g}_{ii}(k_z) - \bar{g}_{ii}(k_z)|\,, \tag{5.1}$$

$$\hat{g}_{jj}(f) = \left|\hat{g}_{jj}(f) - \bar{g}_{jj}(f)\right|, \tag{5.2}$$

where, $\bar{g}_{ii}(k_z)$ and $\bar{g}_{jj}(f)$ are the mean magnitudes of the estimated PSDs taken as the background noise and are removed at each time/height-step.

5.3 Results

Figure 5.1 show the spatial and temporal evolution of the POS and LOS transverse components over height. A sinusoidal function is fitted to the data to extract the trend (marked as the dashed-line) of the tube-scale motion, with the high-(k_z) residual perturbations ($\delta\xi_{pert}$), shown in Figure (5.1, 2(a-c)). A visual inspection of the plots indicate two-fold results. First, the POS and the LOS components of the transverse dynamics, with high and low wavenumber (k_z), are in the opposite phase with a varying lag (Fig. 5.1, 1-2(a-c)). Second, the strong deviation of the perturbed transverse motion from the helical behavior (Fig. 5.1, 4(a-c)), suggests nonlinear evolution of the transverse dynamics with height.

[1] Representation of two orthogonal simple harmonic oscillations on a plane of motion

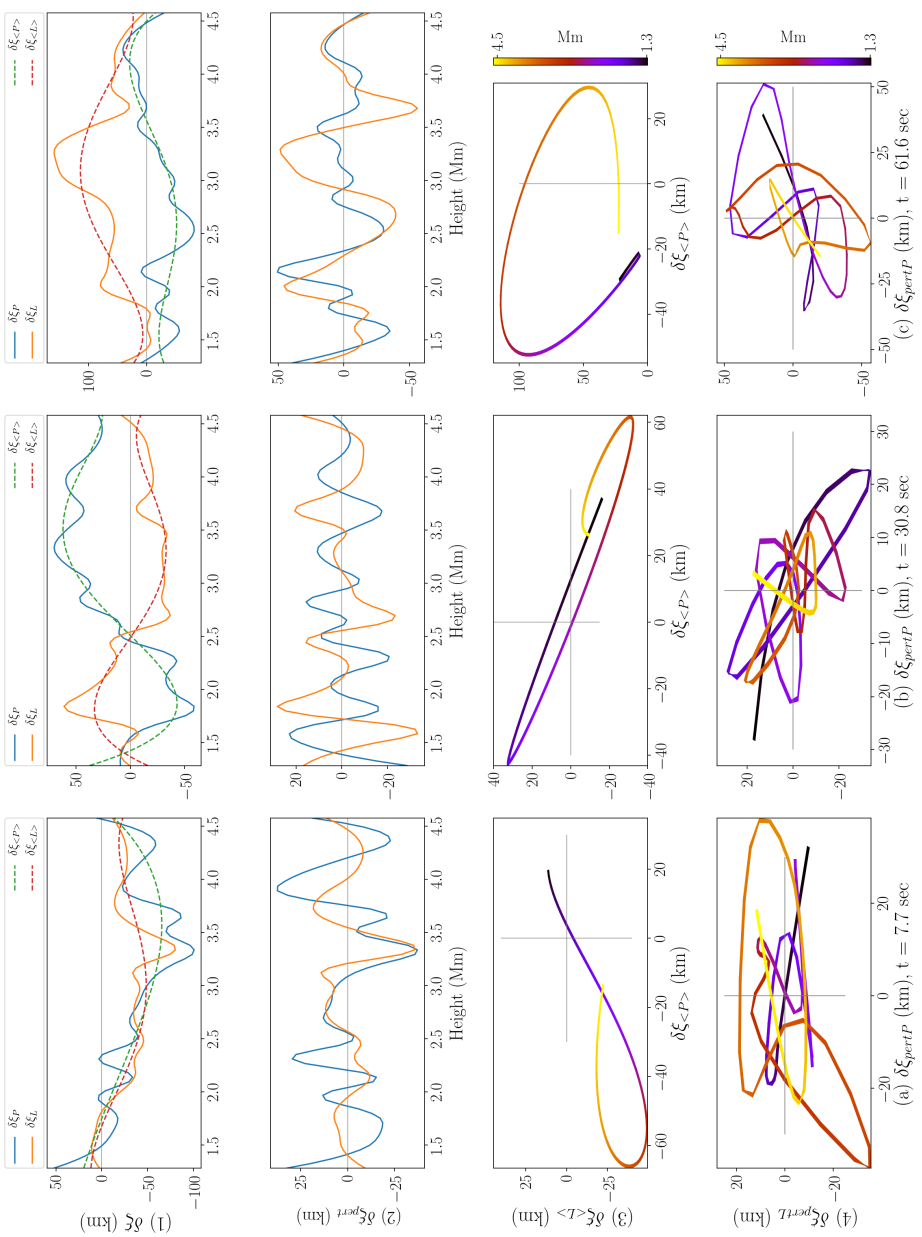

Fig. 5.1 Panels (a-c) shows the evolution of the estimated transverse components (POS-LOS), for spicule SP1, at three time-steps (7.7 sec, 30.8 sec, 61.6 sec) over height, along with the *Lissajous-like* plots to highlight the non-helical behavior. Top panel (1) show the POS-LOS components with a sinusoidal function fit (marked as a dashed-line), indicative of the dominant trend of the motion in perpendicular planes. The perturbed parameters ($\delta\xi_{pert}$), estimated by removing the fit (trend) from the estimated data is shown in panel (2). The perturbed parameters show the POS and LOS components in the opposite phase with a varying lag. The *Lissajous-like* plot for the fitted function and the perturbed parameters are shown in panels (3) and (4), respectively. Panel (3) highlights the evolution of the inherent trend, with height, while the plot in Panel (4) shows the associated complexities. The crosshair marks the mean location of the spicule motion in the plane of motion.

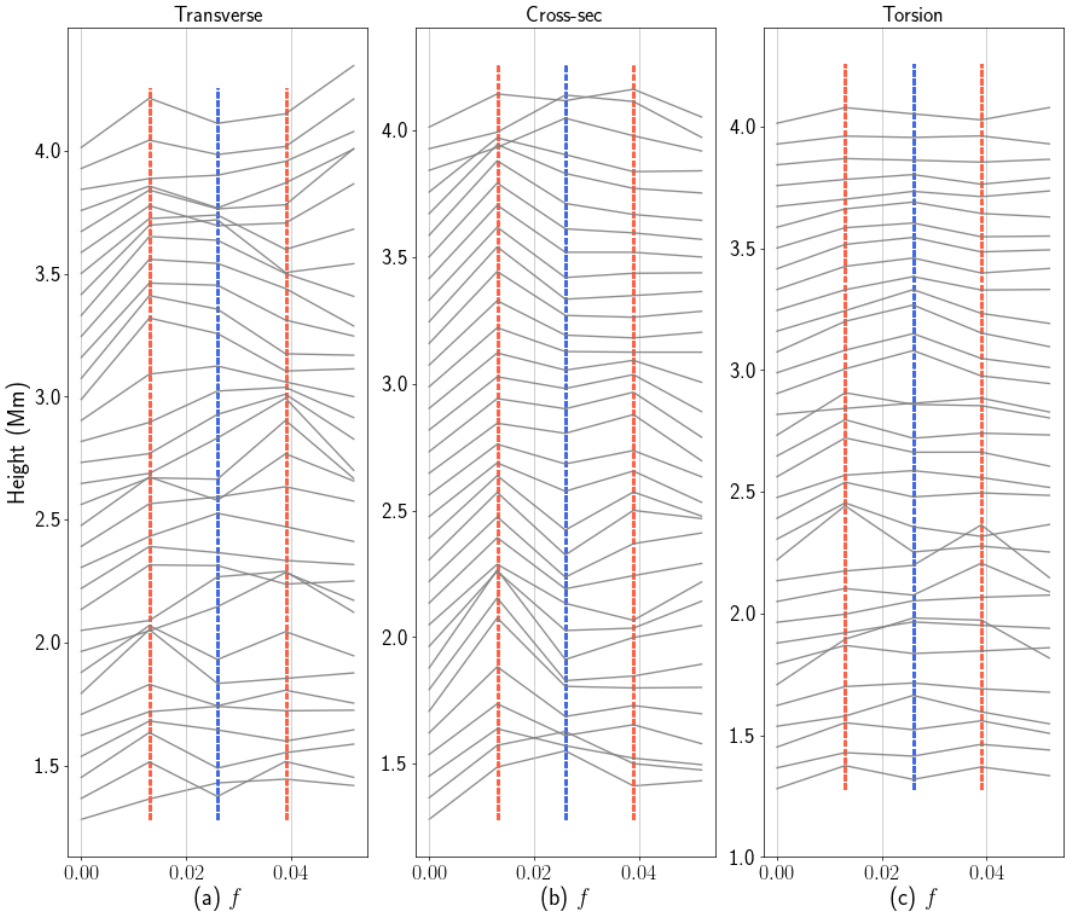

Fig. 5.2 Panels showing the distribution of frequency f estimates for transverse (a), cross-sectional width (b) and azimuthal shear/torsion (c) parameters with height. Two dashed lines, namely, (red) at 0.013 and 0.039 Hz, respectively, mark the location of enhanced PSDs for transvere and cross-sectional width parameters, similar to the Figure 4.4b, where an average of these estimates are shown. The vertical line (blue) at 0.026 Hz marks the position of the PSD enhancements for azimuthal shear parameter.

Similar observations for out-of-phase behavior, with a lag were reported for oscillatory prominence threads by Okamoto et al. (2015), and recently, for spicular structures by Khutsishvili et al. (2017). In their study, Okamoto et al. (2015) examined various theoretical scenarios, that included resonant absorption and possible presence of multiple flux tubes in the observed structure to explain the out-of-phase behavior and coherent POS-LOS velocities. However, it should be noted that, the resonant absorption occurs at very fine spatial-scales, which is beyond the scope of examination with the current observational capabilities. However, Antolin et al. (2015) in their numerical simulations, along with forward-modeling of the transverse flux tube motions, found similar out-of-phase patterns in the intensity and Doppler velocity components,

and emphasized the role of azimuthal flows at the flux tube boundaries in the observed phase-shift. The evolution of these transverse motions with height for spicule structures, having the ambient plasma density decreasing rapidly (see Fig. 1.3a), were studied by Zaqarashvili and Skhirtladze (2008). In their study, they postulated that the amplitude of the transverse oscillations should increase with the apex of the flux tube structure, while exhibiting helical motion. However, their analysis did not included the observed nonlinear effects, like the multiple wave-modes, out-of-phase behavior and phase-lag, that could result in highly complex and possibly non-helical motions in spicules. Okamoto and De Pontieu (2011), in their analysis found that there also exists a mixture of upward, downward and the resulting temporary standing waves, due to the reflection of the confined waves at the transition-region. These different transverse waves, with a plethora of phase-speeds, do evolve with time and height and can in fact lead to non-helical motions, though this aspect was not examined in their study.

To further investigate any possible role, of the multiple wave-modes in the observed non-helical behavior, spectral analysis in both spatial (wavenumber) and temporal (frequency) domains was performed, as described in Section 5.2. The evolution of the frequency (f) estimates of the parameters with height, and wavenumber (k_z) with time, are shown in Figures, 5.2 and 5.3, respectively. Frequency estimates show two peaks at 0.013 Hz and 0.039 Hz, which were concluded as a signature of nonlinear period-tripling in Chapter 4. For most of the heights, the location of these peaks in the frequency domain, does not show any variations, though the changes in associated wave amplitudes are evident. However, at a few positions in height, the frequency peaks, for transverse and cross-sectional width parameters, show enhanced power at 0.026 Hz, where the PSD of the azimuthal shear/torsion component is dominant. This behavior might reflect the exchange of energy between different modes, as they evolve in time. The wavenumber (k_z), however, shows shift at the peak-location, with associated variations in the PSD magnitudes. Multiple peaks, with comparable amplitudes are found, during the temporal evolution, indicating the presence of different waves in the spicule structure. This outcome is consistent with the observations of multiple waves, both, propagating (upwards/downwards) and standing, reported by Okamoto and De Pontieu (2011).

The wavenumber position of the two most dominant peaks in Figure 5.3 is traced over time and is shown in Figure 5.4. The wavenumber (k_z) for the peak with the higher PSD magnitude is taken as the primary, while, with the other (second-highest) is taken as the secondary k_z. The primary peak corresponding to low-wavenumber (high-wavelength) shows a constant value over the time, with discrete variations for k_z estimates for the observed dynamic components. The estimates at those instance, attain

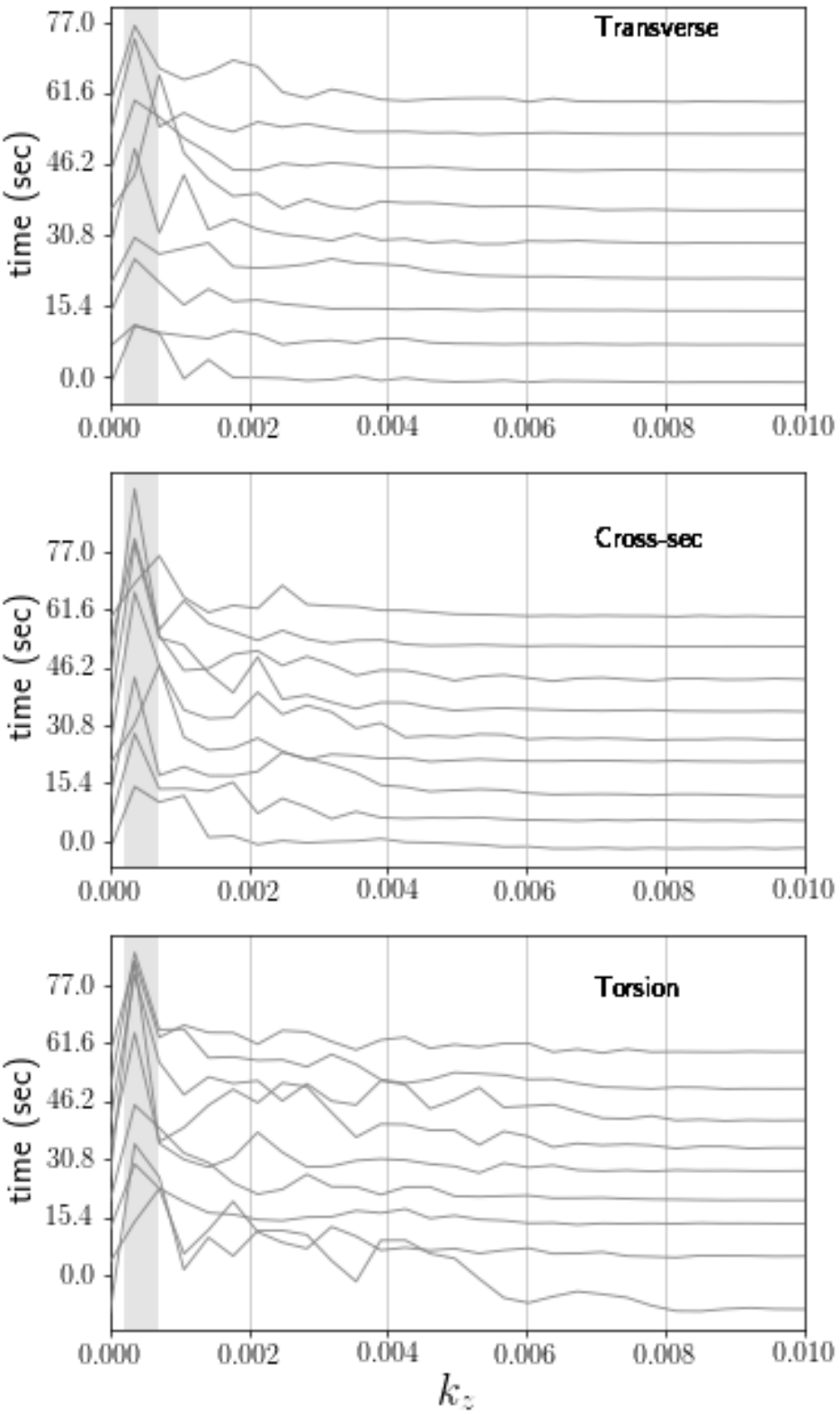

Fig. 5.3 The distribution of the wavenumber, k_z, estimates (top to bottom), with time, for the three observed kinematic parameters (transverse, cross-sectional width and azimuthal shear/torsion) are shown. Shaded region marks the half-max of the averaged-PSD in wavenumber domains, similar to Figure 4.4a, in Chapter 4. The estimated wavenumber parameters showcase PSD peak-shifting, along with multiple peaks with comparable magnitudes, indicating the presence of multiple waves, confined in the spicule structure. k_z range corresponding to 100 km are shown, which is the spatial resolution limit for the data.

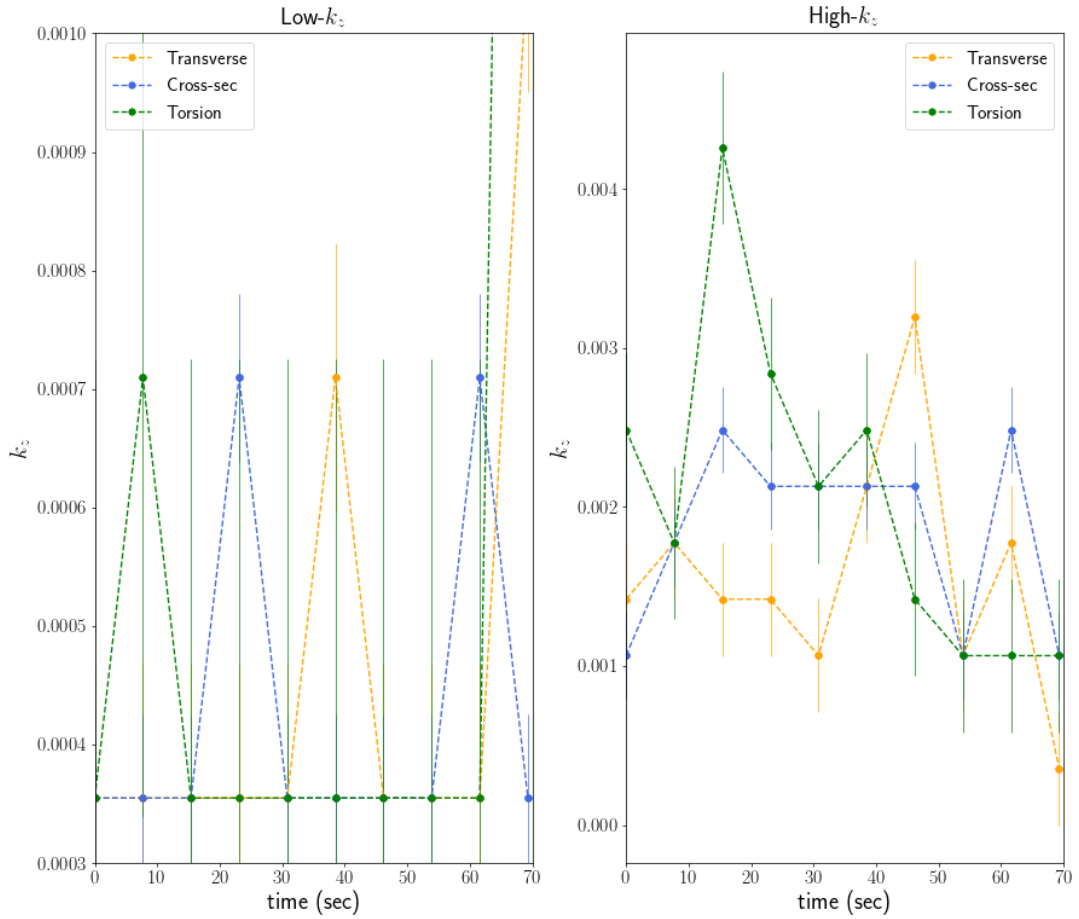

Fig. 5.4 Temporal evolution of the wavenumber (k_z) associated with the two dominating PSD peaks, along with errorbars marking $\pm\sigma$. Left panel showcase the variations for the low-k_z, which is primarily concentrated at k_z, corresponding to $\sim$2800 km wavelength. Deviations of k_z to double its magnitude, by different parameters, at discrete time-steps, might indicate *wavelength-halving* character, similar to the nonlinear period-doubling in the frequency domain. Right panel shows the high-wavenumber component, which shows strong variations with time for the analyzed observed parameters. This behavior might be due to the inhomogeneous chromospheric environment and/or presence of multiple wave-modes with different phase-speeds.

a k_z value with twice the magnitude (or, *half*-wavelength) as before. This behavior is somewhat similar to the period-doubling aspect of the nonlinear waves in frequency domain (see Fig. 5.4). However, the secondary peak, with high k_z (or shorter wavelength), shows strong variations in time for all the three observed kinematic parameters. This gives an impression of a strong coupling between the waves with higher k_z, to the inhomogeneities of the local chromospheric environment. It must be noted that the solar interface-region is highly complex, gravitationally stratified region, with magnetic pressure varying over unity. Furthermore, the presence/superposition of multiple kinetic wave-modes confined in the spicular waveguide, can also result in variations in the wavenumber estimates. The possibility of energy exchange between the observed kinematic modes through linear/nonlinear mechanisms is also possible. Nevertheless, it appears that the complex motion observed for the spicule structure is actually due to a combination of two (and more) MHD wave modes. The corresponding wavenumbers k_z for these modes suggests that mode with primary wavenumber (low-k_z) dominates the overall motion of the flux tube in both perpendicular observational planes (POS and LOS), while mode with secondary wavenumber (high-k_z) is responsible for the complex, non-helical motion. The *feed-back/response* from the secondary wavenumber peak deviates the spicule motion from the ideal helical behavior, as expected from a single kink wave.

The coupled ensemble of multiple/nonlinear wave-modes with transverse displacement and cross-sectional width parameters are visualized in 3D, in Figure 5.5. The cross-sectional width variation for the spicule structure is assumed here as axisymmetric, however, that might not be the case with nonlinear motion due to kink wave-mode(s) in the spicule structure. The three time-steps are visualized at different phases of spicule's lifetime, with the overall structure undergoing non-helical motion, as shown in Figure 5.1. Presence of multiple kinematic components can further complicate the dynamics of spicule structures in solar chromosphere and strongly influence the evolution of injected motion due to buffeting at spicule's footpoints.

5.4 Conclusion

Coupled dynamical components, that consist of transverse displacement, cross-sectional width and azimuthal shear/torsion components are examined to understand the motion of the spicule structure, across the interface-region. Spatial-, temporal- and spectral-analysis of the estimated parameters, indicate the complex, nonlinear behavior of the

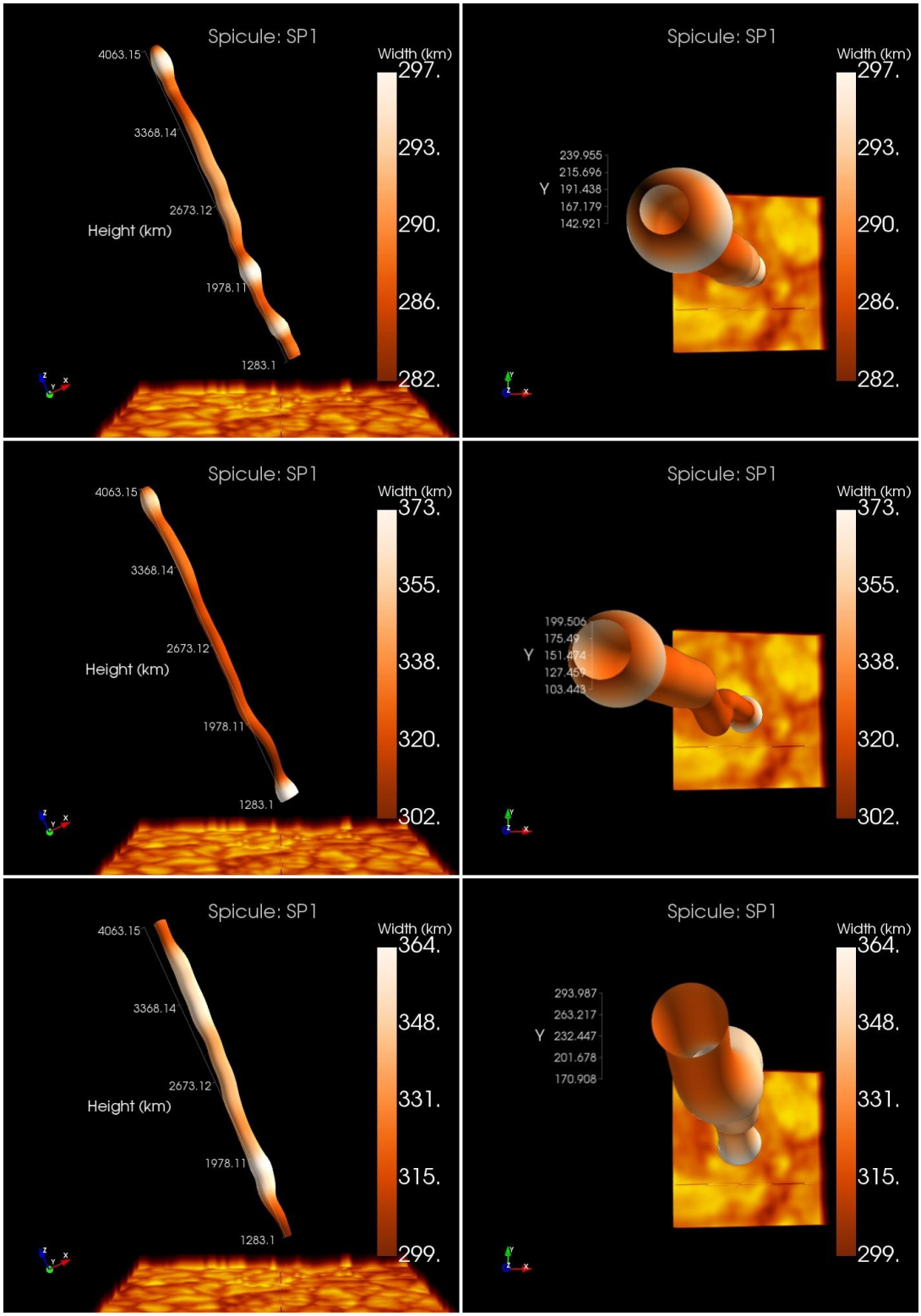

Fig. 5.5 Panels (top to bottom) show 3D visualization of the coupled transverse and cross-sectional width parameters over height, for three time steps (7.7 sec, 30.8 sec, 61.6 sec), respectively. Panels on the left show the POS-view of the spicule (SP1) kinematic components, while those on right highlight the top-view. Color-scale is in proportion to the cross-sectional width, with an axisymmetric assumption of variation in width. The position of the photosphere (not to the scale) is marked by a G-band image from *Hinode*/SOT data.

spicular dynamics, with strong coherence in the studied estimates. Key conclusions from the study are as follows:

1. The transverse displacement components in POS and LOS are coupled in the opposite-phase with a lag. The simulation/forward-modeling from recent studies (e.g., Antolin et al., 2015; Okamoto et al., 2015), claim the role of the resonant absorption phenomenon in the observed behavior, though, it is not possible to examine the proposed theoretical mechanism directly through observations.

2. The spatial evolution of the coupled transverse components reveal non-helical motions of the spicule structure, across the interface-region, with two (and more) kink wave-modes. These observations are in contradiction with some previous studies (Stangalini et al., 2017; Zaqarashvili and Skhirtladze, 2008), as they only considered a single kink pulse, with dynamical components, polarized in the perpendicular planes of motion.

3. Spectral analysis in the frequency (f) and wavenumber (k_z) domains, for the observed parameters, highlight the presence of multiple wave-mode(s). Though, the spatial (height) evolution of the frequency (f) estimates shows concentration of PSD magnitudes at 0.013 Hz and 0.039 Hz for transverse displacement and cross-sectional width parameters, and at 0.026 Hz for the azimuthal shear/torsion parameters, with mutual exchange of PSD at some heights. The wavenumber (k_z) estimates over time show multiple peaks that shift their locations.

4. The low-k_z component of the wavenumber shows nearly constant location, with occasional shift to double k_z location, by all three analyzed parameters. However, the high-k_z element shows strong changes over time, which could be due to the local plasma and magnetic inhomogeneities, in the chromospheric atmosphere.

5. It is possible that the high-k_z component could be accounted for the observed complex and non-helical motions in the observed spicule structures.

Chapter 6

Conclusions and Future work

6.1 Overview of the thesis

This thesis primarily concerns with the dynamical behavior of thin magnetic flux tube structures observed in the solar chromosphere and their accurate interpretation in terms of the magnetohydrodynamic (MHD) wave modes. Spicule structures observed at the solar limb, using high-resolution imaging-spectroscopy data (Chapter 2) were analyzed for the three-dimensional (3D) overview of their kinetics. Up until now, most studies devoted to understand the role of these features in the mass, energy and momentum transportation, were restricted in either of the planes of motion (POS or LOS). For the first time, the observed dynamics of is studied by combining the perpendicular, plane-of-sky (POS) and the line-of-sight (LOS) kinematic components, at both, pixel- and tube-scales. Novel analysis methods were developed to combine the observed dynamical parameters, as described in Chapters 3 and 4, to gain insight into the true motions of the spicules. Cross-sectional width and azimuthal shear/torsion parameters were also studied to obtain a comprehensive overview of the nonlinear motions in these structures. Evolution of these kinematic estimates, in spatial, temporal and spectral domains, provided a step-forward in the understanding of the nonlinear motions in these structures. Furthermore, the non-helical complex motions (Chapter 5) in these features reflected the complicated nature associated with the propagation of the MHD wave-modes through the solar interface region. Major conclusions from this thesis, for each chapter as well as future prospects, are given in the sections below:

6.2 Conclusions

Chapter 2, mainly describes the imaging-spectroscopy data used in the thesis and also the selection of the spicule cases used throughout in the thesis. The data used in the study is in Hα spectral line, taken from the CRISP instrument at the Swedish Solar Telescope, for a duration of around 30 minutes. The high-quality data shows two active regions at the solar limb, along with complex *forest* of spicular structures. The superimposed spicule structures with their short-lifetimes and high velocities makes the selection of individual cases, a notoriously difficult task. Eight spicules, which were least-superimposed in the respective line-scan positions, during their lifetimes, were selected for the study. Their observed physical parameters (lifetimes, height, length, inclination, etc.) along with their dominant plane of motion were listed in this chapter. From Hα images from previous days, it is concluded that the spicules at the limb were originating from the quiet-Sun region. This information is key to estimate the magnetic pressure changes, associated with kink wave motion, in Chapter 3.

Chapter 3 highlighted the challenges associated with the accurate interpretation of the observed wave-modes (torsional Aflvén or kink) in spicule structures. It is a common belief that the kink wave motions are purely transverse in nature and no other motions are linked to them. However, theoretical and numerical studies in the past contradicted this view and proposed the coupled transverse (internal) and rotational (external) behavior in the flux tube structures, associated with the kink wave mode. The correct identification of the confined wave mode becomes even more difficult in observations, as, the Doppler estimates for both $m = 0$ torsional Alfvén wave-mode and $m = 1$ kink wave, show similar axisymmetric (red-blue) profiles. Here, it must be noted that the Doppler profile for torsional Alfvén wave is axisymmetric, *i.e.* independent of the observer's LOS, whereas, in case of kink motions, it strongly depends on it. Moreover, the *ideal* torsional Alfvén wave cannot displace the flux tube structures, while the kink wave *independently* can, in principle, displace the flux tube, and has the rotational profile due to the ambient plasma. Also, the surrounding magnetic and plasma environment would experience compressions and rarefactions due to kink motion, and would appear as discrete perturbation-profiles. Till date, the pressure perturbations in the ambient solar atmosphere, linked with the spicule motions was not possible, due to the observational and instrumentation limitations. To circumvent this problem, 3D velocity-vectors at each pixel were determined and proxies for plasma and magnetic pressure perturbations were estimated. Chapter 3, highlighted the coupled, LOS-dependent, transverse and rotational motions, associated with the kink wave mode, for two spicule cases with predominant POS and LOS motions and compared the

estimated pressure profiles to the expected theoretical models. The only assumptions taken into account for the estimation of the perpendicular velocity components were those related to the intensity motions (for POS), which are considered entirely due to the plasma motion, and not due to any thermal or seeing effects, and also the observed plasma colomn is optically thick, i.e., emission towards the observer are prominent. The results from this chapter are highly important for accurate identification of the confined wave modes in spicule structures. Discrete MHD wave-modes have their specific energy transfer and dissipation mechanisms, key to the understanding of the role of spicules in chromospheric/coronal heating.

Chapter 4 focuses on the evolution of the coupled dynamics in kinematic components of the observed spicule structure, at the tube-scale, in spatial-, spectral- and temporal-domains. Key dynamical parameters, like, longitudinal-flows, transverse displacement, cross-sectional width and the azimuthal shear/torsion, were estimated to analyze the spicule motion and the possible MHD wave modes confined in the waveguide. Field-aligned (longitudinal) flows were estimated by tracking the visible apex position of the inclined (23.6°) spicule structure with average velocities of the order of 41 ± 28 km/s. Here, it is assumed that the spicule is inclined in the observer's LOS with same angle as observed in the POS. The flow velocities were later used to correct the possible projection-effects that might affect the proper LOS Doppler velocity estimates. Transverse kinematic components in the perpendicular observational planes (POS, LOS) were estimated by using the time-distance (TD) plots, with each cross-cut at $\sim$172 km apart in height, on imaging and Doppler data. The TD plots highlighted a *pulse-like* behavior in the spicule structures, which was earlier hypothesized in theoretical and numerical studies. The resultant-vector of these two was further used to investigate the transverse dynamics. Apart from displacement parameters, cross-sectional width was also estimated over height by using a Gaussian fit on intensity profiles across the spicule structure. The Full Width at the Half-Max (FWHM) of the Gaussian function was taken as the proxy for the width of the structure. The mean-magnitude or the unperturbed cross-sectional width was found to be around 156 ± 24 km, with variations upto ±80 km. This information was utilized to estimate the azimuthal shear (average magnitude of 44 ± 39 km) across the spicular waveguide. All these parameters were studied in their spectral (for mutual phase relationships) and temporal domains.

Analysis also showed profound coupling between the observed kinematic parameters in temporal and spectral (both frequency and wavenumber) domains. Nonlinear behavior with period- doubling and tripling aspects was highlighted with an important finding on the relation between azimuthal shear/torsion and other dynamical parame-

ters. In the frequency analysis, the averaged-PSD peak for azimuthal shear component showed power where all other parameters had a deficit. Also, the frequency of shear component was located in middle of the primary and secondary peaks of the spectral peaks for all other estimated parameters. This behavior was anticipated from the numerical studies for thin magnetic flux tubes, but was observed for the first time in our analysis. Furthermore, the dynamical components, which were earlier studied/reported as independent kinematic modes (Chapter 1), were found strongly coupled with each other. A few studies (Jess et al., 2012; Morton et al., 2012a) which reported the coupled transverse and cross-sectional width, assumed axisymmteric variations in the tube structure, which might not be the case, and needs future investigation, supplemented with numerical simulations. The 3D visualizations for the coupled evolution of the observed dynamical parameters shed new light on the motions and revealed the inherent complexities associated with the spicule structures . Results from Chapter 4 may have strong implications for the kinematic energy-budget, such as, distribution of the total available energy in different wave modes, along with the partition of energy in between magnetic and plasma parameters and also energy transfer/dissipation mechanisms.

Chapter 5 examined the evolution of the coupled transverse dynamics of the spicule structure from the estimated kinematic components in the perpendicular observational planes (POS and LOS). Periodic transverse displacements were observed in the spicule waveguides and were interpreted to be the signatures of the confined MHD kink wave modes. However, the evolution of these transverse motions with height were found to be helical in nature, concluded through numerical studies and the tracking of photospheric foot-point motions of the chromospheric flux tubes. Our analysis showed that the oscillatory POS and LOS motions in height are strongly coupled in the opposite phase with a lag. The *lissajous-like* plots of these motions revealed non-helical nature of these complex transverse motions. Inspection of spectral estimates, indicated the presence of two nonlinear kink waves, confined in the observed waveguides with averaged-PSD peaks varying in time. This variation of the dominant peaks could be due to the chromospheric inhomogeneities and/or presence of upward and downward propagating wave components in spicule structures. Though, the upward/downward/standing waves in spicular waveguides were reported in previous studies, however, their effects on the transverse dynamics was yet unknown, and is showcased for the first time in our study. Moreover, the presence of other nonlinear dynamical components (cross-sectional width, azimuthal shear/torsion and field-aligned flows), can also affect the wave propagation though spicule structures across the solar interface region. The analysis presented in this chapter highlighted the complex motions pertinent to the spicular waveguides in the chromospheric environment.

6.3 Future work

The future prospects of this research is to extend the analysis with multi-wavelength diagnostics of the open (spicules, fibrils, mottles, etc.) and closed (arch-filament, loop-like) magnetic topology features, in the solar interface-region, observed in both active- and quiet-Sun magnetic background conditions. The research presented in this thesis, primarily relies on high-resolution data from CRISP/SST in Hα line profile at the limb, observed for a quiet-Sun spicule structures. However, it must be noted that the spicules are essentially multi-thermal structures and their physical behavior evolves from one line to the other (Pereira et al., 2014), with extended lifetimes. Furthermore, the role of the background magnetic field conditions on the observed dynamical behavior, of the magnetic flux tube structures, is yet, unclear and needs to be investigated. To address these challenges, successful observational campaigns from the Dunn Solar Telescope (in 2016) and the Swedish Solar Telescope (in 2017) were carried out. The high-resolution imaging-spectroscopy data from both observations in the multiple wavelengths (Hα, Hβ, Ca II) were complemented by co-spatial IRIS observations (Mg II, Si IV). A sample of the observed data in several wavelengths for on-disk structures is shown in Figure 6.1. Apart from these, forward modeling of the observed spectral lines is also envisioned to get a better insight into the response of the spectral lines to the complex dynamics of the flux tube features (e.g., Antolin et al., 2015; Okamoto et al., 2015). The specific science cases that would be pursued are as follows:

6.3.1 *Pulse-like* behavior in spicule structures

Observations of the spicular waveguides from *Hinode*/SOT, in Ca II passband, had shown that the overall lifetime of the feature is comparable to the estimated wave period (De Pontieu et al., 2007c; Okamoto and De Pontieu, 2011). This oscillatory behavior is observed as a *pulse*-like trait in the time-distance plots of these structures. The oscillations in spicules, due to a sudden impulse has recently been elaborated by numerical studies (Kuźma et al., 2017; Martinez-Sykora et al., 2017). Nevertheless, the origin of spicule structures, as a consequence of a strong pulse/shock is not entirely a new concept (De Pontieu et al., 2004; Hollweg and Roberts, 1981; Shibata and Suematsu, 1982; Sterling, 2000; Suematsu et al., 1982) and has remained a key possible mechanism for spicule generation. Furthermore, as a consequence of the propagating pulse, confined in the spicular waveguide, the other observed kinematic components (transverse, cross-sectional width, azimuthal shear/torsion) can couple

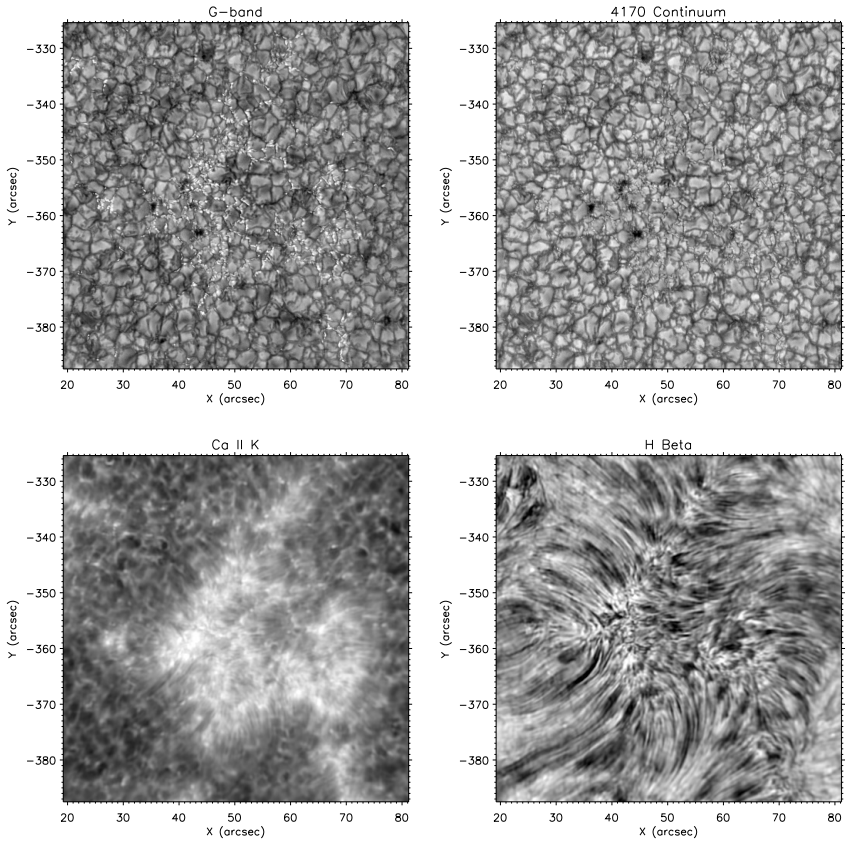

Fig. 6.1 Observations of quiet-Sun region in multiple wavelengths (G-band, continuum, Ca II and Hβ) from Dunn Solar Telescope on 21 October 2016. The G-band data acts as a tracer for the foot-point motions of the flux tube structures. The image clearly shows the granular cell structures on the solar photosphere, along with bright points in the intergranular boundaries, indicating the concentrations of the small-scale magnetic flux element. The corresponding continuum image shows magnetic pore structures, suggesting the flux emergence sites in photosphere. The Ca II shows bright plage regions, while the Hβ data clearly shows elongated, dark, filamentary structures, sprouting from these regions.

to the longitudinal flows. The possible coupling between periodic transverse and longitudinal motions did also appeared in previous numerical studies (James et al., 2003; Ulmschneider et al., 1991; Ziegler and Ulmschneider, 1997a,b), but lacks any conclusive evidence. Most of these studies, till date, have mostly been restricted to the numerical pursuit and demands observational investigations for structures emanating from different magnetic regions (active- and quiet-Sun). In the spectral analysis of an observed spicule (SP1), the different estimated kinematic components reflected strong coherence with the longitudinal mass motions. Figure 6.2 shows the dynamical parameters in frequency domain with the observed longitudinal flows, with two peaks at around 25 sec and 100 sec periods for field-aligned motions. The secondary peak

(at ∼100 sec) for longitudinal flows showed a higher magnitude as compared to the primary peak at 25 sec, reverse to the observed behaviour in frequency estimates for the transverse, cross-sectional width and photometric parameters. The secondary peak for transverse, cross-sectional width, intensity and longitudinal variations coincide at ∼25 sec. This provides strong indications for the coupled nature of the field-aligned and other dynamical parameters in spicular waveguides, and requires further investigation. In future, a combination of the state-of-the-art numerical simulations with multi-wavelength observations of spicule structures is foreseen to better understand the role of impulsive mechanisms in spicule generation and the observed dynamical behavior.

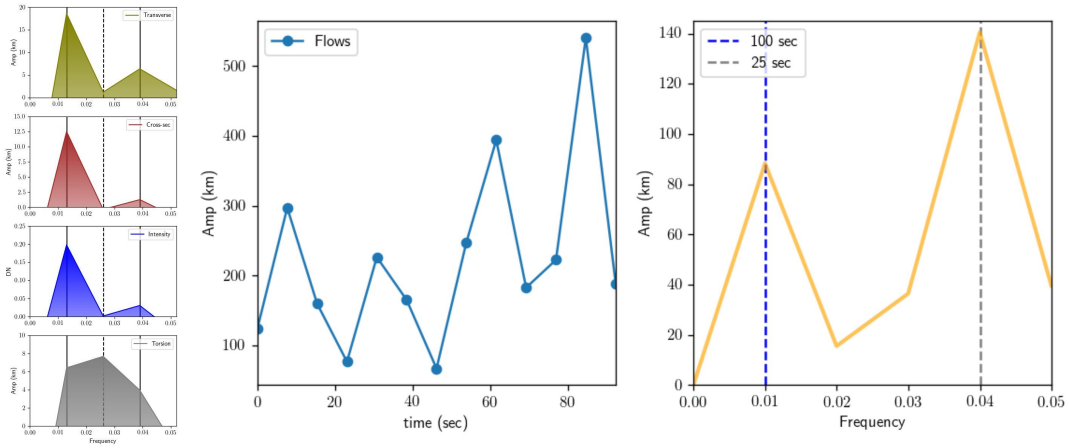

Fig. 6.2 Spectral analysis of dynamical components in the frequency domain (similar to Fig. 4.4 in Chapter 4) for spicule (SP1). Left panel (top-bottom) shows the spectral-peaks at 77 sec (primary) and 25.6 sec (secondary) for transverse, cross-sectional width and intensity parameter, marked with vertical lines. The azimuthal shear/torsion shows peak (38.4 sec) where the other parameters shows deficit in estimated power. This behaviour is discussed in detail in Chapter 4. Middle panel shows the temporal evolution of the visible apex of the spicule, with its spectral analysis (frequency) shown in the right panel, with averaged-PSD peaks at 25 sec and 100 sec. The magnitudes of the power for spectral peaks associated with the longitudinal motions shows a reverse trend as that from other estimated parameters (transverse, cross-sectional width and intensity).

6.3.2 Multi-threaded structure of chromospheric waveguides

Observations for both off-limb (spicule) and on-disk (mottle) structures show asymmetric spectra with multiple peaks in spectroscopic measurements, which are considered as the consequence of multi-threaded structures (Fig. 6.3) in chromospheric features (Dara et al., 1998; Ebadi, 2013; Skogsrud et al., 2014; Suematsu et al., 2008; Tanaka, 1974). Various mechanisms for the observed behavior were proposed, that included

the role of the line-of-sight (LOS) superposition effects (Skogsrud et al., 2014; Suematsu et al., 2008), strand-like structures due to the generation of Kelvin-Helmholtz vortices (Antolin et al., 2014), *pulse*-like origin (Ebadi, 2013). Also, Shelyag et al. (2011) showed that the vorticity, as observed in the solar photosphere, is generated by granular flows and intergranular magnetic elements. This vorticity, when injected at the foot-points of the magnetic flux tubes, can propagate up in the atmosphere though the tube structure, resulting in torsional and cross-sectional variations in the waveguide (Kitiashvili et al., 2013). These processes can deform the flux tube structure, which might appear as double/multiple stranded in the observations.

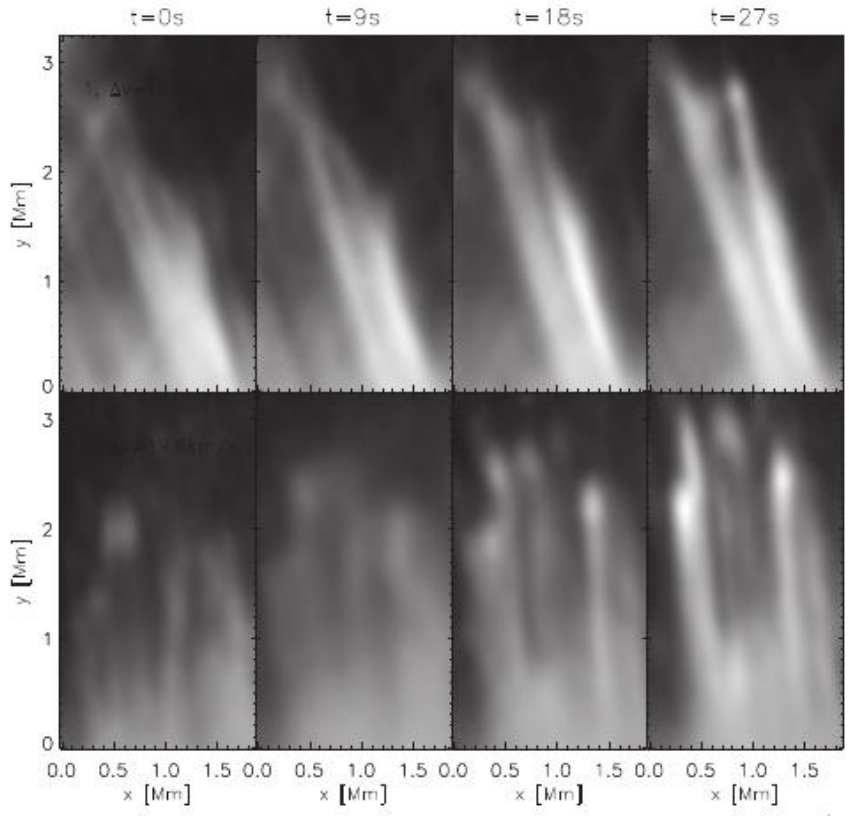

Fig. 6.3 Image taken from Skogsrud et al. (2014), shows two samples (top-bottom), with the spicule structures in Hα wavelength. The temporal evolution of the observed spicule structures shows the multi-strand/threaded structure, as a consequence of a dense feature being splitting into individual strands/threads.

However, laboratory experiments also showcase the multi-stranded structures in plasma (Beurskens et al., 2001; Romero-Talamas et al., 2006), along with the *fragmenting/splitting* and *merging* of the magnetic flux tube structures. This behavior for solar flux tube structures was also theoretically studied and reported by Ryutova (1993, 2015). Furthermore, numerical analysis for the bulk nonlinear transverse motions in

solar thin magnetic flux tubes also indicated the fragmentation of the structures as a consequence of strong/nonlinear kink wave motions (e.g., Ziegler and Ulmschneider, 1997b). These mechanisms do require further observational investigations, aided by numerical simulations, for a better understanding of one of the most fundamental observed properties of chromospheric magnetic flux tubes. The evolution of multi-stranded structures with height and time in multiple passbands is planned for an insight in this process in the solar chromosphere.

6.3.3 Kelvin-Helmholtz instabilities in spicular waveguides

Ubiquitous transverse and longitudinal motions are observed in spicules which reflect the confined MHD wave-behavior of these structures in the complex and inhomogeneous chromospheric atmosphere. These motions are coupled with the cross-sectional width variations and azimuthal shear/torsion of the flux tube structure (Chapter 4). The complex (nonlinear) dynamics of these waveguides further amplify the dissipation process, (see e.g., Goossens et al., 1992; Hollweg et al., 1990; Ionson, 1978). Theoretically, it is postulated that, the bulk transverse motions in the waveguide, due to confined kink wave-mode ($m = 1$), there is a transfer of energy, from transverse motions to the local torsional motions (similar to $m = 0$ torsional Alfvén wave mode) around the tube boundary (Verth et al., 2010). These azimuthal torsional motions can amplify with time and result into Kelvin-Helmholtz instability (Soler et al., 2010), which enhances the dissipation of energy from bulk motion to localized heating. This mechanism is numerically studied by Antolin et al. (2015, 2014) for the flux tube structures in both coronal and chromospheric ambient surroundings. However, most of the previous studies only included the bulk transverse motions of the spicular waveguides, whereas, the spicule motion comprises of transverse, cross-sectional width variations and longitudinal flows. Under the influence of these complex motions, the velocity shear between the spicule and the ambient chromospheric plasma would be more complicated, than previously assumed. Moreover, the observational limitations and analysis of separate POS and LOS motions have hampered the observational evidence of such dissipations in chromospheric environment.

The newly developed technique to estimate the resultant 3D velocity vectors at the pixel-scales, by combining the POS and LOS velocity estimates (Chapter 3), could be advantageous in detection and study of these fine-scale plasma instabilities. Figure 6.4, shows the presence of eddy-like structures near spicule surface. Eddies at flux tube surface are expected due to the velocity shear, in the form of Kelvin-Helmholtz instabilities. It is planned to analyze the multi-wavelength off-limb data to locate, track

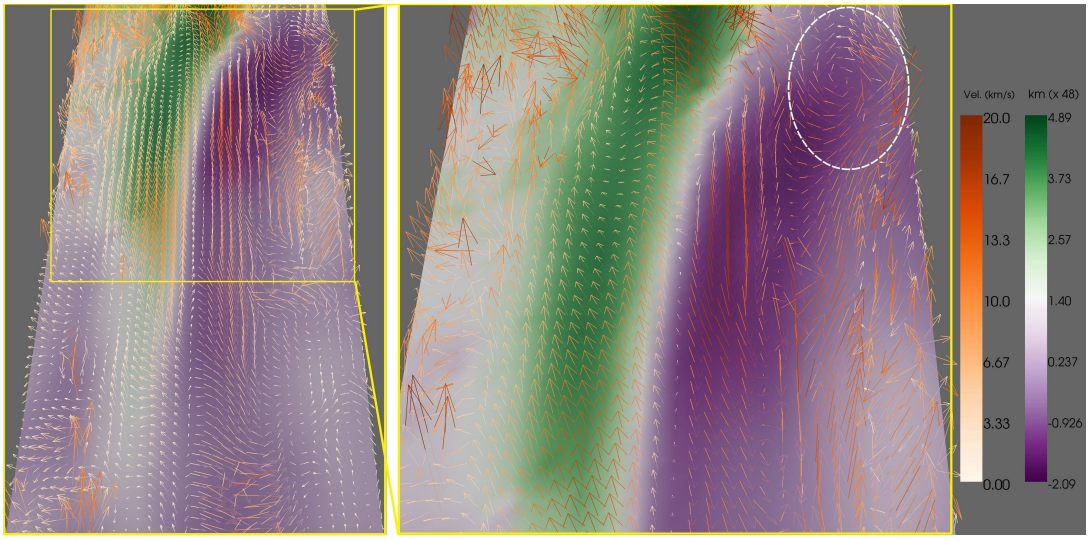

Fig. 6.4 Visualizations showing the reconstructed resultant velocity vectors, projected over a 2D-surface, color-coded in proportion to the magnitude of the resultant velocities. The background surface shows the LOS displacement of the analyzed spicule structure (SP5 in Chapter 3). Zoomed visualizations (yellow-box) inside and outside of the observed flux tube shows '*eddies*', formed due to the complex spicule motion. Example of such an eddie is highlighted by white-oval, indicating small-scale instabilities due to velocity shear between spicular and ambient plasma environment.

these shear flows around spicule structures. Techniques for automated detection and analysis for on-disk flows (vortex) were recently developed and tested (Giagkiozis et al., 2017). Also, the properties, such as lifetimes, boundaries (area), velocities, of such small-scale motions is foreseen using an approach developed by Graftieaux et al. (2001). A major outcome of this planned research will not only help in understanding the dissipation mechanisms in the chromosphere, but also, the crucial relationship between spicule and ambient plasma environment.

6.3.4 The flaring-arch filament (FAF) systems

The solar interface region is permeated by magnetic structures, in both open and closed field configurations. Several small-scale closed magnetic structures or low-lying loops have been observed and reported as, arch-filament systems (AFS), unresolved fine structure (UFS), intranetwork loops, flaring-arch filaments (FAFs) (Bruzek, 1967; Dowdy, 1993; Feldman, 1987; Vissers et al., 2015), from both ground- and space-based platforms. Furthermore, these low-lying loop structures were also associated with coronal jet eruptions (Moore et al., 2010; Sterling et al., 2015) and as sites of episodic heating (Hansteen et al., 2014). Recent multi-wavelength observations using IRIS

spacecraft by Hansteen et al. (2014) showed high Doppler velocity excursions at the foot-points of the AFS/UFS/FAF, with magnitudes up to 70-80 km/s, which is around 2-3 times higher than the acoustic velocities in plasma at chromospheric temperatures (80-100 $\times$ 10^4 K). The exact nature of the underlying physical mechanisms responsible for such high velocity excursions at the 'legs' of these structures is yet not fully understood.

Figure 6.5 shows an example of FAF structure observed at the limb in Hα imaging-spectroscopy data (Chapter 2), from the CRISP/SST instrument. The temporal evolution at different line-scan positions, shows the structure appearing both in closed loop and arch-like configurations, with apex-height at 2 Mm. A high velocity red-shifted jet structure is visible with velocities up to 60 km/s. The brightening at one of the legs of the FAF system, along with the corresponding Doppler estimates indicate possible plasma upflows, which might be due to magnetic reconnection (Ellerman-bomb) event at one of the foot-points (Reid et al., 2015). The foot-points of these structures are rooted into the intergranular lanes and can experience flux-emergence and buffetting phenomenon. However, these mechanisms indeed need to be investigated for FAF systems and for their possible role in high-velocity plasma flows and jet-triggering behaviour. The related future work-plan will focus on analysis of this and similar events in multiple wavelength observations from ground- (CRISP/SST) and space-(IRIS) based data.

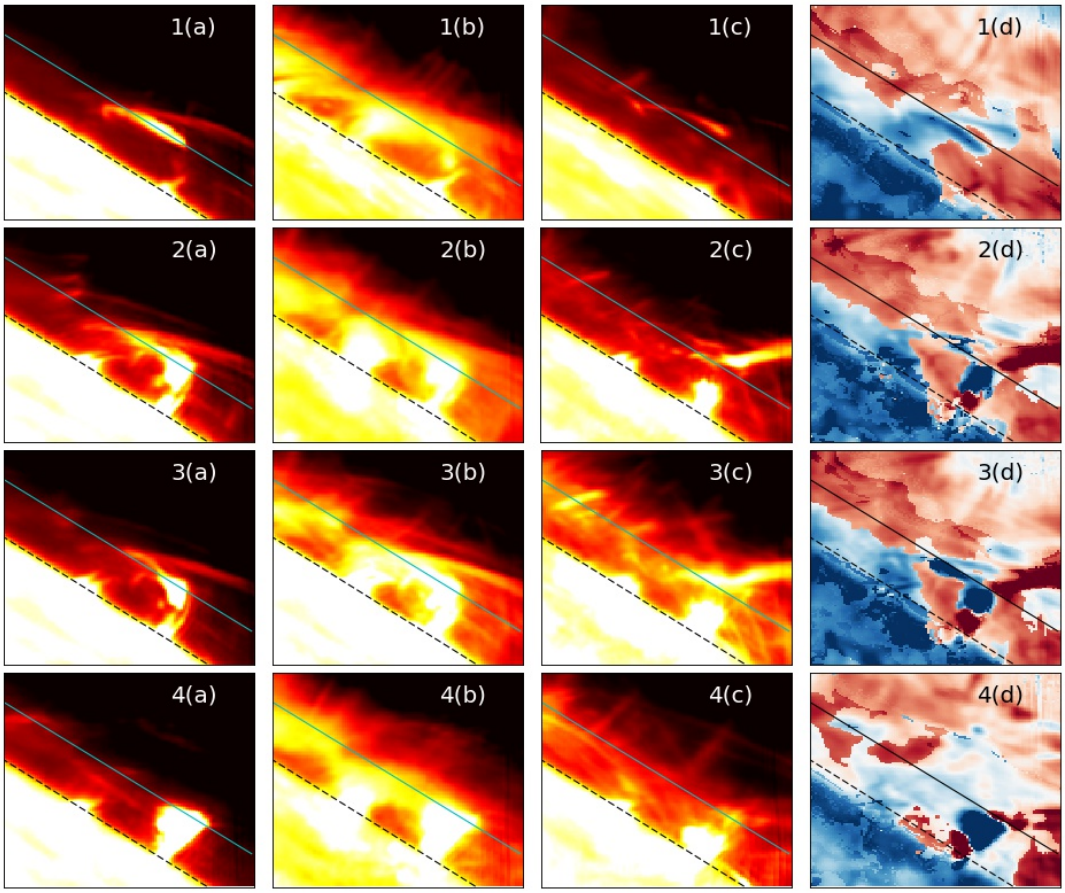

Fig. 6.5 A mosaic showcasing the evolution of a flaring-arch filament (FAF) structure and the associated jet, at the solar off-limb location, observed in the Hα spectral line. The images (1-4) correspond to the evolution of the FAF structure over time (25.9, 28.7, 30.2, 33.1 minutes), while (a-c) indicates the different line-scan positions (-1.290, -0.946, 1.032 Å from the line-core), along with the Doppler estimates scaled between $\pm$35 km/s. The blue-line, in the intensity images, marks the height at 2 Mm from the visible limb position (shown by the dashed-line). During different phases of the evolution, the structure shows both loop-like and arch-like profiles at various line-scan positions, along with strong Doppler shifts at one of the legs of the feature.

References

Abbasvand, V., Ebadi, H., and Fazel, Z. (2015). Seismology of solar spicules based on Hinode/SOT observations. *ArXiv e-prints*.

Alfvén, H. (1941). On the solar corona. *Arkiv for Matematik, Astronomi, och Fysik (Band 27A)*.

Antolin, P., Okamoto, T. J., De Pontieu, B., Uitenbroek, H., Van Doorsselaere, T., and Yokoyama, T. (2015). Resonant Absorption of Transverse Oscillations and Associated Heating in a Solar Prominence. II. Numerical Aspects. *ApJ*, 809:72.

Antolin, P., Yokoyama, T., and Van Doorsselaere, T. (2014). Fine Strand-like Structure in the Solar Corona from Magnetohydrodynamic Transverse Oscillations. *ApJL*, 787:L22.

Arregui, I. (2015). Wave heating of the solar atmosphere. *Philosophical Transactions of the Royal Society of London Series A*, 373:20140261–20140261.

Aschwanden, M. J., Winebarger, A., Tsiklauri, D., and Peter, H. (2007). The Coronal Heating Paradox. *ApJ*, 659:1673–1681.

Athay, R. G. and Bessey, R. J. (1964). Doppler Shifts and Line Broadening in Spicules. *ApJ*, 140:1174.

Avery, L. W. (1970). The formation of the Ca ii K line in a spinning spicule. *SolPhys*, 13:301–311.

Avrett, E. H. and Loeser, R. (2008). Models of the Solar Chromosphere and Transition Region from SUMER and HRTS Observations: Formation of the Extreme-Ultraviolet Spectrum of Hydrogen, Carbon, and Oxygen. *ApJS*, 175:229–276.

Beckers, J. M. (1968). Solar Spicules (Invited Review Paper). *SolPhys*, 3:367–433.

Beckers, J. M. (1972). Solar Spicules. *Annu. Rev. Astro. Astrophys.*, 10:73.

Beckers, J. M., Noyes, R. W., and Pasachoff, J. M. (1966). New Observations of Solar Chromospheric Spicules. *Astronomical Journal*, 71:155–156.

Beurskens, M. N. A., Cardozo, N. J. L., Arends, E. R., Barth, C. J., and van der Meiden, H. J. (2001). Filamentation in the rtp tokamak plasma. *Plasma Physics and Controlled Fusion*, 43(1):13.

Bhavilai, R. (1965). The structure of the solar chromosphere, I: Identification of spicules on the disk. *MNRAS*, 130:411.

Braithwaite, J. (2006). The stability of toroidal fields in stars. *A&A*, 453:687–698.

Bratsolis, E., Dialetis, D., and Alissandrakis, C. E. (1993). A new determination of the mean lifetime of bright and dark chromospheric mottles. *A&A*, 274:940.

Brault, J. and Neckel, H. (1987). Spectral Atlas of Solar Absolute Disk-averaged and Disk-Center Intensity from 3290 to 12510 Å.

Bray, R. J. and Loughhead, R. E. (1974). *The Solar Chromosphere*.

Bruzek, A. (1967). On Arch-Filament Systems in Spotgroups. *SolPhys*, 2:451–461.

Cao, W., Gorceix, N., Coulter, R., Ahn, K., Rimmele, T. R., and Goode, P. R. (2010). Scientific instrumentation for the 1.6 m New Solar Telescope in Big Bear. *Astronomische Nachrichten*, 331:636.

Cargill, P. J. and Klimchuk, J. A. (2004). Nanoflare Heating of the Corona Revisited. *ApJ*, 605:911–920.

Carlsson, M. (2007). Modeling the Solar Chromosphere. In Heinzel, P., Dorotovič, I., and Rutten, R. J., editors, *The Physics of Chromospheric Plasmas*, volume 368 of *Astronomical Society of the Pacific Conference Series*, page Heinzel.

Cavallini, F. and IBIS Team (2004). IBIS: Instrument Description and First Results. In *American Astronomical Society Meeting Abstracts #204*, volume 36 of *Bulletin of the American Astronomical Society*, page 710.

Cirtain, J. W., Golub, L., Winebarger, A. R., de Pontieu, B., Kobayashi, K., Moore, R. L., Walsh, R. W., Korreck, K. E., Weber, M., McCauley, P., Title, A., Kuzin, S., and Deforest, C. E. (2013). Energy release in the solar corona from spatially resolved magnetic braids. *Nature*, 493:501–503.

Cram, L. E. and Wilson, P. R. (1975). Hydromagnetic waves in structured magnetic fields. *SolPhys*, 41:313–327.

Dara, H. C., Koutchmy, S., and Suematsu, Y. (1998). Properties of Hα spicules from disk and limb high-resolution observations. In Guyenne, T.-D., editor, *Solar Jets and Coronal Plumes*, volume 421 of *ESA Special Publication*, page 255.

de la Cruz Rodríguez, J., Löfdahl, M. G., Sütterlin, P., Hillberg, T., and Rouppe van der Voort, L. (2015). CRISPRED: A data pipeline for the CRISP imaging spectropolarimeter. *A&A*, 573:A40.

De Pontieu, B., Carlsson, M., Rouppe van der Voort, L. H. M., Rutten, R. J., Hansteen, V. H., and Watanabe, H. (2012). Ubiquitous Torsional Motions in Type II Spicules. *ApJL*, 752:L12.

De Pontieu, B., Erdélyi, R., and de Wijn, A. G. (2003a). Intensity Oscillations in the Upper Transition Region above Active Region Plage. *ApJl*, 595:L63–L66.

De Pontieu, B., Erdélyi, R., and James, S. P. (2004). Solar chromospheric spicules from the leakage of photospheric oscillations and flows. *Nature*, 430:536–539.

De Pontieu, B., Hansteen, V. H., Rouppe van der Voort, L., van Noort, M., and Carlsson, M. (2007a). High-Resolution Observations and Modeling of Dynamic Fibrils. *ApJ*, 655:624–641.

De Pontieu, B., Hansteen, V. H., Rouppe van der Voort, L., van Noort, M., and Carlsson, M. (2007b). Observations and Simulations of Fibrils and Mottles. *ArXiv Astrophysics e-prints*.

De Pontieu, B., McIntosh, S., Hansteen, V. H., Carlsson, M., Schrijver, C. J., Tarbell, T. D., Title, A. M., Shine, R. A., Suematsu, Y., Tsuneta, S., Katsukawa, Y., Ichimoto, K., Shimizu, T., and Nagata, S. (2007c). A Tale of Two Spicules: The Impact of Spicules on the Magnetic Chromosphere. *PASJ*, 59:S655–S662.

De Pontieu, B., McIntosh, S. W., Carlsson, M., Hansteen, V. H., Tarbell, T. D., Schrijver, C. J., Title, A. M., Shine, R. A., Tsuneta, S., Katsukawa, Y., Ichimoto, K., Suematsu, Y., Shimizu, T., and Nagata, S. (2007d). Chromospheric Alfvénic Waves Strong Enough to Power the Solar Wind. *Science*, 318:1574.

De Pontieu, B., Tarbell, T., and Erdélyi, R. (2003b). Correlations on Arcsecond Scales between Chromospheric and Transition Region Emission in Active Regions. *ApJ*, 590:502–518.

De Pontieu, B., Title, A. M., Lemen, J. R., Kushner, G. D., Akin, D. J., Allard, B., Berger, T., Boerner, P., Cheung, M., Chou, C., Drake, J. F., Duncan, D. W., Freeland, S., Heyman, G. F., Hoffman, C., Hurlburt, N. E., Lindgren, R. W., Mathur, D., Rehse, R., Sabolish, D., Seguin, R., Schrijver, C. J., Tarbell, T. D., Wülser, J.-P., Wolfson, C. J., Yanari, C., Mudge, J., Nguyen-Phuc, N., Timmons, R., van Bezooijen, R., Weingrod, I., Brookner, R., Butcher, G., Dougherty, B., Eder, J., Knagenhjelm, V., Larsen, S., Mansir, D., Phan, L., Boyle, P., Cheimets, P. N., DeLuca, E. E., Golub, L., Gates, R., Hertz, E., McKillop, S., Park, S., Perry, T., Podgorski, W. A., Reeves, K., Saar, S., Testa, P., Tian, H., Weber, M., Dunn, C., Eccles, S., Jaeggli, S. A., Kankelborg, C. C., Mashburn, K., Pust, N., Springer, L., Carvalho, R., Kleint, L., Marmie, J., Mazmanian, E., Pereira, T. M. D., Sawyer, S., Strong, J., Worden, S. P., Carlsson, M., Hansteen, V. H., Leenaarts, J., Wiesmann, M., Aloise, J., Chu, K.-C., Bush, R. I., Scherrer, P. H., Brekke, P., Martinez-Sykora, J., Lites, B. W., McIntosh, S. W., Uitenbroek, H., Okamoto, T. J., Gummin, M. A., Auker, G., Jerram, P., Pool, P., and Waltham, N. (2014). The Interface Region Imaging Spectrograph (IRIS). *SolPhys*, 289:2733–2779.

Defouw, R. J. (1976). Wave propagation along a magnetic tube. *ApJ*, 209:266–269.

Dere, K. P., Bartoe, J.-D. F., and Brueckner, G. E. (1989). Explosive events in the solar transition zone. *SolPhys*, 123:41–68.

Deubner, F.-L. (1974). Some properties of velocity fields in the solar photosphere. V - Spatio-temporal analysis of high resolution spectra. *SolPhys*, 39:31–48.

Domingo, V., Fleck, B., and Poland, A. I. (1995). The SOHO Mission: an Overview. *SolPhys*, 162:1–37.

Dowdy, Jr., J. F. (1993). Observational evidence for hotter transition region loops within the supergranular network. *ApJ*, 411:406–409.

Ebadi, H. (2013). Evidences to the pulse like origin of double spicules based on Hinode/SOT observations. *Ap&SS*, 348:11–15.

Ebadi, H. and Ghiassi, M. (2014). Observation of kink waves and their reconnection-like origin in solar spicules. *Ap&SS*, 353:31–36.

Ebadi, H. and Khoshrangbaf, M. (2014). Observation of the period ratio P_1/P_2 of transversal oscillations in solar macro-spicules. *Ap&SS*, 352:353–359.

Ebadi, H., Zaqarashvili, T. V., and Zhelyazkov, I. (2012). Observation of standing kink waves in solar spicules. *Ap&SS*, 337:33–37.

Edlén, B. (1943). Die Deutung der Emissionslinien im Spektrum der Sonnenkorona. Mit 6 Abbildungen. *ZAP*, 22:30.

Edwin, P. M. and Roberts, B. (1983). Wave propagation in a magnetic cylinder. *SolPhys*, 88:179–191.

Emslie, A. G. and Noyes, R. W. (1978). The characteristics of impulsive solar EUV bursts. *SolPhys*, 57:373–383.

Erdélyi, R. (2004). Coronal heating: Heating in the solar atmosphere. *Astronomy and Geophysics*, 45(4):4.34–4.37.

Erdélyi, R. and Fedun, V. (2007). Are There Alfvén Waves in the Solar Atmosphere? *Science*, 318:1572.

Erdélyi, R. and Taroyan, Y. (2008). Hinode EUV spectroscopic observations of coronal oscillations. *A&A*, 489:L49–L52.

Feldman, U. (1987). On the unresolved fine structures of the solar atmosphere. II - The temperature region 200,000 - 500,000 K. *ApJ*, 320:426–429.

Fisher, G. H. and Welsch, B. (2007). FLCT: A Fast, Efficient Method for Performing Local Correlation Tracking. In *American Astronomical Society Meeting Abstracts #210*, volume 39 of *Bulletin of the American Astronomical Society*, page 210.

Fisher, G. H. and Welsch, B. T. (2008). FLCT: A Fast, Efficient Method for Performing Local Correlation Tracking. In Howe, R., Komm, R. W., Balasubramaniam, K. S., and Petrie, G. J. D., editors, *Subsurface and Atmospheric Influences on Solar Activity*, volume 383 of *Astronomical Society of the Pacific Conference Series*, page 373.

Fossum, A. and Carlsson, M. (2005). High-frequency acoustic waves are not sufficient to heat the solar chromosphere. *Nature*, 435:919–921.

Foukal, P. (1971a). Hα Fine Structure and the Chromospheric Field. *SolPhys*, 20:298–309.

Foukal, P. (1971b). Morphological Relationships in the Chromospheric Hα Fine Structure. *SolPhys*, 19:59–71.

Freed, M. S., McKenzie, D. E., Longcope, D. W., and Wilburn, M. (2016). Analysis of Flows inside Quiescent Prominences as Captured by Hinode/Solar Optical Telescope. *ApJ*, 818:57.

Gadzhiev, T. G. and Nikolskii, G. M. (1982). Spicule Motions. *Soviet Astronomy Letters*, 8:341.

Gafeira, R., Jafarzadeh, S., Solanki, S. K., Lagg, A., van Noort, M., Barthol, P., Blanco Rodríguez, J., del Toro Iniesta, J. C., Gandorfer, A., Gizon, L., Hirzberger, J., Knölker, M., Orozco Suárez, D., Riethmüller, T. L., and Schmidt, W. (2017a). Oscillations on Width and Intensity of Slender Ca ii H Fibrils from Sunrise/SuFI. *ApJS*, 229:7.

Gafeira, R., Lagg, A., Solanki, S. K., Jafarzadeh, S., van Noort, M., Barthol, P., Blanco Rodríguez, J., del Toro Iniesta, J. C., Gandorfer, A., Gizon, L., Hirzberger, J., Knölker, M., Orozco Suárez, D., Riethmüller, T. L., and Schmidt, W. (2017b). Morphological Properties of Slender Ca ii H Fibrils Observed by Sunrise II. *ApJS*, 229:6.

Gary, G. A. (2001). Plasma Beta above a Solar Active Region: Rethinking the Paradigm. *SolPhys*, 203:71–86.

Gent, F. A., Fedun, V., Mumford, S. J., and Erdélyi, R. (2013). Magnetohydrostatic equilibrium - I. Three-dimensional open magnetic flux tube in the stratified solar atmosphere. *MNRAS*, 435:689–697.

Giagkiozis, I., Fedun, V., Erdélyi, R., and Verth, G. (2015). Axisymmetric Modes in Magnetic Flux Tubes with Internal and External Magnetic Twist. *ApJ*, 810:53.

Giagkiozis, I., Fedun, V., Scullion, E., and Verth, G. (2017). Vortex Flows in the Solar Atmoshpere: Automated Identification and Statistical Analysis. *ArXiv e-prints*.

Golub, L. and Pasachoff, J. M. (1997). *The Solar Corona*.

Goossens, M., Erdélyi, R., and Ruderman, M. S. (2011). Resonant MHD Waves in the Solar Atmosphere. *Space Science Reviews*, 158:289–338.

Goossens, M., Hollweg, J. V., and Sakurai, T. (1992). Resonant behaviour of MHD waves on magnetic flux tubes. III - Effect of equilibrium flow. *SolPhys*, 138:233–255.

Goossens, M., Soler, R., Terradas, J., Van Doorsselaere, T., and Verth, G. (2014). The Transverse and Rotational Motions of Magnetohydrodynamic Kink Waves in the Solar Atmosphere. *ApJ*, 788:9.

Goossens, M., Terradas, J., Andries, J., Arregui, I., and Ballester, J. L. (2009). On the nature of kink MHD waves in magnetic flux tubes. *A&A*, 503:213–223.

Graftieaux, L., Michard, M., and Grosjean, N. (2001). Combining PIV, POD and vortex identification algorithms for the study of unsteady turbulent swirling flows. *Measurement Science and Technology*, 12:1422–1429.

Grotrian, W. (1939). Zur Frage der Deutung der Linien im Spektrum der Sonnenkorona. *Naturwissenschaften*, 27:214–214.

Hansteen, V., De Pontieu, B., Carlsson, M., Lemen, J., Title, A., Boerner, P., Hurlburt, N., Tarbell, T. D., Wuelser, J. P., Pereira, T. M. D., De Luca, E. E., Golub, L., McKillop, S., Reeves, K., Saar, S., Testa, P., Tian, H., Kankelborg, C., Jaeggli, S., Kleint, L., and Martínez-Sykora, J. (2014). The unresolved fine structure resolved: IRIS observations of the solar transition region. *Science*, 346:1255757.

Harrison, R. A. (1997). EUV Blinkers: The Significance of Variations in the Extreme Ultraviolet Quiet Sun. *SolPhys*, 175:467–485.

Hasan, S. and Keil, S. L. (1984). Time-resolved spectral observations of spicule velocities at several heights. *ApJL*, 283:L75–L77.

He, J., Marsch, E., Tu, C., and Tian, H. (2009). Excitation of Kink Waves Due to Small-Scale Magnetic Reconnection in the Chromosphere? *ApJL*, 705:L217–L222.

Heyvaerts, J. and Priest, E. R. (1983). Coronal heating by phase-mixed shear Alfven waves. *A&A*, 117:220–234.

Hollweg, J. V. and Roberts, B. (1981). Bound oscillations on thin magnetic flux tubes - Convective instability and umbral oscillations. *ApJ*, 250:398–407.

Hollweg, J. V., Yang, G., Cadez, V. M., and Gakovic, B. (1990). Surface waves in an incompressible fluid - Resonant instability due to velocity shear. *ApJ*, 349:335–344.

Ionson, J. A. (1978). Resonant absorption of Alfvenic surface waves and the heating of solar coronal loops. *ApJ*, 226:650–673.

Jafarzadeh, S., Solanki, S. K., Gafeira, R., van Noort, M., Barthol, P., Blanco Rodríguez, J., del Toro Iniesta, J. C., Gandorfer, A., Gizon, L., Hirzberger, J., Knölker, M., Orozco Suárez, D., Riethmüller, T. L., and Schmidt, W. (2017). Transverse Oscillations in Slender Ca ii H Fibrils Observed with Sunrise/SuFI. *ApJS*, 229:9.

James, S. P., Erdélyi, R., and De Pontieu, B. (2003). Can ion-neutral damping help to form spicules? *A&A*, 406:715–724.

Jess, D. B., Mathioudakis, M., Christian, D. J., Keenan, F. P., Ryans, R. S. I., and Crockett, P. J. (2010). ROSA: A High-cadence, Synchronized Multi-camera Solar Imaging System. *SolPhys*, 261:363–373.

Jess, D. B., Mathioudakis, M., Erdélyi, R., Crockett, P. J., Keenan, F. P., and Christian, D. J. (2009). Alfvén Waves in the Lower Solar Atmosphere. *Science*, 323:1582.

Jess, D. B., Morton, R. J., Verth, G., Fedun, V., Grant, S. D. T., and Giagkiozis, I. (2015). Multiwavelength Studies of MHD Waves in the Solar Chromosphere. An Overview of Recent Results. *Space Science Review*, 190:103–161.

Jess, D. B., Pascoe, D. J., Christian, D. J., Mathioudakis, M., Keys, P. H., and Keenan, F. P. (2012). The Origin of Type I Spicule Oscillations. *ApJL*, 744:L5.

Jiang, L., Perlin, M., and Schultz, W. W. (1998). Period tripling and energy dissipation of breaking standing waves. *Journal of Fluid Mechanics*, 369.

Judge, P. G. and Carlsson, M. (2010). On the Solar Chromosphere Observed at the LIMB with Hinode. *ApJ*, 719:469–473.

Kalkofen, W. (1990). The heating of the quiet solar chromosphere. In Priest, E. R. and Krishan, V., editors, *Basic Plasma Processes on the Sun*, volume 142 of *IAU Symposium*, pages 197–204.

Kalkofen, W. (2007). Is the Solar Chromosphere Heated by Acoustic Waves? *ApJ*, 671:2154–2158.

Kano, R., Bando, T., Narukage, N., Ishikawa, R., Tsuneta, S., Katsukawa, Y., Kubo, M., Ishikawa, S.-n., Hara, H., Shimizu, T., Suematsu, Y., Ichimoto, K., Sakao, T., Goto, M., Kato, Y., Imada, S., Kobayashi, K., Holloway, T., Winebarger, A., Cirtain, J., De Pontieu, B., Casini, R., Trujillo Bueno, J., Štepán, J., Manso Sainz, R., Belluzzi, L., Asensio Ramos, A., Auchère, F., and Carlsson, M. (2012). Chromospheric Lyman-alpha spectro-polarimeter (CLASP). In *Space Telescopes and Instrumentation 2012: Ultraviolet to Gamma Ray*, volume 8443 of , page 84434F.

Khomenko, E. and Collados, M. (2012). Heating of the Magnetized Solar Chromosphere by Partial Ionization Effects. *ApJ*, 747:87.

Khutsishvili, D.and Zaqarashvili, T. V. K. E., Kvernadze, T., Kulidzanishvili, V., Kakhiani, V., and Sikharulidze, M. (2017). Anti-phase oscillations of hα line doppler velocity and width in solar limb spicules. *Astrophysics and Space Science*, 362(12):235.

Kilcik, A., Özgüç, A., Rozelot, J. P., and Ataç, T. (2010). Periodicities in Solar Flare Index for Cycles 21 - 23 Revisited. *SolPhys*, 264:255–268.

Kim, Y.-H., Bong, S.-C., Park, Y.-D., Cho, K.-S., Moon, Y.-J., and Suematsu, Y. (2008). Estimation of Spicule Magnetic Field Using Observed MHD Waves by the Hinode SOT. *Journal of Korean Astronomical Society*, 41:173–180.

Kitiashvili, I. N., Kosovichev, A. G., Lele, S. K., Mansour, N. N., and Wray, A. A. (2013). Ubiquitous Solar Eruptions Driven by Magnetized Vortex Tubes. *ApJ*, 770:37.

Komm, R. W., Anderson, E., Hill, F., Howe, R., Fodor, I., and Stark, P. (1998). Multitaper Analysis Applied to a 3-month Time Series. In Korzennik, S., editor, *Structure and Dynamics of the Interior of the Sun and Sun-like Stars*, volume 418 of *ESA Special Publication*, page 257.

Kosugi, T., Matsuzaki, K., Sakao, T., Shimizu, T., Sone, Y., Tachikawa, S., Hashimoto, T., Minesugi, K., Ohnishi, A., Yamada, T., Tsuneta, S., Hara, H., Ichimoto, K., Suematsu, Y., Shimojo, M., Watanabe, T., Shimada, S., Davis, J. M., Hill, L. D., Owens, J. K., Title, A. M., Culhane, J. L., Harra, L. K., Doschek, G. A., and Golub, L. (2007). The Hinode (Solar-B) Mission: An Overview. *SolPhys*, 243:3–17.

Kukhianidze, V., Zaqarashvili, T. V., and Khutsishvili, E. (2006). Observation of kink waves in solar spicules. *A&A*, 449:L35–L38.

Kulidzanishvili, V. I. and Nikolskii, G. M. (1978). Properties of the solar chromosphere H-alpha spicules as observed spectrally. *SolPhys*, 59:21–28.

Kulidzanishvili, V. I. and Zhugzhda, I. D. (1983). On the problem of spicular oscillations. *SolPhys*, 88:35–41.

Kuperus, M. (1969). The Heating of the Solar Corona. *Space Science Review*, 9:713–739.

Kuperus, M., Ionson, J. A., and Spicer, D. S. (1981). On the theory of coronal heating mechanisms. *Annu. Rev. Astro. Astrophys.*, 19:7–40.

Kuridze, D., Henriques, V., Mathioudakis, M., Erdélyi, R., Zaqarashvili, T. V., Shelyag, S., Keys, P. H., and Keenan, F. P. (2015). The Dynamics of Rapid Redshifted and Blueshifted Excursions in the Solar Hα Line. *ApJ*, 802:26.

Kuridze, D., Morton, R. J., Erdélyi, R., Dorrian, G. D., Mathioudakis, M., Jess, D. B., and Keenan, F. P. (2012). Transverse Oscillations in Chromospheric Mottles. *ApJ*, 750:51.

Kuridze, D., Verth, G., Mathioudakis, M., Erdélyi, R., Jess, D. B., Morton, R. J., Christian, D. J., and Keenan, F. P. (2013). Characteristics of Transverse Waves in Chromospheric Mottles. *ApJ*, 779:82.

Kuźma, B., Murawski, K., Zaqarashvili, T. V., Konkol, P., and Mignone, A. (2017). Numerical simulations of solar spicules: Adiabatic and non-adiabatic studies. *A&A*, 597:A133.

Langangen, Ø., De Pontieu, B., Carlsson, M., Hansteen, V. H., Cauzzi, G., and Reardon, K. (2008). Search for High Velocities in the Disk Counterpart of Type II Spicules. *ApJL*, 679:L167.

Leake, J. E., Arber, T. D., and Khodachenko, M. L. (2005). Collisional dissipation of Alfvén waves in a partially ionised solar chromosphere. *A&A*, 442:1091–1098.

Leenaarts, J., Carlsson, M., Hansteen, V., and Rutten, R. J. (2007). Non-equilibrium hydrogen ionization in 2D simulations of the solar atmosphere. *A&A*, 473:625–632.

Leenaarts, J., Carlsson, M., and Rouppe van der Voort, L. (2012). The Formation of the Hα Line in the Solar Chromosphere. *ApJ*, 749:136.

Leighton, R. B., Noyes, R. W., and Simon, G. W. (1962). Velocity Fields in the Solar Atmosphere. I. Preliminary Report. *ApJ*, 135:474.

Linsay, P. S. (1981). Period doubling and chaotic behavior in a driven anharmonic oscillator. *Phys. Rev. Lett.*, 47:1349–1352.

Lippincott, S. L. (1957). Chromospheric Spicules. *Smithsonian Contributions to Astrophysics*, 2:15.

Lites, B. W., Shine, R. A., and Chipman, E. G. (1978). Line formation in the solar chromosphere. I - The C II resonance lines observed with OSO 8. *ApJ*, 222:333–341.

López Ariste, A. and Casini, R. (2005). Inference of the magnetic field in spicules from spectropolarimetry of He I D3. *A&A*, 436:325–331.

Loughhead, R. E. (1974). High-Resolution Photography of the Solar Chromosphere. XII: An Attempt to Measure Vertical Velocities of Hα Bright Mottles beyond Limb. *SolPhys*, 35:55–61.

Magyar, N. and Van Doorsselaere, T. (2016). Damping of nonlinear standing kink oscillations: a numerical study. *A&A*, 595:A81.

Mariska, J. T. (1986). The quiet solar transition region. *Annu. Rev. Astro. Astrophys.*, 24:23–48.

Martinez-Sykora, J., De Pontieu, B., Hansteen, V. H., Rouppe van der Voort, L., Carlsson, M., and Pereira, T. M. D. (2017). On the generation of solar spicules and alfvénic waves. *Science*, 356(6344):1269–1272.

Michard, R. (1954). Radial velocities of spicules and the width of chromospheric lines. *The Observatory*, 74:209–209.

Michard, R. (1956). Spectrophotométrie des raies d'émission intenses de la chromosphère. *Annales d'Astrophysique*, 19:1.

Moore, R. L., Cirtain, J. W., Sterling, A. C., and Falconer, D. A. (2010). Dichotomy of Solar Coronal Jets: Standard Jets and Blowout Jets. *ApJ*, 720:757–770.

Mooroogen, K., Morton, R. J., and Henriques, V. (2017). Dynamics of internetwork chromospheric fibrils: Basic properties and magnetohydrodynamic kink waves. *A&A*, 607:A46.

Morton, R. J. (2014). Magneto-seismological insights into the penumbral chromosphere and evidence for wave damping in spicules. *A&A*, 566:A90.

Morton, R. J., Verth, G., Fedun, V., Shelyag, S., and Erdélyi, R. (2013). Evidence for the Photospheric Excitation of Incompressible Chromospheric Waves. *ApJ*, 768:17.

Morton, R. J., Verth, G., Hillier, A., and Erdélyi, R. (2014). The Generation and Damping of Propagating MHD Kink Waves in the Solar Atmosphere. *ApJ*, 784:29.

Morton, R. J., Verth, G., Jess, D. B., Kuridze, D., Ruderman, M. S., Mathioudakis, M., and Erdélyi, R. (2012a). Observations of ubiquitous compressive waves in the Sun's chromosphere. *Nature Communications*, 3:1315.

Morton, R. J., Verth, G., McLaughlin, J. A., and Erdélyi, R. (2012b). Determination of Sub-resolution Structure of a Jet by Solar Magnetoseismology. *ApJ*, 744:5.

Mouradian, Z. (1967). La diffusion des spicules dans la couronne solaire. *SolPhys*, 2:258–266.

Mufti, S. and Shah, G. N. (2011). Solar-geomagnetic activity influence on Earth's climate. *Journal of Atmospheric and Solar-Terrestrial Physics*, 73:1607–1615.

Narain, U. and Ulmschneider, P. (1990). Chromospheric and coronal heating mechanisms. *Space Science Review*, 54:377–445.

Narain, U. and Ulmschneider, P. (1996). Chromospheric and Coronal Heating Mechanisms II. *Space Science Review*, 75:453–509.

Nikol'skii, G. M. and Sazanov, A. A. (1966). The Motion and Nature of Hα Spicules in the Solar Chromosphere. *AZH*, 43:928.

Nikolsky, G. M. and Platova, A. G. (1971). Motions of Hα-spicules along the solar limb. *SolPhys*, 18:403–409.

November, L. J. and Simon, G. W. (1988). Precise proper-motion measurement of solar granulation. *ApJ*, 333:427–442.

Okamoto, T. J., Antolin, P., De Pontieu, B., Uitenbroek, H., Van Doorsselaere, T., and Yokoyama, T. (2015). Resonant Absorption of Transverse Oscillations and Associated Heating in a Solar Prominence. I. Observational Aspects. *ApJ*, 809:71.

Okamoto, T. J. and De Pontieu, B. (2011). Propagating Waves Along Spicules. *ApJL*, 736:L24.

Osterbrock, D. E. (1961). The Heating of the Solar Chromosphere, Plages, and Corona by Magnetohydrodynamic Waves. *ApJ*, 134:347.

Papushev, P. G. and Salakhutdinov, R. T. (1994). The dynamics of chromospheric spicules. *Space Science Review*, 70:47–51.

Parker, E. N. (1957). Acceleration of Cosmic Rays in Solar Flares. *Physical Review*, 107:830–836.

Parker, E. N. (1974a). Hydraulic Concentration of Magnetic Fields in the Solar Photosphere. I. Turbulent Pumping. *ApJ*, 189:563–568.

Parker, E. N. (1974b). Hydraulic Concentration of Magnetic Fields in the Solar Photosphere. II. Bernoulli Effect. *ApJ*, 190:429–436.

Pasachoff, J. M., Noyes, R. W., and Beckers, J. M. (1968). Spectral Observations of Spicules at Two Heights in the Solar Chromosphere. *SolPhys*, 5:131–158.

Percival, D. B. and Walden, A. T. (1993). *Spectral Analysis for Physical Applications*. Cambridge University Press.

Pereira, T. M. D., De Pontieu, B., and Carlsson, M. (2012). Quantifying Spicules. *ApJ*, 759:18.

Pereira, T. M. D., De Pontieu, B., Carlsson, M., Hansteen, V., Tarbell, T. D., Lemen, J., Title, A., Boerner, P., Hurlburt, N., Wülser, J. P., Martínez-Sykora, J., Kleint, L., Golub, L., McKillop, S., Reeves, K. K., Saar, S., Testa, P., Tian, H., Jaeggli, S., and Kankelborg, C. (2014). An Interface Region Imaging Spectrograph First View on Solar Spicules. *ApJL*, 792:L15.

Pesnell, W. D., Thompson, B. J., and Chamberlin, P. C. (2012). The Solar Dynamics Observatory (SDO). *SolPhys*, 275:3–15.

Peter, H., Tian, H., Curdt, W., Schmit, D., Innes, D., De Pontieu, B., Lemen, J., Title, A., Boerner, P., Hurlburt, N., Tarbell, T. D., Wuelser, J. P., Martínez-Sykora, J., Kleint, L., Golub, L., McKillop, S., Reeves, K. K., Saar, S., Testa, P., Kankelborg, C., Jaeggli, S., Carlsson, M., and Hansteen, V. (2014). Hot explosions in the cool atmosphere of the Sun. *Science*, 346:1255726.

Pietarila, A., Aznar Cuadrado, R., Hirzberger, J., and Solanki, S. K. (2011). Kink Waves in an Active Region Dynamic Fibril. *ApJ*, 739:92.

Prestes, A., Rigozo, N. R., Echer, E., and Vieira, L. E. A. (2006). Spectral analysis of sunspot number and geomagnetic indices (1868 2001). *Journal of Atmospheric and Solar-Terrestrial Physics*, 68:182–190.

Pucci, S., Poletto, G., Sterling, A. C., and Romoli, M. (2013). Physical Parameters of Standard and Blowout Jets. *ApJ*, 776:16.

Raouafi, N. E., Patsourakos, S., Pariat, E., Young, P. R., Sterling, A. C., Savcheva, A., Shimojo, M., Moreno-Insertis, F., DeVore, C. R., Archontis, V., Török, T., Mason, H., Curdt, W., Meyer, K., Dalmasse, K., and Matsui, Y. (2016). Solar Coronal Jets: Observations, Theory, and Modeling. *Space Science Review*, 201:1–53.

Reid, A., Mathioudakis, M., Scullion, E., Doyle, J. G., Shelyag, S., and Gallagher, P. (2015). Ellerman Bombs with Jets: Cause and Effect. *ApJ*, 805:64.

Roberts, B. and Webb, A. R. (1978). Vertical motions in an intense magnetic flux tube. *SolPhys*, 56:5–35.

Roberts, W. O. (1945). A Preliminary Report on Chromospheric Spicules of Extremely Short Lifetime. *ApJ*, 101:136.

Roberts, W. O., Brenton, V. K., Shapley, M. B., and Kopal, Z. (1949). Further Measures of Chromospheric Spicules. *PASP*, 61:160.

Romero-Talamas, C. A., Holcomb, C., Bellan, P. M., and Hill, D. N. (2006). Spheromak formation and sustainment studies at the sustained spheromak physics experiment using high-speed imaging and magnetic diagnostics. *Physics of Plasmas*, 13(2):022502.

Rouppe van der Voort, L., Leenaarts, J., de Pontieu, B., Carlsson, M., and Vissers, G. (2009). On-disk Counterparts of Type II Spicules in the Ca II 854.2 nm and Hα Lines. *ApJ*, 705:272–284.

Ruderman, M. S., Goossens, M., and Andries, J. (2010). Nonlinear propagating kink waves in thin magnetic tubes. *Physics of Plasmas*, 17(8):082108.

Rush, J. H. and Roberts, W. O. (1954). Recent Studies of Chromospheric Spicules. *Australian Journal of Physics*, 7:230.

Rutten, R. J. (2006). On the Nature of the Solar Chromosphere. In Leibacher, J., Stein, R. F., and Uitenbroek, H., editors, *Solar MHD Theory and Observations: A High Spatial Resolution Perspective*, volume 354 of *Astronomical Society of the Pacific Conference Series*, page 276.

Rutten, R. J. (2007). Observing the Solar Chromosphere. In Heinzel, P., Dorotovič, I., and Rutten, R. J., editors, *The Physics of Chromospheric Plasmas*, volume 368 of *Astronomical Society of the Pacific Conference Series*, page Heinzel.

Rutten, R. J. (2008). Hα as a Chromospheric Diagnostic. In Matthews, S. A., Davis, J. M., and Harra, L. K., editors, *First Results From Hinode*, volume 397 of *Astronomical Society of the Pacific Conference Series*, page 54.

Rutten, R. J., Vissers, G. J. M., Rouppe van der Voort, L. H. M., Sütterlin, P., and Vitas, N. (2013). Ellerman bombs: fallacies, fads, usage. In *Journal of Physics Conference Series*, volume 440 of *Journal of Physics Conference Series*, page 012007.

Ryutova, M. (1993). Generation of Plasma Flows and Filamentation of Magnetic Fields in Solar Atmosphere. In Zirin, H., Ai, G., and Wang, H., editors, *IAU Colloq. 141: The Magnetic and Velocity Fields of Solar Active Regions*, volume 46 of *Astronomical Society of the Pacific Conference Series*, page 549.

Ryutova, M. (2015). *Physics of Magnetic Flux Tubes*.

Saha, M. N. (1920). Liii. ionization in the solar chromosphere. *The London, Edinburgh, and Dublin Philosophical Magazine and Journal of Science*, 40(238):472–488.

Sawyer, C. (1972). Hα Mottles. *SolPhys*, 24:79–86.

Scharmer, G. B., Bjelksjo, K., Korhonen, T. K., Lindberg, B., and Petterson, B. (2003). The 1-meter Swedish solar telescope. In Keil, S. L. and Avakyan, S. V., editors, *Innovative Telescopes and Instrumentation for Solar Astrophysics*, volume 4853 of , pages 341–350.

Scharmer, G. B., Narayan, G., Hillberg, T., de la Cruz Rodriguez, J., Löfdahl, M. G., Kiselman, D., Sütterlin, P., van Noort, M., and Lagg, A. (2008). CRISP Spectropolarimetric Imaging of Penumbral Fine Structure. *ApJL*, 689:L69.

Scullion, E., Erdélyi, R., Fedun, V., and Doyle, J. G. (2011). The Response of A Three-dimensional Solar Atmosphere to Wave-driven Jets. *ApJ*, 743:14.

Secchi, A. (1877). *Le soleil: Texte. Seconde partie*. Number pt. 2. Gauthier-Villars.

Sekse, D. H., Rouppe van der Voort, L., and De Pontieu, B. (2012). Statistical Properties of the Disk Counterparts of Type II Spicules from Simultaneous Observations of Rapid Blueshifted Excursions in Ca II 8542 and Hα. *ApJ*, 752:108.

Sekse, D. H., Rouppe van der Voort, L., and De Pontieu, B. (2013a). On the Temporal Evolution of the Disk Counterpart of Type II Spicules in the Quiet Sun. *ApJ*, 764:164.

Sekse, D. H., Rouppe van der Voort, L., De Pontieu, B., and Scullion, E. (2013b). Interplay of Three Kinds of Motion in the Disk Counterpart of Type II Spicules: Upflow, Transversal, and Torsional Motions. *ApJ*, 769:44.

Sharma, R., Verth, G., and Erdélyi, R. (2017). Dynamic Behavior of Spicules Inferred from Perpendicular Velocity Components. *ApJ*, 840:96.

Shelyag, S., Fedun, V., and Erdélyi, R. (2008). Magnetohydrodynamic code for gravitationally-stratified media. *A&A*, 486:655–662.

Shelyag, S., Keys, P., Mathioudakis, M., and Keenan, F. P. (2011). Vorticity in the solar photosphere. *A&A*, 526:A5.

Shetye, J., Doyle, J. G., Scullion, E., Nelson, C. J., Kuridze, D., Henriques, V., Woeger, F., and Ray, T. (2016). High-cadence observations of spicular-type events on the Sun. *A&A*, 589:A3.

Shetye, J., Kuridze, D., Stangalini, M., Doyle, J. G., Scullion, E., Henriques, V., and Ray, T. (2017). High-frequency transverse oscillations and intensity perturbations in spicular-type events. *ArXiv e-prints*.

Shibata, K., Ishido, Y., Acton, L. W., Strong, K. T., Hirayama, T., Uchida, Y., McAllister, A. H., Matsumoto, R., Tsuneta, S., Shimizu, T., Hara, H., Sakurai, T., Ichimoto, K., Nishino, Y., and Ogawara, Y. (1992). Observations of X-ray jets with the YOHKOH Soft X-ray Telescope. *PASJ*, 44:L173–L179.

Shibata, K. and Suematsu, Y. (1982). Why are spicules absent over plages and long under coronal holes. *SolPhys*, 78:333–345.

Shimojo, M., Hashimoto, S., Shibata, K., Hirayama, T., Hudson, H. S., and Acton, L. W. (1996). Statistical Study of Solar X-Ray Jets Observed with the YOHKOH Soft X-Ray Telescope. *PASJ*, 48:123–136.

Shimojo, M. and Shibata, K. (2000). Physical Parameters of Solar X-Ray Jets. *ApJ*, 542:1100–1108.

Shklovskii, I. S. and Kononovich, E. V. (1958). Models of the Solar Chromosphere. *Soviet Astronomy*, 2:32.

Skogsrud, H., Rouppe van der Voort, L., and De Pontieu, B. (2014). On the Multithreaded Nature of Solar Spicules. *ApJL*, 795:L23.

Slepian, D. (1978). Prolate spheroidal wave functions, Fourier analysis, and uncertainty. V - The discrete case. *AT T Technical Journal*, 57:1371–1430.

Solanki, S. K., Barthol, P., Danilovic, S., Feller, A., Gandorfer, A., Hirzberger, J., Riethmüller, T. L., Schüssler, M., Bonet, J. A., Martínez Pillet, V., del Toro Iniesta, J. C., Domingo, V., Palacios, J., Knölker, M., Bello González, N., Berkefeld, T., Franz, M., Schmidt, W., and Title, A. M. (2010). SUNRISE: Instrument, Mission, Data, and First Results. *ApJL*, 723:L127–L133.

Soler, R., Carbonell, M., and Ballester, J. L. (2013). Magnetoacoustic Waves in a Partially Ionized Two-fluid Plasma. *ApJS*, 209:16.

Soler, R., Terradas, J., Oliver, R., Ballester, J. L., and Goossens, M. (2010). Kelvin-Helmholtz Instability in Coronal Magnetic Flux Tubes due to Azimuthal Shear Flows. *ApJ*, 712:875–882.

Song, P. (2017). A Model of the Solar Chromosphere: Structure and Internal Circulation. *ApJ*, 846:92.

Song, P. and Vasyliūnas, V. M. (2011). Heating of the solar atmosphere by strong damping of Alfvén waves. *Journal of Geophysical Research (Space Physics)*, 116:A09104.

Spruit, H. C. (1981). Equations for thin flux tubes in ideal MHD. *A&A*, 102:129–133.

Srivastava, A. K., Shetye, J., Murawski, K., Doyle, J. G., Stangalini, M., Scullion, E., Ray, T., Wójcik, D. P., and Dwivedi, B. N. (2017). High-frequency torsional Alfvén waves as an energy source for coronal heating. *Scientific Reports*, 7:43147.

Stangalini, M., Giannattasio, F., Erdélyi, R., Jafarzadeh, S., Consolini, G., Criscuoli, S., Ermolli, I., Guglielmino, S. L., and Zuccarello, F. (2017). Polarized Kink Waves in Magnetic Elements: Evidence for Chromospheric Helical Waves. *ApJ*, 840:19.

Sterling, A. C. (2000). Solar Spicules: A Review of Recent Models and Targets for Future Observations - (Invited Review). *SolPhys*, 196:79–111.

Sterling, A. C., Moore, R. L., Falconer, D. A., and Adams, M. (2015). Small-scale filament eruptions as the driver of X-ray jets in solar coronal holes. *Nature*, 523:437–440.

Suarez, D. O., Ramos, A. A., and Bueno, J. T. (2015). Height variation of the vector magnetic field in solar spicules. *ApJL*, 803(2):L18.

Suematsu, Y., Ichimoto, K., Katsukawa, Y., Shimizu, T., Okamoto, T., Tsuneta, S., Tarbell, T., and Shine, R. A. (2008). High Resolution Observations of Spicules with Hinode/SOT. In Matthews, S. A., Davis, J. M., and Harra, L. K., editors, *First Results From Hinode*, volume 397 of *Astronomical Society of the Pacific Conference Series*, page 27.

Suematsu, Y., Shibata, K., Neshikawa, T., and Kitai, R. (1982). Numerical hydrodynamics of the jet phenomena in the solar atmosphere. I - Spicules. *SolPhys*, 75:99–118.

Tanaka, K. (1974). Evolution of Chromospheric Fine Structures on the Disk. In Athay, R. G., editor, *Chromospheric Fine Structure*, volume 56 of *IAU Symposium*, page 239.

Tavabi, E., Koutchmy, S., Ajabshirizadeh, A., Ahangarzadeh Maralani, A. R., and Zeighami, S. (2015). Alfvénic waves in polar spicules. *A&A*, 573:A4.

Terradas, J. and Goossens, M. (2012). Transverse kink oscillations in the presence of twist. *A&A*, 548:A112.

Thomson, D. J. (1982). Spectrum Estimation and Harmonic Analysis. *IEEE Proceedings*, 70:1055–1096.

Trujillo Bueno, J., Merenda, L., Centeno, R., Collados, M., and Landi Degl'Innocenti, E. (2005). The Hanle and Zeeman Effects in Solar Spicules: A Novel Diagnostic Window on Chromospheric Magnetism. *ApJL*, 619:L191–L194.

Tsiropoula, G., Alissandrakis, C. E., and Schmieder, B. (1993). The fine structure of a chromospheric rosette. *A&A*, 271:574.

Tsiropoula, G., Tziotziou, K., Kontogiannis, I., Madjarska, M. S., Doyle, J. G., and Suematsu, Y. (2012). Solar Fine-Scale Structures. I. Spicules and Other Small-Scale, Jet-Like Events at the Chromospheric Level: Observations and Physical Parameters. *Space Science Review*, 169:181–244.

Ulmschneider, P. (1981). On the acoustic and magnetoacoustic heating of the outer atmosphere of stars. *Space Science Review*, 29:355.

Ulmschneider, P., Rammacher, W., Musielak, Z. E., and Kalkofen, W. (2005). On the Validity of Acoustically Heated Chromosphere Models. *ApJL*, 631:L155–L158.

Ulmschneider, P., Zaehringer, K., and Musielak, Z. E. (1991). Propagation of nonlinear longitudinal-transverse waves along magnetic flux tubes in the solar atmosphere. I - Adiabatic waves. *A&A*, 241:625–634.

Ulrich, R. K. (1996). Observations of Magnetohydrodynamic Oscillations in the Solar Atmosphere with Properties of Alfvén Waves. *ApJ*, 465:436.

Van Doorsselaere, T., Nakariakov, V. M., and Verwichte, E. (2008). Detection of Waves in the Solar Corona: Kink or Alfvén? *ApJL*, 676:L73.

van Hoek, M., Jia, L., Zhou, J., Zheng, C., and Menenti, M. (2016). Early Drought Detection by Spectral Analysis of Satellite Time Series of Precipitation and Normalized Difference Vegetation Index (NDVI). *Remote Sensing*, 8(5).

van Noort, M., Rouppe van der Voort, L., and Löfdahl, M. G. (2005). Solar Image Restoration By Use Of Multi-frame Blind De-convolution With Multiple Objects And Phase Diversity. *SolPhys*, 228:191–215.

Vernazza, J. E., Avrett, E. H., and Loeser, R. (1973). Structure of the Solar Chromosphere. Basic Computations and Summary of the Results. *ApJ*, 184:605–632.

Vernazza, J. E., Avrett, E. H., and Loeser, R. (1976). Structure of the solar chromosphere. II - The underlying photosphere and temperature-minimum region. *ApJS*, 30:1–60.

Vernazza, J. E., Avrett, E. H., and Loeser, R. (1981). Structure of the solar chromosphere. III - Models of the EUV brightness components of the quiet-sun. *ApJS*, 45:635–725.

Verth, G., Goossens, M., and He, J.-S. (2011). Magnetoseismological Determination of Magnetic Field and Plasma Density Height Variation in a Solar Spicule. *ApJL*, 733:L15.

Verth, G. and Jess, D. B. (2016). MHD Wave Modes Resolved in Fine-Scale Chromospheric Magnetic Structures. *Washington DC American Geophysical Union Geophysical Monograph Series*, 216:431–448.

Verth, G., Terradas, J., and Goossens, M. (2010). Observational Evidence of Resonantly Damped Propagating Kink Waves in the Solar Corona. *ApJL*, 718:L102–L105.

Vissers, G. J. M., Rouppe van der Voort, L. H. M., Rutten, R. J., Carlsson, M., and De Pontieu, B. (2015). Ellerman Bombs at High Resolution. III. Simultaneous Observations with IRIS and SST. *ApJ*, 812:11.

Weart, S. R. (1970). The Horizontal Component of Spicule Motion. *SolPhys*, 14:310–314.

Wedemeyer-Böhm, S., Lagg, A., and Nordlund, Å. (2009). Coupling from the Photosphere to the Chromosphere and the Corona. *Space Science Review*, 144:317–350.

Withbroe, G. L. and Noyes, R. W. (1977). Mass and energy flow in the solar chromosphere and corona. *Annu. Rev. Astro. Astrophys.*, 15:363–387.

Xia, L. D., Popescu, M. D., Doyle, J. G., and Giannikakis, J. (2005). Time series study of EUV spicules observed by SUMER/SoHO. *A&A*, 438:1115–1122.

Zaqarashvili, T. V. and Erdélyi, R. (2009). Oscillations and Waves in Solar Spicules. *Space Science Review*, 149:355–388.

Zaqarashvili, T. V., Khutsishvili, E., Kukhianidze, V., and Ramishvili, G. (2007). Doppler-shift oscillations in solar spicules. *A&A*, 474:627–632.

Zaqarashvili, T. V. and Skhirtladze, N. (2008). Helical Motion of Magnetic Flux Tubes in the Solar Atmosphere. *ApJL*, 683:L91.

Zhang, Y. Z., Shibata, K., Wang, J. X., Mao, X. J., Matsumoto, T., Liu, Y., and Su, J. T. (2012). Revision of Solar Spicule Classification. *ApJ*, 750:16.

Ziegler, U. and Ulmschneider, P. (1997a). Dynamical response of magnetic tubes to transverse perturbations. I. Thick flux tubes. *A&A*, 324:417–431.

Ziegler, U. and Ulmschneider, P. (1997b). Dynamical response of magnetic tubes to transverse perturbations. II. Towards thin flux tubes. *A&A*, 327:854–862.

Zirker, J. B. (1967). On the Motions of Chromospheric Fine-Structure in a Weak Plage. *SolPhys*, 1:204–215.

Appendix A

Supplementary cases

The spicule cases identified in the Hα dataset, as given in Table 1, were used to study the dynamics at both pixel- and spicule length-scale. Spicule structures (SP5, SP8 & SP1) are reported in detail, in Chapters 3, 4, 5, respectively. The analysis for other remaining spicule cases are present here, to supplement the findings presented in the Chapters before. The estimated parameters, that highlight the perturbed ambient magnetic and plasma pressures for spicule features (SP1, SP2, SP3, SP4, SP6, SP7) are given in Section 1, while the kinematic parameters for features SP2, SP3 and SP4, are presented in Section 2, along with phase relationships and non-helical evolution of transverse components with height.

Section 1

The estimated perturbations in magnetic and plasma pressures for the remaining spicule cases (SP1, SP2, SP3, SP4, SP6, SP7) are presented for accurate interpretation of the confined MHD wave modes in the flux tube structure. The observed physical parameters, along with the dominant plane of the transverse motion is listed in Table 1, given in Chapter 2. The estimation of the perturbed magnetic and plasma pressures are discussed in detail in Chapter 3, with detailed analysis for two sample cases, each for dominant transverse dynamics in the plane of sky (SP5) and the line of sight (SP8), with respect to the observer. The cases presented here (Figures A.1 - A.3) provides profound evidence of the perturbations in the spicule's ambient chromospheric environment, due to the dynamics of the structure under the influence of the confined wave mode. These analyzed cases also strengthen the fact that the kink wave mode has both internal (transverse) and external (rotational) dynamical characteristics, that strongly depend up on the observer's line of sight, when studied in imaging-spectroscopy data.

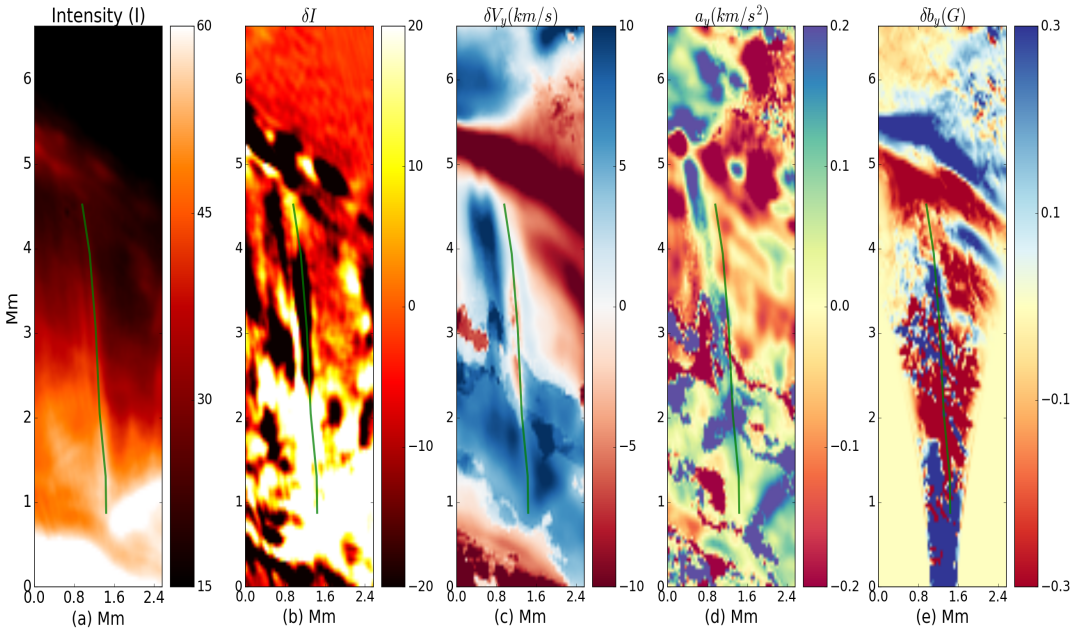

(a) Estimated parameters for spicule SP1, used to identify the confined wave mode. The spicule had dominant bulk transverse motion in observer's LOS.

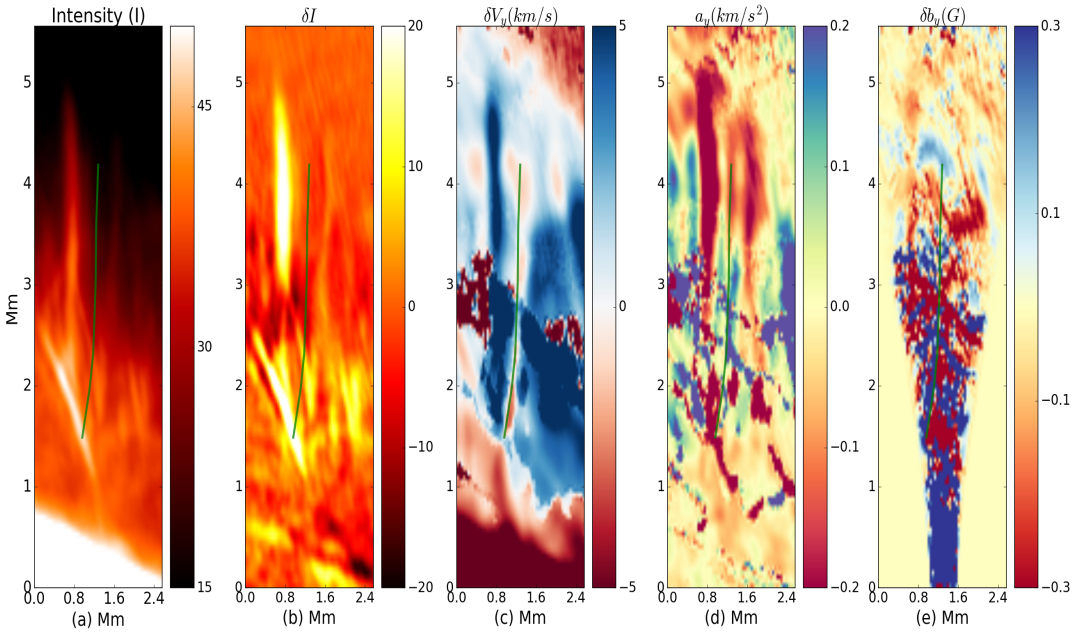

(b) Observed and estimated parameters for spicule SP2 with bulk transverse motion in observer's LOS.

Fig. A.1 Panels show the observed and estimated parameters of spicules SP1 & SP2 (marked by lines). In respective panels (a), the ROI is highlighted in the Hα intensity image. Panels (b) to (e) show the intensity difference (δI), Doppler velocity (δV_y), acceleration (a_y) and the LOS magnetic field perturbation (δb_y), respectively.

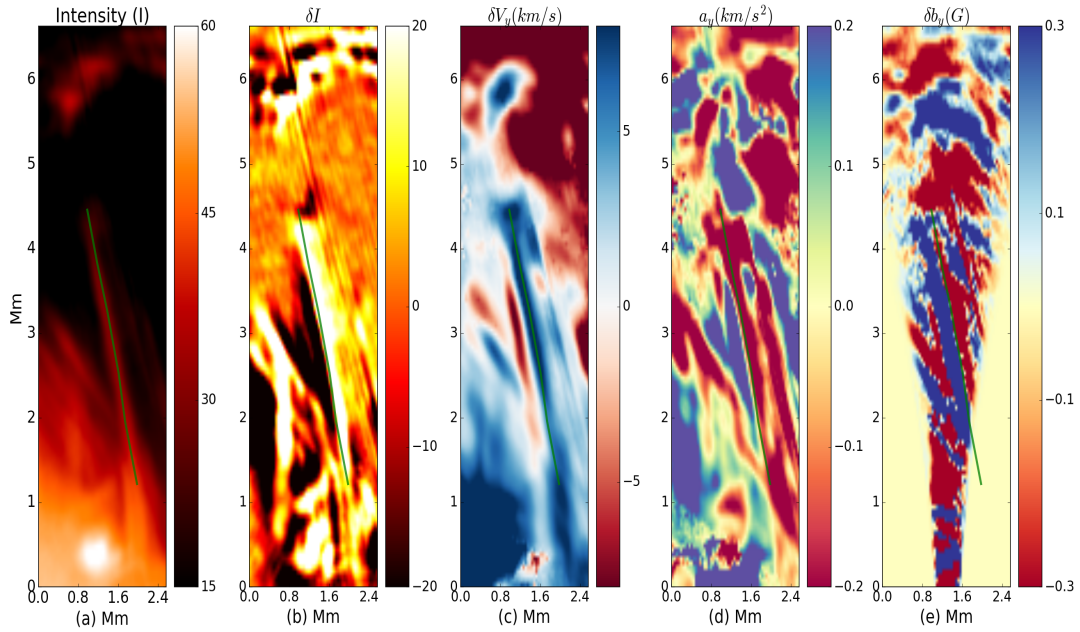

(a) Estimated parameters for spicule SP3, with dominant bulk transverse motion in observer's LOS.

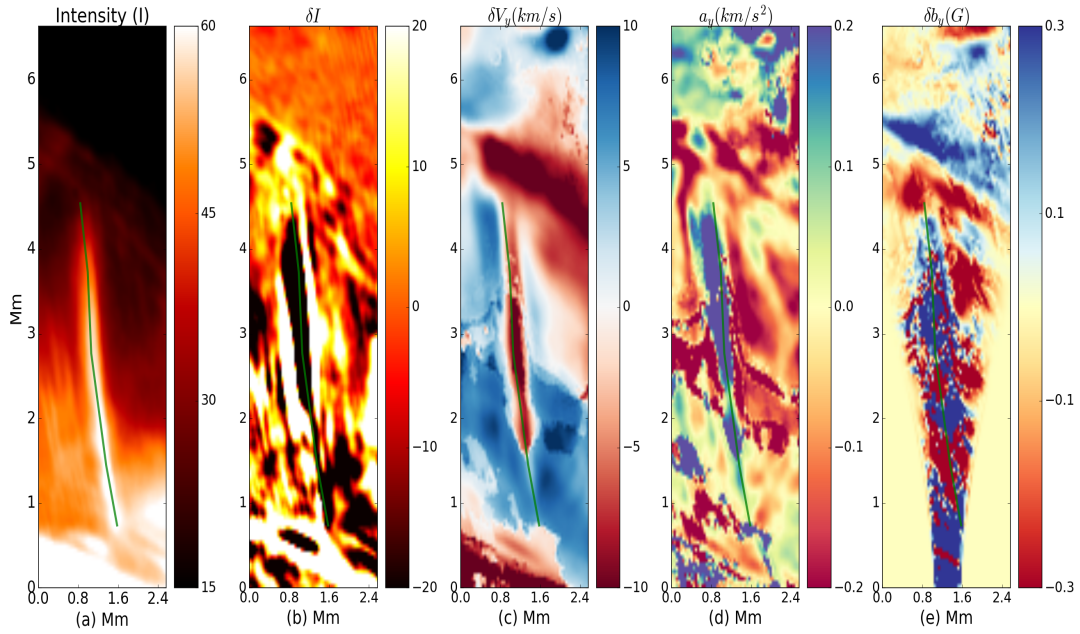

(b) Observed and estimated parameters for spicule SP4 with bulk transverse motion in observer's POS. The red-blue axisymmetry in the LOS Doppler profile indicates the displacement of ambient plasma due to spicule motion.

Fig. A.2 Panels show the observed and estimated parameters of spicules SP3 & SP4 (marked by lines). In respective panels (a), the ROI is highlighted in the Hα intensity image. Panels (b) to (e) show the intensity difference (δI), Doppler velocity (δV_y), acceleration (a_y) and the LOS magnetic field perturbation (δb_y), respectively.

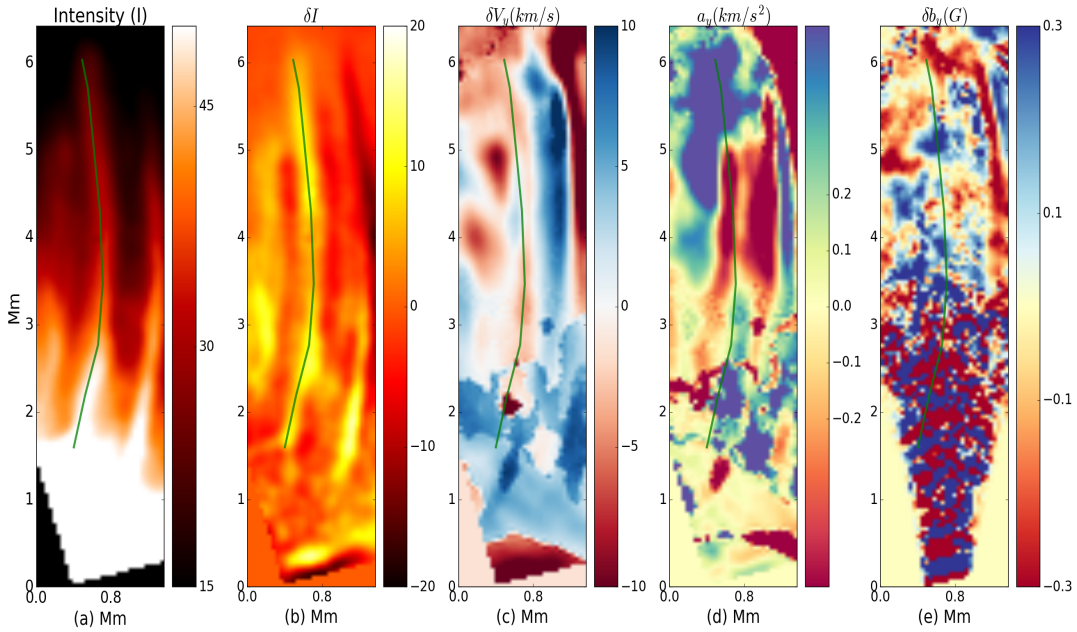

(a) Observed and estimated parameters for spicule SP6 with bulk transverse motion in observer's POS. The red-blue axisymmetry in the LOS Doppler profile indicates the displacement of ambient plasma due to spicule motion.

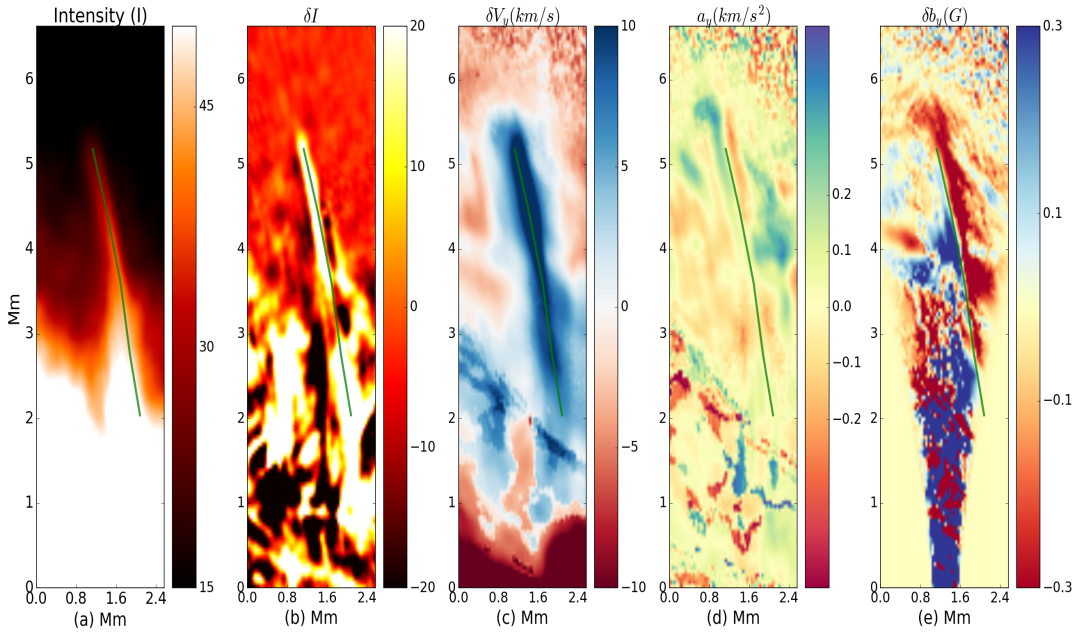

(b) Observed and estimated parameters for spicule SP7 with bulk transverse motion in observer's LOS.

Fig. A.3 Panels show the observed and estimated parameters of spicules SP6 & SP7 (marked by lines). In respective panels (a), the ROI is highlighted in the Hα intensity image. Panels (b) to (e) show the intensity difference (δI), Doppler velocity (δV_y), acceleration (a_y) and the LOS magnetic field perturbation (δb_y), respectively.

Section 2

In this section, three additional cases (SP2, SP3, SP4) are provided, with detailed analysis of the sample feature (SP1) is already discussed for nonlinear kink wave dynamics (Chapter 4), and non-helical transverse dynamics (Chapter 5). The estimation of the kinematic parameters and also analysis methods are same as discussed in the chapters before.

Spicule 2

The spicule (SP2) had an average visible geometric length of 2.5 Mm, reaching up to a height of around 4.1 Mm, inclined to the normal at the limb at an angle of 13.0°. The estimation of different kinematic parameters (transverse, cross sectional width and azimuthal shear/torsion) is given in detail in Chapter 4. The evolution of these estimated parameters, in height and time are given in Figure A.4. These parameters show profound coherence in both wavenumber and frequency domains, with in-phase and out-of-phase oscillatory behavior in time (Fig. A.5). The frequency analysis indicate towards the nonlinear evolution of these parameters with period-doubling and tripling aspects. The primary and secondary peaks were located at 0.0118 Hz (84.7 sec) and 0.0354 Hz (24.2 sec) for transverse and photometric variations, with azimuthal shear/torsion parameter shows a peak at 0.0236 Hz (42.3 sec). The strong coupling in between the estimates is also evident from the mutual variations in between the phase angles (Fig. A.6), concentrated around 0° and $\pm 180^\circ$. Furthermore, the transverse components (POS, LOS and the resultant displacement) show out-of-phase behavior in their evolution over height, as shown for three distinct time-steps over the lifetime (Fig. A.7) of the SP2 feature. The trend due to the first kink wave mode dominates the overall dynamics of the structure while the secondary kink wave mode shows strong non-helical motion with height.

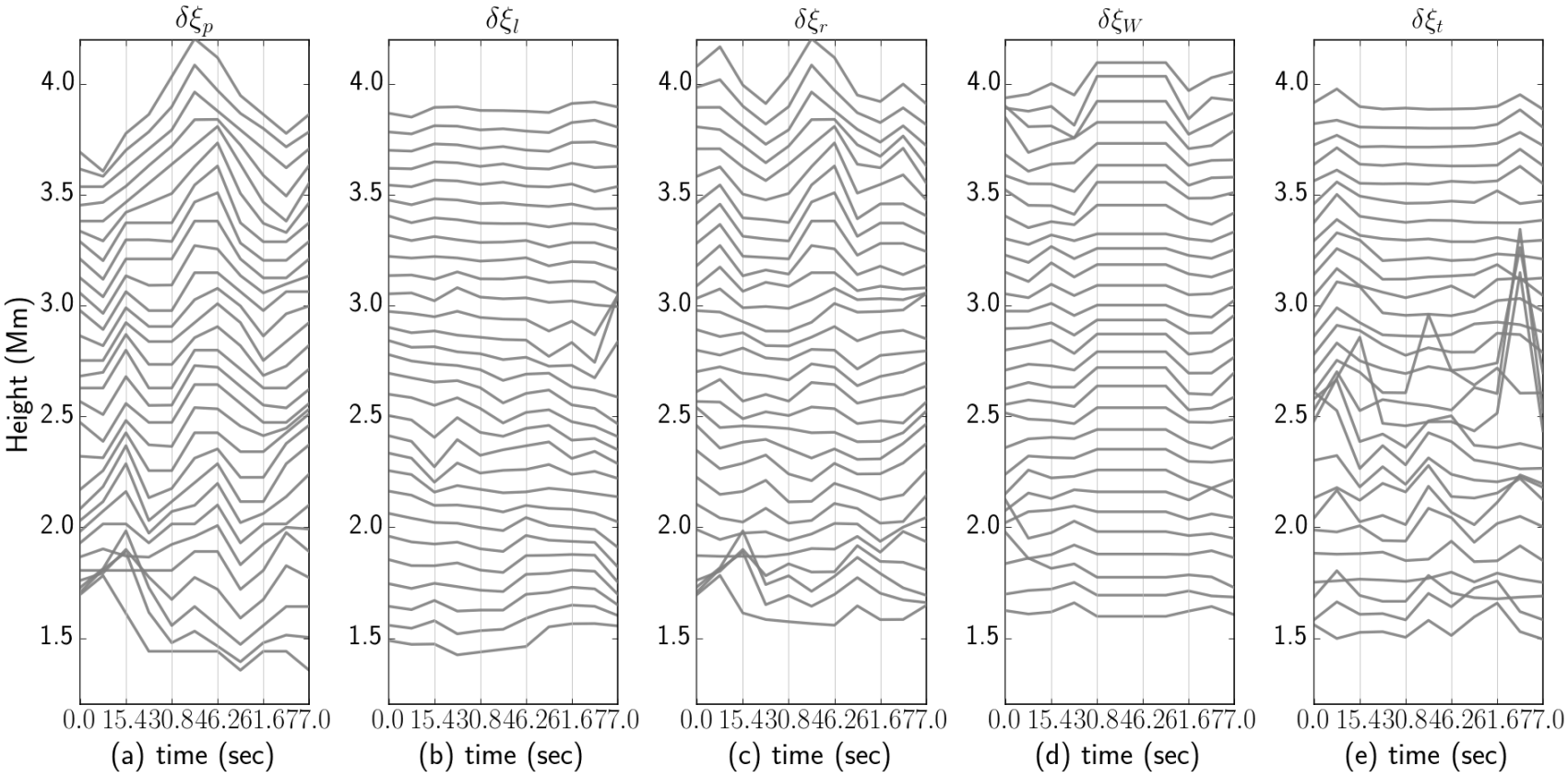

Fig. A.4 Evolution of the time-distance (TD) behavior for the spicule (SP2) structure with height, sampled at every four pixels ($\sim$172 km) apart. Panel (a-c) shows transverse components estimated in POS (a: $\delta\xi_p$), LOS (b: $\delta\xi_l$) and the resultant (c: $\delta\xi_r$). Panel (d) plots the variations in cross-sectional width estimates ($\delta\xi_W$), while the azimuthal shear/torsion ($\delta\xi_t$) components are shown in panel (e). The magnitude of the parameters shown here is in 'km'.

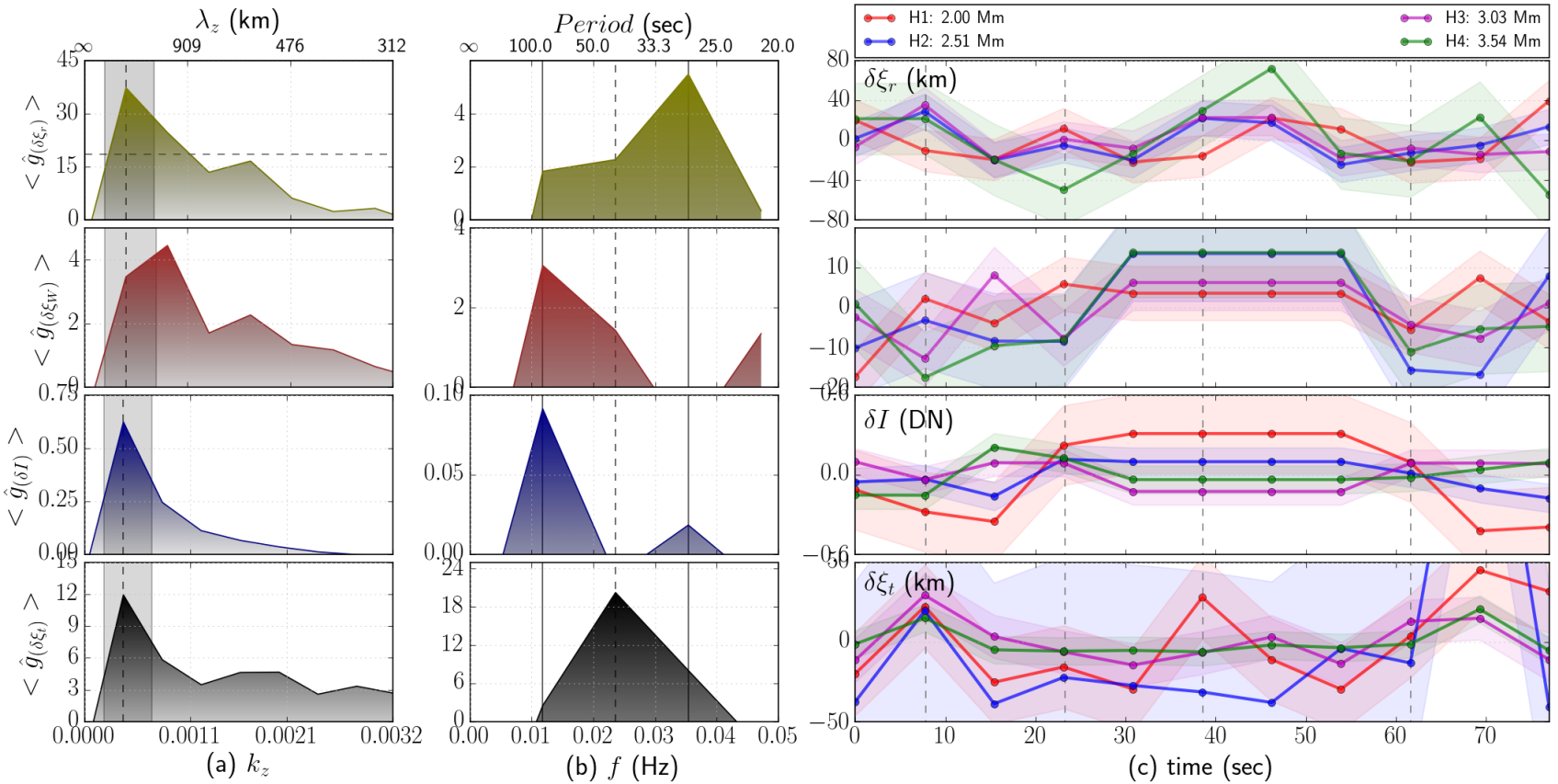

Fig. A.5 The spectral and temporal variations in transverse displacement ($\delta\xi_r$), cross-sectional width ($\delta\xi_W$), intensity (δI) and azimuthal shear/torsion ($\delta\xi_t$) parameters, for spicule (SP2), are shown. Panel (a) shows the temporally averaged spectral profiles (top to bottom: displacement, width, intensity, azimuthal shear), in wavenumber (k_z) domain, with the mean power (taken as background noise) removed. Shaded-region highlights the half-max (horizontal dashed-line) width of the distribution of the peak spectral power (vertical dashed-line). Panel (b) shows similar analysis in frequency (f) domain with primary and secondary peaks in resultant displacement, cross-sectional width and intensity marked with solid lines. Panels (c) show the time evolution of the parameters for different heights. Examples of in-phase and out-of-phase oscillations are marked with vertical dashed-lines.

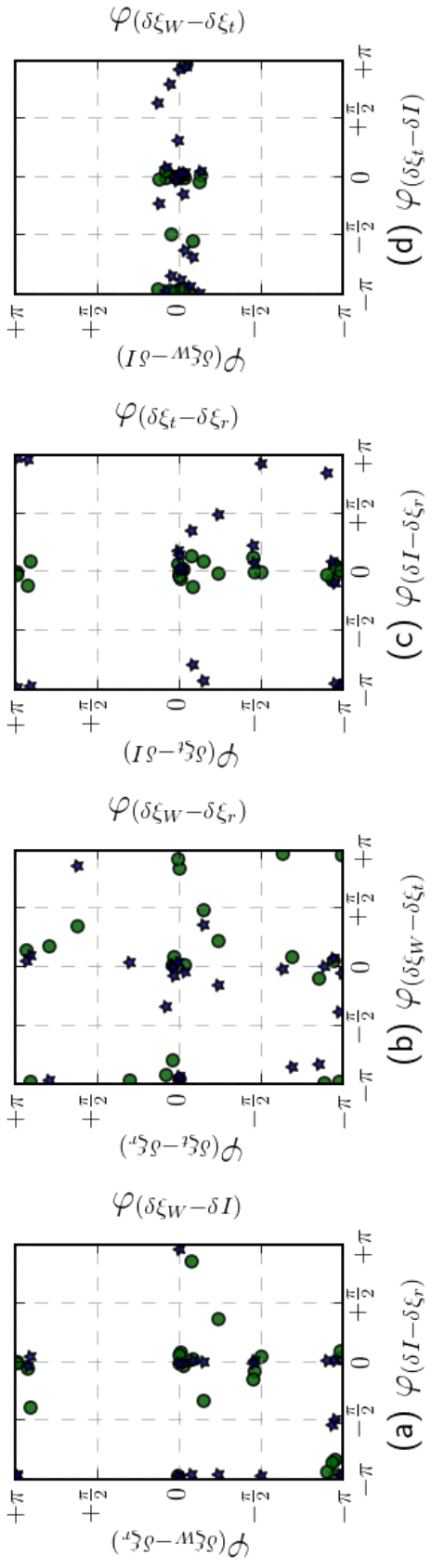

Fig. A.6 Scatter plots showing mutual variations of the estimated phase relations in frequency domains for different observables. The mutual phase relations between the parameter-pairs on x-axis and y-axis (on left) are marked as circle, while the relationship with the parameter-pairs between x-axis and y'-axis (on right) are marked here as star. The phase differences are mostly concentrated around 0° and $\pm\pi^\circ$ with a deviation of $\pm 30^\circ$.

Spicule 3

The spicule (SP3) had an average visible geometric length of 2.2 Mm, reaching up to a height of around 4.8 Mm, inclined to the normal at the limb at an angle of 35.7°. The evolution of these estimated parameters, in height and time are given in Figure A.8. These parameters show profound coherence in both wavenumber and frequency domains, with in-phase and out-of-phase oscillatory behavior in time (Fig. A.9). The frequency analysis indicate towards the nonlinear evolution of these parameters with period-doubling and tripling aspects. The primary and secondary peaks were located at 0.0143 Hz (69.9 sec) and 0.0433 Hz (23.0 sec) for transverse and photometric variations, with azimuthal shear/torsion parameter shows a peak at 0.0287 Hz (34.8 sec). These results are concurrent with those obtained for SP1. The strong coupling in between the estimates is also evident from the mutual variations in between the phase angles (Fig. A.10), concentrated around 0° and $\pm 180^\circ$. Furthermore, the transverse components (POS, LOS and the resultant displacement) show out-of-phase behavior in their evolution over height, as shown for three distinct time-steps over the lifetime (Fig. A.11) of the SP3 feature. The trend due to the first kink wave mode dominates the overall dynamics of the structure while the secondary kink wave mode shows strong non-helical motion with height.

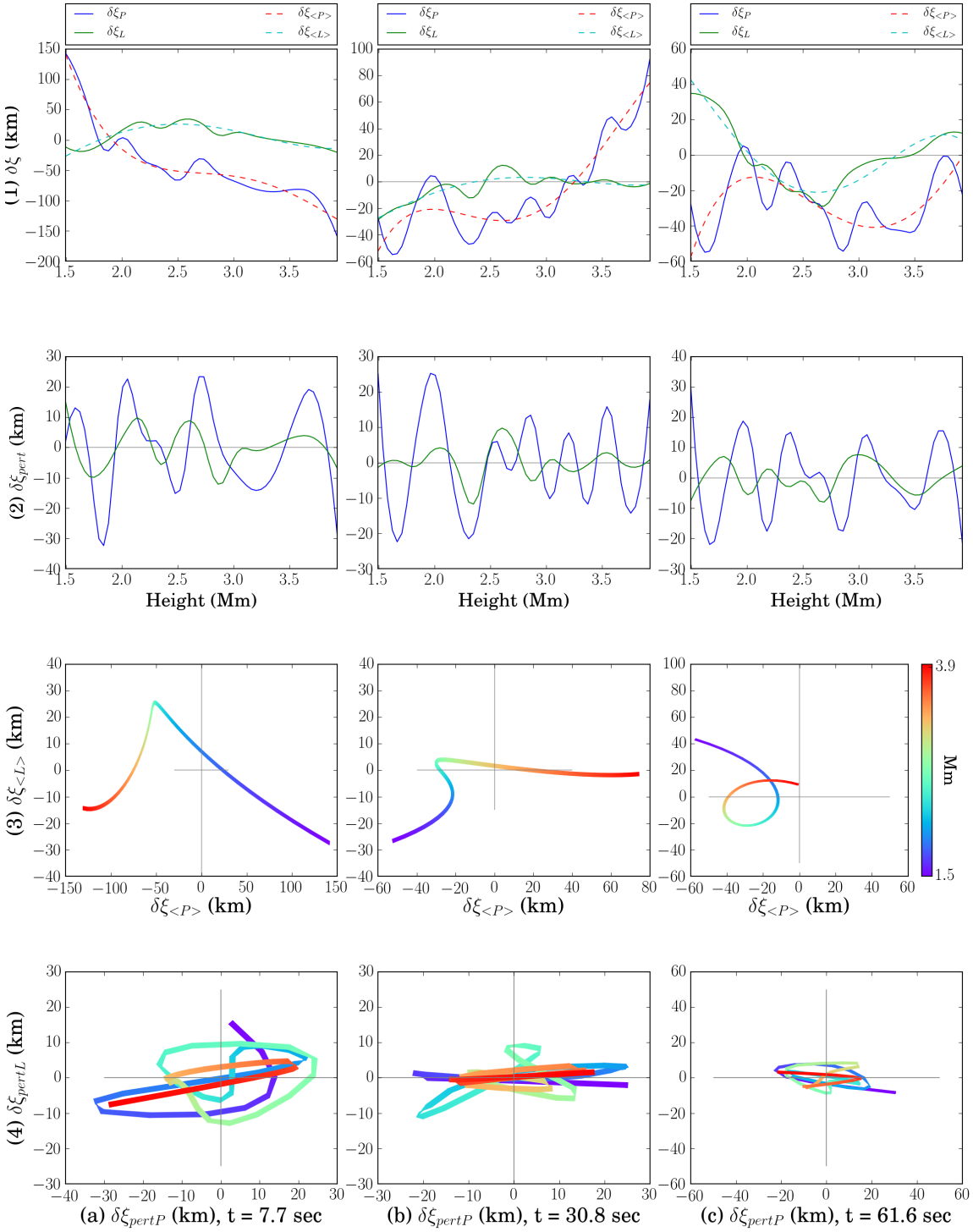

Fig. A.7 Panels (a-c) shows the evolution of the estimated transverse components (POS-LOS), for spicule SP2, at three time-steps over height, along with the *Lissajous-like* plots to highlight the non-helical behavior. Top panel (1) show the POS-LOS components with a sinusoidal function fit (marked as a dashed-line), indicative of the dominant trend of the motion in perpendicular planes. The perturbed parameters ($\delta\xi_{pert}$), estimated by removing the fit (trend) from the estimated data is shown in panel (2). The *Lissajous-like* plot for the fitted function and the perturbed parameters are shown in panels (3) and (4), respectively.

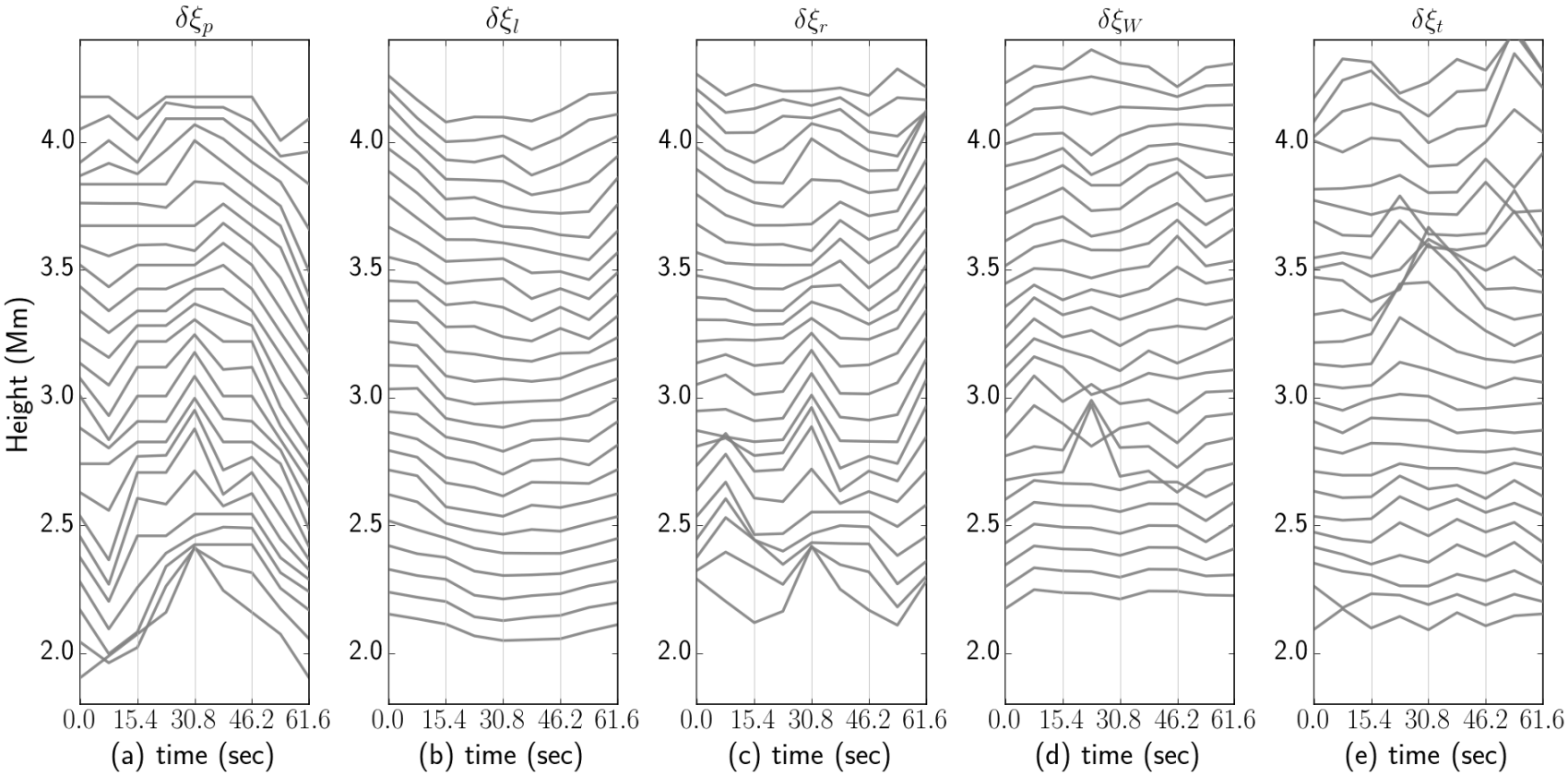

Fig. A.8 Evolution of the time-distance (TD) behavior for the spicule (SP3) structure with height, sampled at every four pixels (∼172 km) apart. Panel (a-c) shows transverse components estimated in POS (a: $\delta\xi_p$), LOS (b: $\delta\xi_l$) and the resultant (c: $\delta\xi_r$). Panel (d) plots the variations in cross-sectional width estimates ($\delta\xi_W$), while the azimuthal shear/torsion ($\delta\xi_t$) components are shown in panel (e). The magnitude of the parameters shown here is in 'km'.

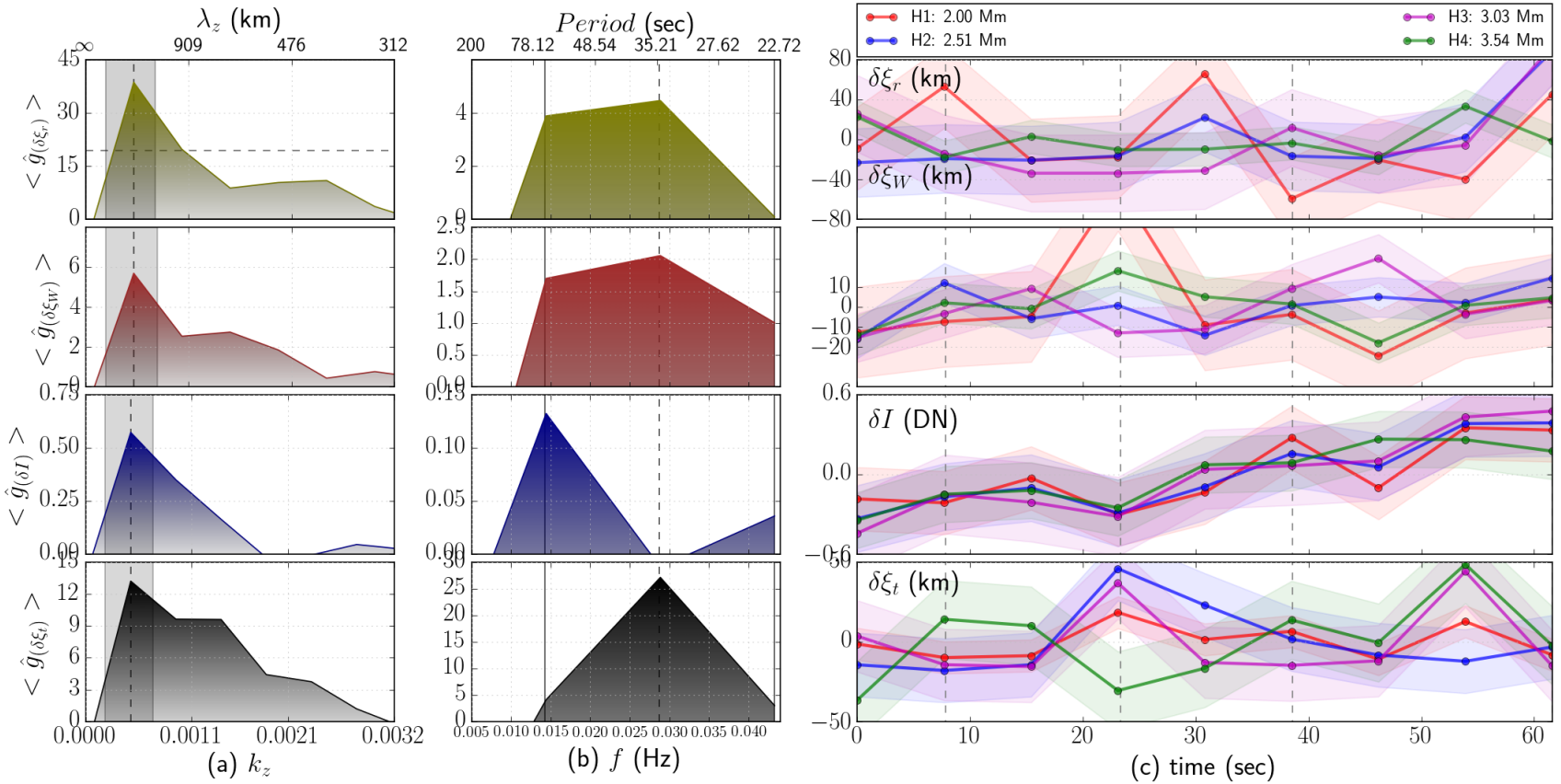

Fig. A.9 The spectral and temporal variations in transverse displacement ($\delta\xi_r$), cross-sectional width ($\delta\xi_W$), intensity (δI) and azimuthal shear/torsion ($\delta\xi_t$) parameters, for spicule (SP3), are shown. Panel (a) shows the temporally averaged spectral profiles (top to bottom: displacement, width, intensity, azimuthal shear), in wavenumber (k_z) domain, with the mean power (taken as background noise) removed. Shaded-region highlights the half-max (horizontal dashed-line) width of the distribution of the peak spectral power (vertical dashed-line). Panel (b) shows similar analysis in frequency (f) domain with primary and secondary peaks in resultant displacement, cross-sectional width and intensity marked with solid lines. Panels (c) show the time evolution of the parameters for different heights. Examples of in-phase and out-of-phase oscillations are marked with vertical dashed-lines.

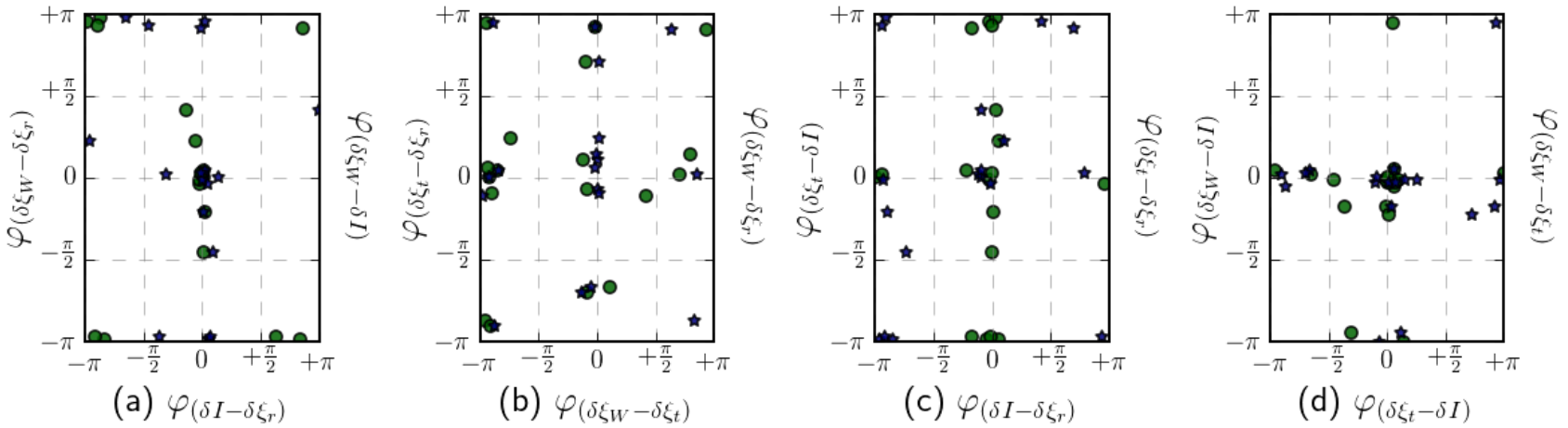

Fig. A.10 Scatter plots showing mutual variations of the estimated phase relations in frequency domains for different observables. The mutual phase relations between the parameter-pairs on x-axis and y-axis (on left) are marked as circle, while the relationship with the parameter-pairs between x-axis and y'-axis (on right) are marked here as star. The phase differences are mostly concentrated around 0° and $\pm\pi^\circ$ with a deviation of $\pm 30^\circ$.

Spicule 4

The spicule (SP4) had an average visible geometric length of 3.7 Mm, reaching up to a height of around 4.4 Mm, inclined to the normal at the limb at an angle of 33.2°. The evolution of these estimated parameters, in height and time are given in Figure A.12. These parameters show profound coherence in both wavenumber and frequency domains, with in-phase and out-of-phase oscillatory behavior in time (Fig. A.13). The frequency analysis, however, show linear coupling in between the observed variables with peaks (primary) coinciding at 0.0162 Hz (69.9 sec) for transverse, cross sectional width, photometric and azimuthal shear/torsion parameters, along with a deficit in PSD at 0.0325 Hz (30.76 sec). The estimated averaged-PSD indicate presence of another peak (secondary), close to the Nyquist frequency, that could be indicative of a nonlinear behavior. The strong coupling in between the estimates is also evident from the mutual variations in between the phase angles (Fig. A.14), concentrated around 0° and $\pm 180°$. Furthermore, the transverse components (POS, LOS and the resultant displacement) show out-of-phase behavior in their evolution over height, as shown for three distinct time-steps over the lifetime (Fig. A.15) of the SP4 feature. The trend due to the first kink wave mode dominates the overall dynamics of the structure while the secondary kink wave mode shows strong non-helical motion with height.

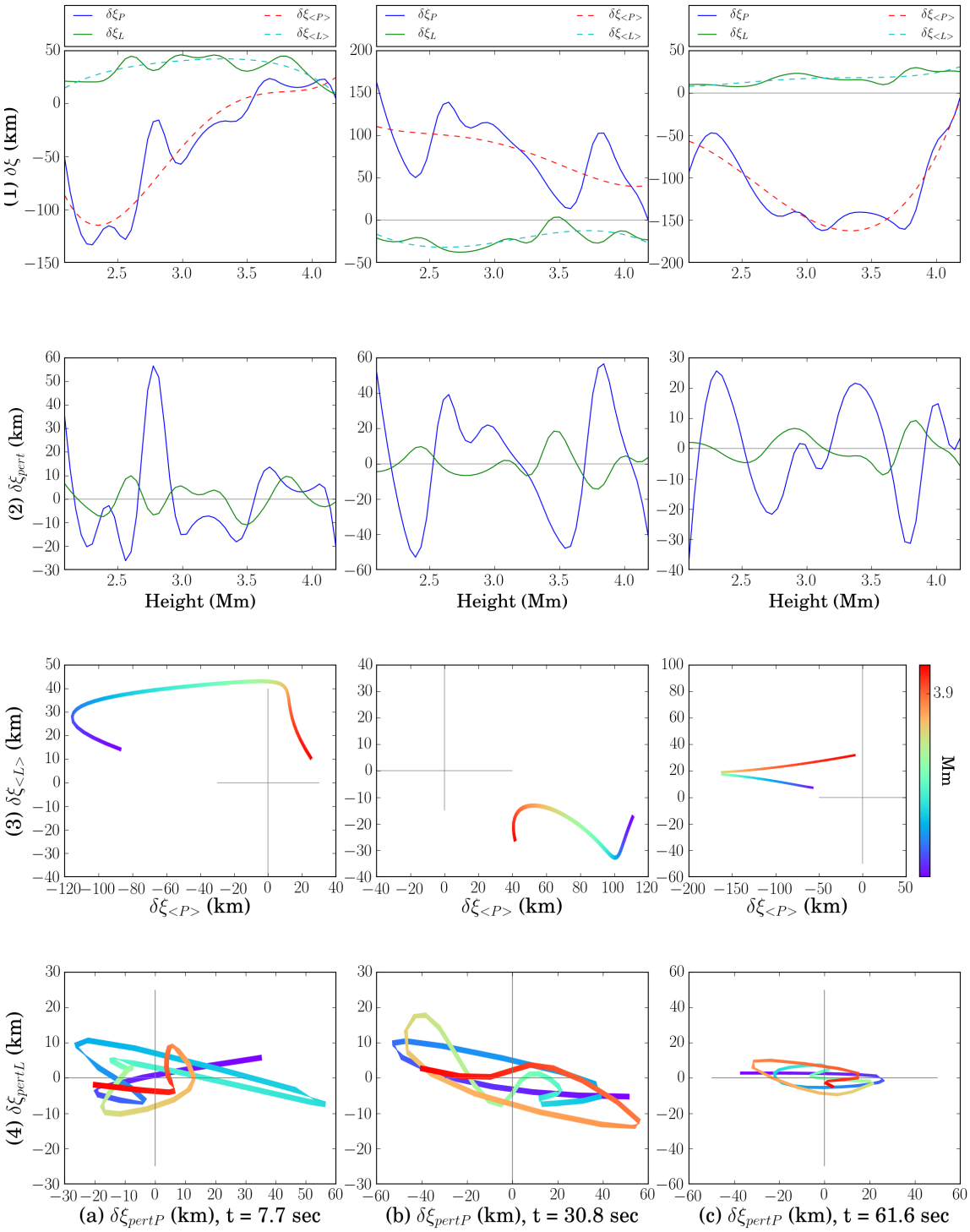

Fig. A.11 Panels (a-c) shows the evolution of the estimated transverse components (POS-LOS), for spicule SP3, at three time-steps over height, along with the *Lissajous-like* plots to highlight the non-helical behavior. Top panel (1) show the POS-LOS components with a sinusoidal function fit (marked as a dashed-line), indicative of the dominant trend of the motion in perpendicular planes. The perturbed parameters ($\delta\xi_{pert}$), estimated by removing the fit (trend) from the estimated data is shown in panel (2). The *Lissajous-like* plot for the fitted function and the perturbed parameters are shown in panels (3) and (4), respectively.

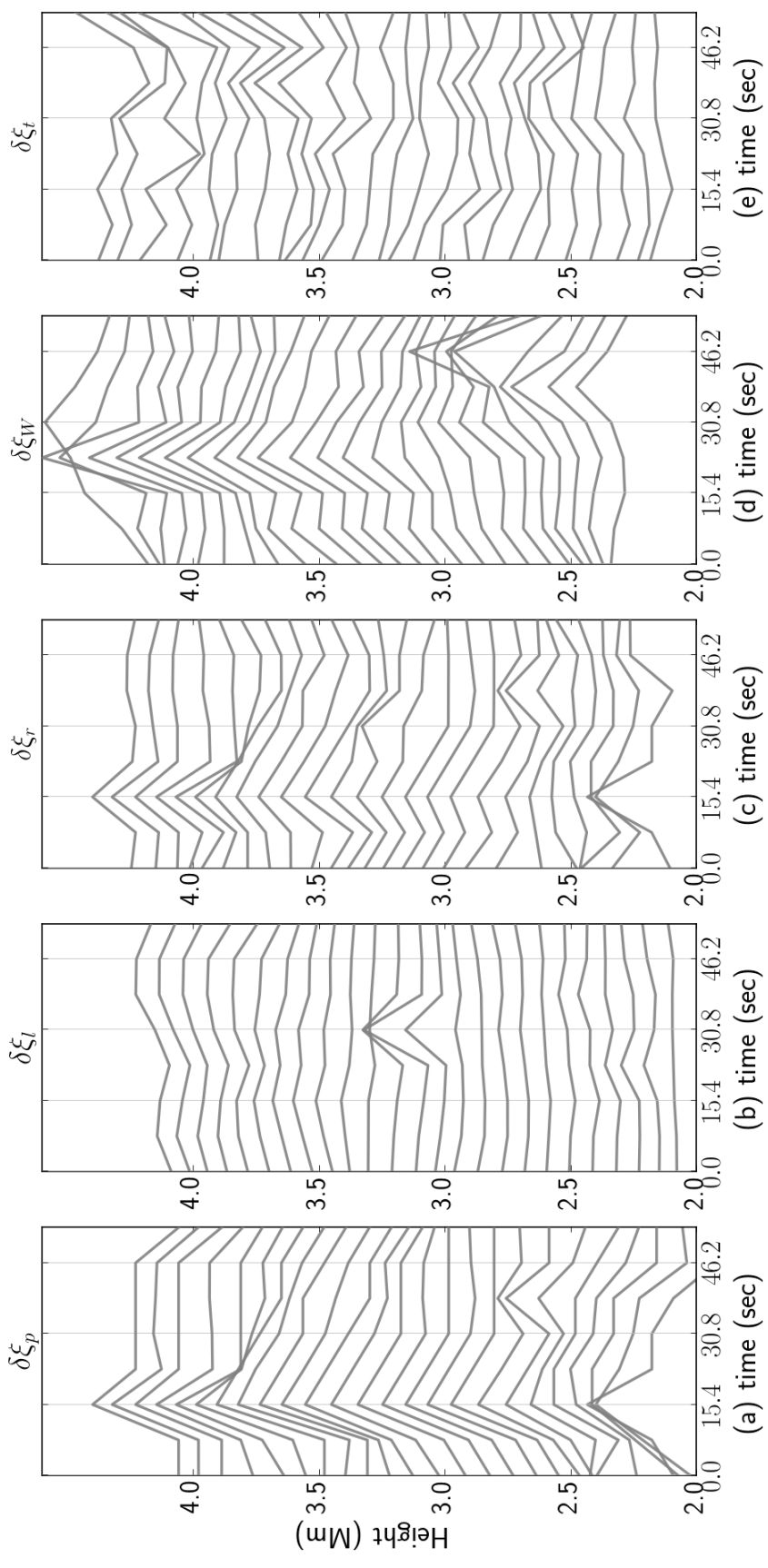

Fig. A.12 The target region over a course of a few days before the CRISP/SST data were taken. Top panels show the Hα images of the sunspots (taken from www.solarmonitor.org), on 18 and 19 June, 2012, which were the target of CRISP/SST observations used in the thesis. Middle panels show the region on 20 June, 2012, along with the CRISP/SST field-of-view (FOV) at the limb on 21 June, 2012. Bottom panel shows the Hα limb observations with the spicule structures analyzed to understand the dynamical behavior.

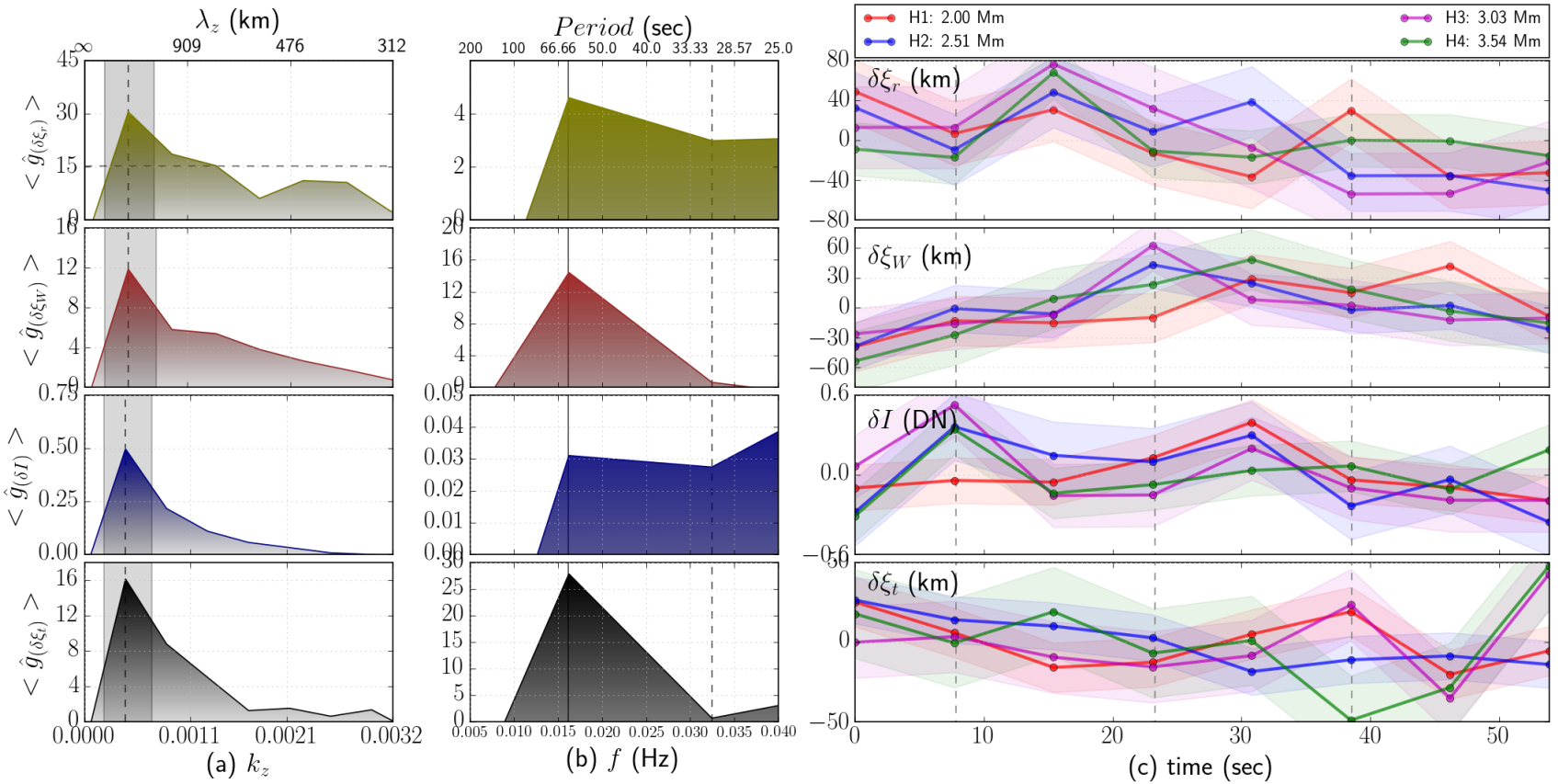

Fig. A.13 The spectral and temporal variations in transverse displacement ($\delta\xi_r$), cross-sectional width ($\delta\xi_W$), intensity (δI) and azimuthal shear/torsion ($\delta\xi_t$) parameters, for spicule (SP4), are shown. Panel (a) shows the temporally averaged spectral profiles (top to bottom: displacement, width, intensity, azimuthal shear), in wavenumber (k_z) domain, with the mean power (taken as background noise) removed. Shaded-region highlights the half-max (horizontal dashed-line) width of the distribution of the peak spectral power (vertical dashed-line). Panel (b) shows similar analysis in frequency (f) domain with primary and secondary peaks in resultant displacement, cross-sectional width and intensity marked with solid lines. Panels (c) show the time evolution of the parameters for different heights. Examples of in-phase and out-of-phase oscillations are marked with vertical dashed-lines.

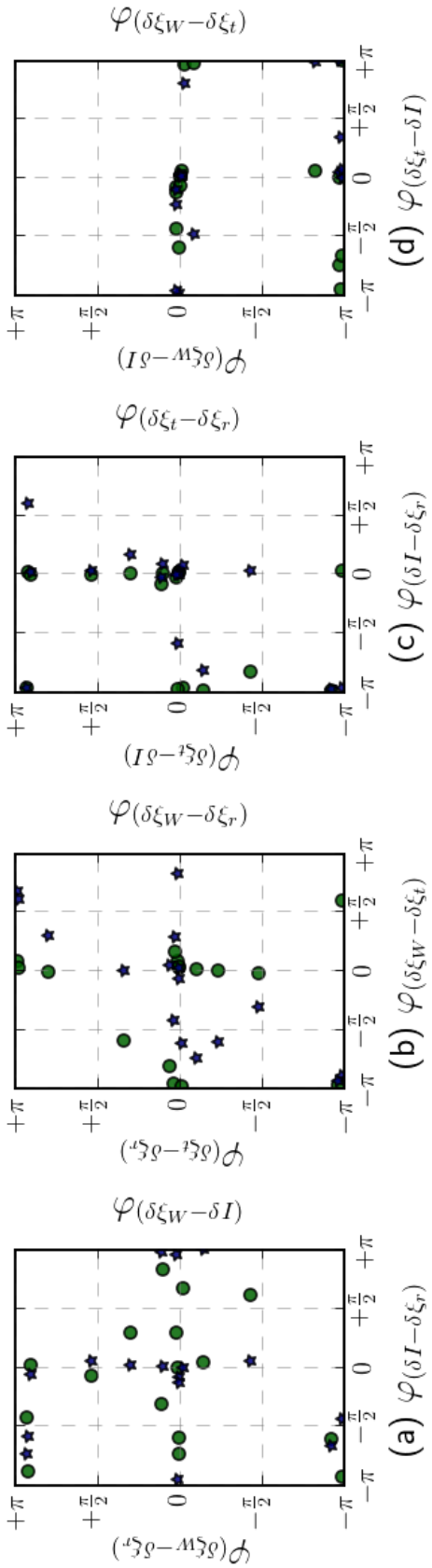

Fig. A.14 Scatter plots showing mutual variations of the estimated phase relations in frequency domains for different observables. The mutual phase relations between the parameter-pairs on x-axis and y-axis (on left) are marked as circle, while the relationship with the parameter-pairs between x-axis and y'-axis (on right) are marked here as star. The phase differences are mostly concentrated around 0° and $\pm\pi^\circ$ with a deviation of $\pm 30^\circ$.

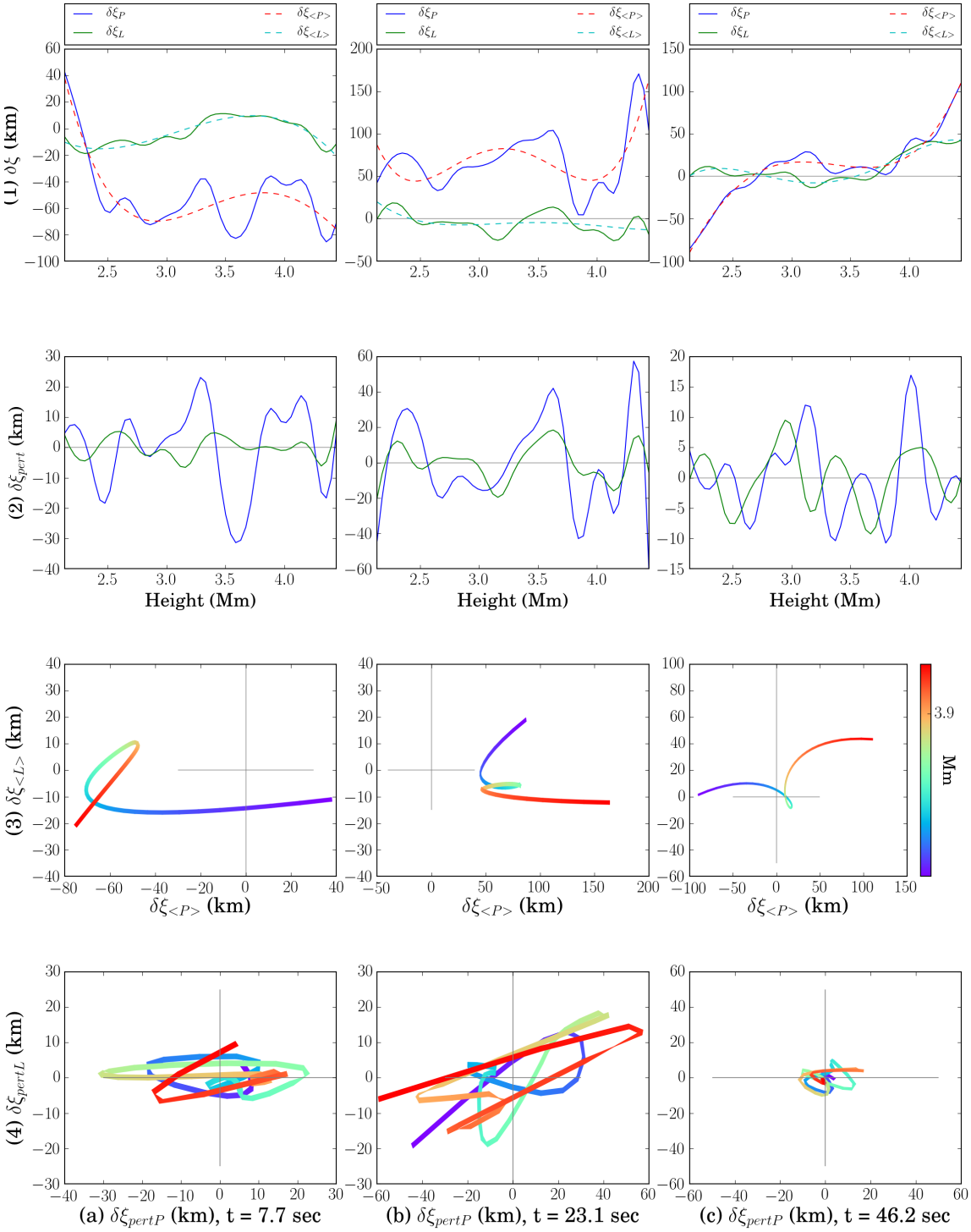

Fig. A.15 Panels (a-c) shows the evolution of the estimated transverse components (POS-LOS), for spicule SP4, at three time-steps over height, along with the *Lissajous-like* plots to highlight the non-helical behavior. Top panel (1) show the POS-LOS components with a sinusoidal function fit (marked as a dashed-line), indicative of the dominant trend of the motion in perpendicular planes. The perturbed parameters ($\delta\xi_{pert}$), estimated by removing the fit (trend) from the estimated data is shown in panel (2). The *Lissajous-like* plot for the fitted function and the perturbed parameters are shown in panels (3) and (4), respectively.